UNIVERSIDADE DA BEIRA INTERIOR
Engenharia

# Hybrid Robust Distributed Propulsion Control of Lateral-Directional Flight Dynamics

(Versão corrigida após defesa)

**Alexandra Teles de Lima Ferreira Monteiro**

Dissertação para obtenção do Grau de Mestre em
**Engenharia Aeronáutica**
(Ciclo de estudos integrado)

Orientador: Prof. Doutor Kouamana Bousson
Co-orientador: Doutor Ricardo José Nunes dos Reis

**Covilhã, janeiro de 2020**

To my dear grandparents, Américo and Glória ♡

*“All our dreams can come true,*
*if we have the courage to pursue them.”*

— Walt Disney

# Acknowledgments

It has been quite a journey. Ending this cycle, I can't even begin to describe how grateful I am and how lucky I feel for having been given so many great opportunities that made me grow and happily led me to where I am today.

A lot of those opportunities I must thank for to Embraer Portugal CETE's team, for welcoming me with open arms into such a friendly work atmosphere, always making me feel like one of them. I could not thank you all enough, particularly to Marta Quintiães and Sérgio Carvalho, true friends who supported me by believing in me, boosting my internship in Brasil.

To my mentor and friend, Ricardo Reis, a special thanks for he has taught me to believe in myself and humbly accept what I do not know, without ever making me feel afraid to ask questions and instigating me to always learn more *"partindo o boi a bife"*. A great deal of my aeronautical knowledge and critical thinking ability I've learnt from you.

During my time in Embraer's headquarters I've made countless friends, who've helped me and made me feel at home in a faraway country, by cheering my days with good mood and humorous thoughts, fortunately, too many to mention individually. It was certainly a lifetime experience.

José Parizi and Fernando Moreira, my absolute gratitude for all the flight controls knowledge passed on, valuable discussions while still defining this work's trail, countless advices and suggestions and most of all for cheering and believing in my work. I've learnt so much thanks to you.

I also could not thank enough to my academic supervisor, professor Kouamana Bousson, for his guidance availability for long distance video meetings, all the calmness and tranquillity he consistently transmitted, without ever making me feel pressured or stressed and appeasing me in those times when I did. Further, for his endless applied-mathematics' methods' suggestions for solving control problems, whenever the previous didn't work.

An enormous thank you to all my friends, whose hangouts I kept rescheduling and postponing in order to focus and finish this work. Your understanding and support are priceless.

A special thanks to my boyfriend, Gustavo, for strengthening me every step of the way even when it meant drifting us apart. I am aware I am a handful, bless you for your patience and may I always be able to make you as happy as you make me.

Lastly but not least, my utmost gratitude goes to my family, who've always done their best raising me and shaping my personality, leading me to where I am today and encouraging me through my every ambition. You'll always have my unconditional love and admiration, especially my grandparents, to whom I've dedicated this work to — your absence is heartily felt.

# Resumo

As aeronaves de asa fixa são geralmente controladas por meio de superfícies de controlo como o leme de profundidade, ailerons e leme de direção. Estas superfícies são operadas através de atuadores hidráulicos e/ou elétricos. Em caso de falha dos sistemas de superfície de controlo (isto é, dos atuadores de controlo e dispositivos de acoplamento), a aeronave pode sofrer danos, levando a acidentes graves ou até mesmo fatais.

Uma história crescente de acidentes e incidentes motivou investigações sobre o uso da propulsão como controlo de voo em situações de emergência e, desde então, pesquisas relativas a aeronaves controladas por propulsão ganharam uma popularidade crescente nas últimas décadas, deixando de ser motivada exclusivamente por razões de segurança à medida em que os investigadores se foram apercebendo que o controlo de propulsão é mais flexível do que as superfícies de controlo clássicas e que os veículos controlados por propulsão são propensos a uma estabilização de atitude e rastreamentos de trajetória altamente rápidos.

A propulsão elétrica distribuída abre ainda mais oportunidades para aeronaves controladas por propulsão, introduzindo motores com respostas mais rápidas e com capacidade de tração adicional, garantindo flexibilidade de integração sem escala e sem perda de potência à medida que a altitude aumenta. Além disso, a implementação da propulsão elétrica distribuída beneficia das vantagens do acoplamento aero-propulsivo, redução de ruído com um impacto acústico substancialmente mais baixo e um impacto positivo no ambiente.

Assim sendo, o conceito do sistema de propulsão elétrica distribuída como atuador de controlo potencializa novos recursos para o projeto, eficiência e robustez de futuras aeronaves, melhorando o desempenho dos projetos convencionais, incluindo a redução das superfícies de controlo tradicionais e da vulnerabilidade do sistema de controlo da aeronave a casos de falha de motores.

Deste modo, o presente trabalho aborda a questão do controlo robusto da dinâmica latero-direcional para uma aeronave controlada por propulsão com incertezas de parâmetros, com o objetivo de entender como controlar uma aeronave de forma robusta através do seu sistema de propulsão elétrica distribuída e como usar essa capacidade para introduzir melhorias no projeto de aeronaves. Concretamente, a questão central concentra-se no projeto de um controlador híbrido robusto, capaz de lidar com um modo de operação independente de controlo por propulsão e um modo convencional, combinando, se necessário, o controlo por propulsão e a operação das superfícies de controlo.

Os métodos propostos são então validados através de simulações computacionais em cenários de voo realistas, tais como várias curvas coordenadas niveladas e uma falha crítica do motor.

# Palavras-chave

Controlo robusto por propulsão , Controlo por H-infinito, Dinâmica de voo latero-direcional, Incertezas de parâmetros, Propulsão Eléctrica Distribuída.

# Resumo alargado

As aeronaves de asa fixa são geralmente controladas por meio de superfícies de controlo como o leme de profundidade, ailerons e leme de direção. Estas superfícies são operadas através de atuadores hidráulicos e/ou elétricos. Em caso de falha dos sistemas de superfície de controlo (isto é, dos atuadores de controlo e dispositivos de acoplamento), a aeronave pode sofrer danos catastróficos.

Por mais de 50 anos, várias aeronaves enfrentaram grandes falhas no sistema de controlo de voo, levando a acidentes graves ou até mesmo fatais, resultando em mais de 1200 vidas perdidas. A crescente história de acidentes e incidentes motivou investigações sobre o uso da propulsão como controlo de voo em situações de emergência, tendo-se realizado diversos estudos analíticos, em simuladores e em voo sobre o assunto.

Muitos dados interessantes puderam ser retirados dessas investigações e o potencial de usar a propulsão como forma de controlo expandiu-se de ser exclusivamente para fins de segurança à medida em que os investigadores se foram apercebendo que o controlo de propulsão é mais flexível do que as superfícies de controlo clássicas e que os veículos controlados por propulsão são propensos a uma estabilização de atitude e rastreamentos de trajetória altamente rápidos, levando a uma crescente popularidade de veículos voadores controlados por propulsão entre os investigadores.

A propulsão elétrica distribuída abre ainda mais oportunidades para aeronaves controladas por propulsão, introduzindo motores com respostas mais rápidas e com capacidade de tração adicional (uma vez que a maioria dos motores elétricos podem ser sobrecarregados por um curto período de tempo sem sobreaquecer e danificar o isolamento), garantindo flexibilidade de integração sem escala (eficiência, compacidade e confiabilidade em qualquer escala) e sem perda de potência à medida que a altitude aumenta. Além disso, a implementação da propulsão elétrica distribuída beneficia das vantagens do acoplamento aero-propulsivo(pressão dinâmica melhorada sobre a asa devido à distribuição das hélices ao longo da envergadura), redução de ruído com um impacto acústico substancialmente mais baixo e um impacto positivo no ambiente, tendo em conta que os sistemas de propulsão elétricos usufruem de melhor eficiência na conversão de energia e são considerados ecológicos.

Assim sendo, o conceito do sistema de propulsão elétrica distribuída como atuador de controlo potencializa novos recursos para o projeto, eficiência e robustez de futuras aeronaves, melhorando o desempenho dos projetos convencionais, incluindo a redução das superfícies de controlo tradicionais e da vulnerabilidade do sistema de controlo da aeronave a casos de falha de motores.

Deste modo, o presente trabalho aborda a questão do controlo robusto da dinâmica latero-direcional para uma aeronave controlada por propulsão com incertezas de parâmetros, com o objetivo de entender como controlar uma aeronave de forma robusta através do seu sistema de propulsão elétrica distribuída e como usar essa capacidade para introduzir melhorias no projeto de aeronaves. Concretamente, a questão central concentra-se no projeto de um controlador híbrido robusto, capaz de lidar com um modo de operação independente de controlo por propulsão e um modo convencional, combinando, se necessário, o controlo por propulsão e a operação das superfícies de controlo.

Dada a importância de certas propriedades chave do sistema permanecerem praticamente inalteradas quando sujeitas a perturbações nos sistemas de controlo da aeronave, garantir a robustez do controlador era um pré-requisito essencial para este trabalho, pois pretendia-se obter um controlador que atenda às especificações de projeto em condições normais de operação do sistema e garanta desempenho satisfatório na presença de distúrbios.

Para entender devidamente a validade do controlador de propulsão desenvolvido neste trabalho, foram comparados dois casos de estudo - uma aeronave com controlo convencional (Tecnam P2006T) e uma modificação da mesma aeronave para permitir o controlo distribuído por propulsão. Duas soluções possíveis para a implementação do controlo por propulsão foram identificadas: tração vetorial e tração diferencial/assimétrica. O autor optou por implementar a última, que consiste em adicionar mais tração de um lado que o outro, a fim de virar a aeronave no sentido da menor tração.

Os parâmetros para projetar o segundo caso foram obtidos por meio de uma breve e elementar estimativa analítica, com base nos métodos de projeto conceitual, considerando os impactos da modificação no peso, momentos e produtos de inércia, arrasto, desempenho na fase de descolagem e derivadas de controlo e estabilidade.

Os métodos propostos são então validados através de simulações computacionais de dois casos de estudo em cenários de voo realistas, tais como várias curvas coordenadas niveladas e uma falha crítica do motor.

Em resumo, este trabalho permitiu esclarecer o potencial da tecnologia de propulsão elétrica distribuída como um atuador de controlo, abordando a questão do controlo do movimento latero-direcional. Como a tecnologia mencionada possui zero emissões de operação, foi dado um passo no sentido de reduzir nossa pegada ambiental, num momento em que a necessidade de soluções ambientalmente responsáveis na aviação é uma preocupação incontestável. Estes novos desenvolvimentos abrem inúmeras oportunidades para novas pesquisas sobre o tema, aprimorando a visão de um futuro melhor e de uma aviação sustentável, estimulando o surgimento de projetos novos e mais flexíveis e dando uso a novas abordagens científicas e tecnológicas.

# Abstract

Fixed-wing flying vehicles are usually controlled by means of control surfaces such as elevator, ailerons, and rudder. These surfaces are operated by hydraulic and/or electric actuators. In case of failure of the control surface systems (i.e., control actuators and coupling devices), the aircraft may suffer damages leading to severe or even fatal crashes.

An increasing history of accidents and incidents motivated researchers to investigate the use of propulsion as an emergency flight control and ever since researches on propulsion controlled flying vehicles have gained increased popularity in the last decades, expanding from safety purposes only as investigators realised propulsion control is more flexible than classical control surfaces and propulsion controlled vehicles are prone to highly fast attitude stabilisation and trajectory tracking.

Distributed electric propulsion opens even further opportunities for propulsion controlled aircraft, introducing faster response engines with additional thrust capability, granting scale-free integration flexibility and no power lapse as altitude increases. Also, the DEP implementation profits from aero-propulsive coupling benefits, noise reduction with a substantially lower acoustic impact and a positive impact on the environment.

Thus, the emergence of the DEP system concept as a control actuator potentiates new capabilities for future aircraft's design, efficiency and robustness, improving the performance of conventional designs, including reducing the traditional control surfaces and decreasing the aircraft's control system vulnerability to engine-out cases.

Hence, the present work addresses the issue of robust lateral-directional dynamics control for a propulsion controlled aircraft with parameter uncertainties, aiming to understand how to robustly control an aircraft through its distributed electric propulsion system and how to use this capability to introduce improvements in an aircraft's design. Concretely, the core issue focuses on designing a hybrid robust roll-yaw controller which is able to deal with a standalone propulsion control operation mode as well as a conventional mode, combining, if needed, both propulsion control and control surface operation.

The proposed methods are then validated through computational simulation on realistic flight scenarios, namely several levelled coordinated turns and a critical engine failure. Thus, this work shines a light on the distributed electric propulsion technology potential as a control actuator, taking a step towards reducing our environmental footprint in a time where the need for environmentally responsible solutions in aircraft technology is an indisputable concern.

# Keywords

Robust propulsion control, H-infinity control, Lateral-directional flight dynamics, Parameter uncertainties, Distributed Electric Propulsion.

# Contents

# List of Figures

# List of Tables

# Nomenclature

| | |
|---|---|
| $\alpha$ | aircraft's angle of attack |
| $\alpha_n$ | nacelle angle of attack |
| $\alpha^*$ | equilibrium state angle of attack |
| $a$ | acceleration |
| $A$ | state coefficient matrix |
| $A_h$ | horizontal empennage aspect ratio |
| $A_p$ | plant's state coefficient matrix |
| $A_{prop}$ | propeller disk area |
| $A_v$ | vertical empennage aspect ratio |
| $A_w$ | wing aspect ratio |
| | |
| $\beta$ | sideslip angle |
| $b_v$ | vertical empennage span |
| $b_w$ | wing reference span |
| $B$ | driving matrix |
| $B_p$ | plant's driving matrix |
| | |
| $c_{d_c}$ | experimental steady state cross-flow drag |
| $(c_{l_{\delta_r}})_{theory}$ | theoretical rudder side force effectiveness |
| $c_{l_{\alpha_v}}$ | vertical empennage airfoil lift curve slope |
| $c_v$ | vertical empennage mean-chord |
| $c_w$ | wing mean-chord |
| $C$ | output/observation matrix |
| $C_D$ | drag force coefficient |
| $C_{D_\alpha}$ | drag due to angle of attack derivative |
| $C_{D_0}$ | aircraft zero-lift drag coefficient |
| $C_{D_{0_{nb}}}$ | zero-lift drag coefficient of the base of the nacelle |
| $(C_{D_{0_n}})$ | nacelle zero-lift drag coefficient |

| | |
|---|---|
| $C_{D_{0_v}}$ | vertical empennage zero-lift drag coefficient |
| $C_{D_{b_n}}$ | nacelle base-drag coefficient |
| $C_{D_{L_n}}$ | nacelle drag coefficient due to lift |
| $C_{D_{L_v}}$ | vertical empennage drag coefficient due to lift |
| $C_{D_n}$ | nacelle drag coefficient |
| $C_{D_v}$ | subsonic vertical empennage drag coefficient |
| $C_{f_n}$ | turbulent flat plate friction coefficient of the nacelle |
| $C_{f_v}$ | turbulent flat plate friction coefficient of the vertical empennage |
| $C_l$ | roll moment coefficient |
| $C_{l_\beta}$ | rolling moment due to sideslip derivative |
| $C_{l_{\beta_v}}$ | vertical tail contribution to the rolling moment due to sideslip derivative |
| $C_{l_{\delta_a}}$ | rolling moment due to aileron deflection derivative |
| $C_{l_{\delta_r}}$ | rolling moment due to rudder deflection derivative |
| $C_{l_p}$ | rolling moment due to roll rate derivative |
| $C_{l_{p_v}}$ | vertical tail contribution to the rolling moment due to roll rate derivative |
| $C_{l_r}$ | rolling moment due to yaw rate derivative |
| $C_{l_{r_v}}$ | vertical tail contribution to the rolling moment due to yaw rate derivative |
| $C_L$ | lift force coefficient |
| $C_{L_0}$ | zero angle of attack lift coefficient |
| $C_{L_\alpha}$ | slope of the lift curve |
| $(C_{L_\alpha})_v$ | lift-curve slope of the vertical panel, determined with the effective aspect ratio of the vertical empennage |
| $C_{L_{a_v}}$ | vertical empennage lift curve slope |
| $C_{L_{sec}}$ | wing section's lift force coefficient |
| $C_m$ | pitch moment coefficient |
| $C_{m_\alpha}$ | pitching moment due to angle of attack derivative |
| $C_{m_{\delta_e}}$ | pitching moment due to stabilator deflection derivative |
| $C_{m_0}$ | pitching moment at zero angle of attack |
| $C_{m_q}$ | pitching moment due to pitch rate derivative |
| $C_n$ | yaw moment coefficient |
| $C_{n_\beta}$ | yawing moment due to sideslip derivative |

| | |
|---|---|
| $C_{n_{\beta_v}}$ | vertical tail contribution to the yawing moment due to sideslip derivative |
| $(C_{n_\beta})_{WB}$ | contribution of the wing-body combination to the total yawing moment due to sideslip |
| $C_{n_{\delta_a}}$ | yawing moment due to aileron deflection derivative |
| $C_{n_{\delta_r}}$ | yawing moment due to rudder deflection derivative |
| $C_{n_p}$ | yawing moment due to roll rate derivative |
| $C_{n_{p_v}}$ | vertical tail contribution to the yawing moment due to roll rate derivative |
| $C_{n_r}$ | yawing moment due to yaw rate derivative |
| $C_{n_{r_v}}$ | vertical tail contribution to the yawing moment due to yaw rate derivative |
| $C_p$ | plant's output/observation matrix |
| $C_T$ | thrust force coefficient |
| $C_X$ | axial force coefficient |
| $C_Y$ | side force coefficient |
| $C_{Y_\beta}$ | side force due to sideslip derivative |
| $C_{Y_{\beta_v}}$ | vertical tail contribution to the side force due to sideslip derivative |
| $C_{Y_{\delta_a}}$ | side force due to aileron deflection derivative |
| $C_{Y_{\delta_r}}$ | side force due to rudder deflection derivative |
| $C_{Y_p}$ | side force due to roll rate derivative |
| $C_{Y_{p_v}}$ | vertical tail contribution to the side force due to roll rate derivative |
| $C_{Y_r}$ | side force due to yaw rate derivative |
| $C_{Y_{r_v}}$ | vertical tail contribution to the side force due to yaw rate derivative |
| $\Delta C_{Y,rudder}$ | increment in airfoil subsection maximum side force coefficient due to the rudder deflection |
| $(\Delta C_{Y_\beta})_v$ | side force due to sideslip of the vertical empennage coefficient |
| $C_Z$ | normal force coefficient |
| | |
| $\delta_a$ | aileron deflection |
| $\delta_e$ | stabilator deflection |
| $\delta_r$ | rudder deflection |
| $\delta_t h$ | throttle position |
| $d$ | disturbance vector |
| $d_b$ | nacelle base diameter |

| | |
|---|---|
| $d_n$ | maximum nacelle diameter |
| $D$ | direct matrix |
| $D$ | drag force |
| | |
| $\xi$ | damping |
| $\eta$ | ratio of the drag of a finite cylinder to the drag of an infinite cylinder |
| $\eta_P$ | propellers's efficiency |
| $\varepsilon$ | tunning constant |
| $\varepsilon_{turn}$ | coordinated turn tracking error |
| $\varepsilon_{T_e}$ | engine angle of incidence |
| $E$ | disturbance associated matrix |
| | |
| $F_{T_{e_n}}$ | difference between each engine wing affected section's weight and lift forces |
| | |
| $\gamma$ | aircraft's trajectory in relation to the horizontal local plane |
| $\gamma$ | attenuation constant |
| $\gamma_{climb}$ | climb angle |
| | |
| $\bar{h}$ | distance from the centre Earth's globe to the aircraft |
| $h_{fus}$ | fuselage height |
| $h_{obstacle}$ | obstacle height |
| $h_{TR}$ | transition phase reached height |
| $H$ | hamiltonian structure of a given algebraic Riccati equation |
| | |
| $Ixx$ | rolling mass moment of inertia |
| $Ixy$ | roll-pitch product of inertia |
| $Iyy$ | pitching mass moment of inertia |
| $Iyz$ | pitch-yaw product of inertia |
| $Izx$ | yaw-roll product of inertia |
| $Izz$ | yawing mass moment of inertia |

| | |
|---|---|
| $J$ | cost function |
| $k$ | empirical factor |
| $k_v$ | empirical factor |
| $K$ | feedback gain |
| $K'$ | empirical correction factor for nonlinear effects at high rudder deflections |
| $K_{drag}$ | drag due to lift factor |
| $K_b$ | effect of taper ratio and rudder span correction factor |
| $K_\Lambda$ | an empirically derived correction factor that accounts for the effects of vertical tail planform |
| $K_N$ | empirical factor related to the sideslip derivative for body plus wing-body interference |
| $K_{R_l}$ | empirical Reynolds-number factor |
| $\lambda$ | eigenvalues of a given matrix |
| $\bar{\lambda}$ | aircraft's longitude |
| $\Lambda_{1/4_v}$ | vertical empennage quarter chord sweep angle |
| $\Lambda_{c/4}$ | wing quarter chord sweep angle |
| $l_B$ | length of the body |
| $l_{fus}$ | fuselage length |
| $l_n$ | nacelle length |
| $l_v$ | distance parallel to the longitudinal axis between the vehicle centre of gravity and the quarter-chord point of the MAC of the vertical empennage |
| $l_{x_{sec}}$ | distance distance parallel to the longitudinal axis between the vehicle's and each section's centre of gravity |
| $l_{x_T}$ | distance parallel to the longitudinal axis between the vehicle's and the engine's centre of gravity |
| $l_{y_T}$ | distance perpendicular to the longitudinal axis between the vehicle's and the engine's centre of gravity |
| $L$ | lift force |
| $L'$ | airfoil thickness location parameter |
| $\bar{L}$ | roll moment |
| $L_{sec}$ | lift force in the engine wing affected section |

| | |
|---|---|
| $L_T$ | thrust roll moment |
| $\mu$ | rolling-friction coefficient |
| $m$ | total number of failed engines |
| $M$ | pitch moment |
| $M_T$ | thrust pitch moment |
| $n$ | load factor |
| $n_{ult}$ | design ultimate load factor |
| $N$ | yaw moment |
| $\bar{N}$ | total number of engines of the aircraft |
| $N_\beta$ | yaw moment generated by the sideslip |
| $N_D$ | drag produced by the failed engine |
| $N_E$ | engine yaw moment |
| $N_V$ | yaw moment generated by the vertical tail |
| $N_T$ | thrust yaw moment |
| $\omega_n$ | natural frequency |
| $\phi$ | roll/bank angle |
| $\dot{\phi}$ | roll/bank rate |
| $\varphi$ | aircraft's latitude |
| $\psi$ | yaw/turn angle |
| $\dot{\psi}$ | yaw/turn rate |
| $p$ | aircraft angular body rate |
| $P$ | unique positive-definite solution of a given algebraic Riccati equation |
| $P_O$ | engine's power for the set throttle, at sea level |
| $P_e$ | engine's power |
| $P_{ef}$ | probability of an engine failure |
| $P_{max}$ | engine's maximum power |

| | |
|---|---|
| $q$ | aircraft angular body rate |
| $Q$ | state weighting matrix |
| $\bar{Q}$ | dynamic pressure |
| $\rho$ | atmospheric density |
| $r$ | aircraft angular body rate |
| $\mathbb{R}$ | real numbers |
| $R$ | control weighting matrix |
| $R_{LS}$ | lifting surface correction factor |
| $R_{turn}$ | radius of turn |
| $R_{TR}$ | radius of the transition phase circular path |
| $R_{wf}$ | wing/fuselage interference factor |
| $\sigma$ | standard deviation |
| $S_{b_n}$ | nacelle base area |
| $S_{B_S}$ | projected side area of the body |
| $S_C$ | climb field length |
| $S_G$ | level ground roll field length |
| $S_R$ | rotation ground roll field length |
| $S_h$ | horizontal empennage area |
| $S_n$ | nacelle maximum frontal area |
| $S_{plf_n}$ | nacelle planform area |
| $S_{sec}$ | wing section area |
| $S_{TO}$ | total take-off field length |
| $S_{TR}$ | transition to climb field length |
| $S_v$ | vertical empennage area measured to the body centre-line |
| $S_w$ | wing reference area |
| $S_{wet_n}$ | wetted area of the nacelle |
| $S_{wet_v}$ | wetted area of the vertical empennage |
| $\tau$ | time constant |

| | |
|---|---|
| $\tau_e$ | engine's time constant |
| $\dot{\theta}$ | aircraft attitude rate |
| $t$ | time |
| $t_{r_h}$ | horizontal empennage maximum root thickness |
| $t_{r_v}$ | vertical empennage maximum root thickness |
| $t_{Tr}$ | engine's Thrust response/settling time |
| $t_{turn}$ | time to complete one turn |
| $T$ | thrust force |
| $T_{\frac{1}{2}}$ | time to halve |
| $T_2$ | time to double |
| $T_E$ | thrust of each engine |
| | |
| $u$ | control vector |
| $u^*$ | non-linear equilibrium (or trimmed) control vector |
| $\bar{u}$ | linear equilibrium (or trimmed) control vector |
| $U$ | controllability matrix |
| | |
| $v$ | lateral component of the flight velocity |
| $v_i$ | induced velocity |
| $V$ | flight velocity |
| $V_\infty$ | airspeed |
| $V_A$ | maneuvering speed |
| $V_{max}$ | maximum speed at sea level |
| $V_{MCG}$ | minimum control speed on ground |
| $V_{NE}$ | never exceed speed |
| $V_S$ | stall speed |
| $V_{TR}$ | transition velocity |
| | |
| $W_e$ | engine weight |
| $W_{empty}$ | empty/equipped weight |
| $W_h$ | horizontal empennage weight |

| | |
|---|---|
| $W_n$ | nacelle weight |
| $W_{TO}$ | take-off weight |
| $W_{useful}$ | standard useful load |
| $W_v$ | vertical empennage weight |
| $W_w$ | wing weight |
| $W_{w_{sec}}$ | wing section's weight |
| | |
| $\chi$ | flight path angle in relation to geodetic North |
| $x$ | state vector |
| $\bar{x}$ | linear equilibrium (or trimmed) state vector |
| $x^*$ | non-linear equilibrium (or trimmed) state vector |
| $x_e$ | integrator's state vector |
| $x_p$ | plant's state vector |
| $X$ | axial force |
| $X_{cg_a}$ | maximum aft axial cg position |
| $X_{cg_f}$ | maximum forward axial cg position |
| $X_T$ | thrust axial force |
| | |
| $y$ | output vector |
| $y_E$ | distance perpendicular to the longitudinal axis between the vehicle centre of gravity and the active engine |
| $Y$ | side force |
| $Y_T$ | thrust side force |
| | |
| $z$ | vertical distance between the wing's root quarter chord point and the aircraft's center of gravity |
| $z_f$ | maximum fuselage depth |
| $z_v$ | vertical distance between the vertical tail's aerodynamic centre and the aircraft's centre of gravity |
| $z_w$ | distance from wing root quarter chord point to the fuselage centreline |
| $Z$ | normal force |
| $Z_T$ | thrust normal force |

| | |
|---|---|
| $\frac{(\alpha_{\delta_r})_{C_L}}{(\alpha_{\delta_r})_{c_l}}$ | effect of aspect ratio and rudder-chord ratio on the three dimensional rudder effectiveness |
| $\frac{c_{l_{\delta_r}}}{(c_{l_{\delta_r}})_{theory}}$ | empirical correction factor |
| $\frac{S_v}{S_w}$ | ratio of the vertical empennage area (measured to the body centre-line) to the total wing area |
| $\frac{S_{v_f}}{S_v}$ | the ratio of the rudder-affected vertical tail area to the total vertical tail area |
| $\frac{t}{c}$ | maximum thickness ratio associated wit the vertical empennage airfoil |
| $\left(1+\frac{\partial\sigma}{\partial\beta}\right)\cdot\frac{q_v}{q_\infty}$ | parameter representing the wake and sidewash effects |

# Acronyms List

| | |
|---|---|
| AFCS | Automatic Flight Control System |
| BWB | Blended Wing Body |
| C-MAPSS | Commercial Modular Aero-Propulsion System Simulation |
| CAD | Computer-Aided Design |
| DEEC | Digital Flight Control Computer |
| DEP | Distributed Electric Propulsion |
| DFCC | Digital Electronic Engine Controls |
| DoF | Degrees of Freedom |
| DP | Distributed Propulsion |
| EAIC | Electronic Air Inlet Controllers |
| FAR | Federal Aviation Regulation |
| FPCC | Flight Propulsion Control Coupling |
| ICCT | International Council on Clean Transportation |
| IFSD | In-Flight Shutdown |
| LEAPTech | Leading Edge Asynchronous Propeller Technology |
| LQR | Linear Quadratic Regulator |
| LTR | Loop Transfer Recovery |
| MDO | Multi-Disciplinary Design Optimisation |
| MIMO | Multiple Input Multiple Output |
| NASA | National Aeronautics and Space Administration |
| OpenVSP | Open Vehicle Sketch Pad |
| PCA | Propulsion Controlled Aircraft |
| PID | Proportional-Integral-Derivative |
| PSC | Performance Seeking Control |
| SI | International System of Units |
| TeDP | Turboelectric Distributed Propulsion |
| TOC | Throttles-Only Control |
| UAV | Unmanned Aerial Vehicle |
| UBI | Universidade da Beira Interior |
| US | United States |
| USAF | United States Air Force |
| VTOL | Vertical Take-off and Landing |

# Chapter 1

## Introduction

Fixed-wing flying vehicles are usually controlled by means of control surfaces such as elevator, ailerons, and rudder. These surfaces are operated by hydraulic and/or electric actuators and in case of failure of those control systems (i.e. control actuators and coupling devices), the aircraft may suffer catastrophic damages.
For over 50 years, multiple aircraft have faced major flight control system failures which led to severe or even fatal crashes, resulting in over 1200 lives lost. The increasing history of accidents and incidents motivated researchers to investigate the use of propulsion as an emergency flight control by conducting simulator, flight and analytical studies on the matter. A summary of these accidents can be found bellow.

Table 1.1: Systems failed and operating for accidents and incidents in which engine thrust was or could have been used for control. [24]

| Accident/Incident | | Aileron | Rudder | Elevator | Engines | Fatalities |
|---|---|---|---|---|---|---|
| June 8, 1966 | North American XB-70, USAF | yes | no | no | all OK | 1 |
| 1970 – 1980 | Vietnam War Statistics, Southeast Asia Losses | – | – | – | – | ≈ 1800 |
| June 12, 1972 | McDonnell Douglas DC-10, American Airlines Flight 96 | yes | no | yes | one out | – |
| April 4, 1973 | Lockheed C-5A, USAF Operation Babylift | yes | no | no | all OK | 155 |
| March 3, 1974 | McDonnell Douglas DC-10, Turkish Airlines Flight 981 | yes | no | no | all OK | 346 |
| May 30, 1974 | Boeing B-52H, USAF | yes | no | no | all OK | – |
| April 12, 1977 | Lockheed L-1011 Tristar, Delta Air Lines Flight 1080 | yes | yes | yes | all OK | – |
| November 29, 1981 | Boeing B-52G, USAF | yes | no | no | all OK | – |
| August 12, 1985 | Boeing 747, Japan Airlines Flight 123 | no | no | no | all OK | 520 |
| July 19, 1989 | McDonnell Douglas DC-10, United Airlines Flight 232 | no | no | no | center out | 111 |
| February, 1991 | Fairchild Republic A-10, USAF Operation Desert Storm | yes | no | no | all OK | – |
| November 12, 2001 | Airbus A300-600, American Airlines Flight 587 | yes | no | yes | all OK | 260 |
| May 29, 2000 | McDonnell Douglas F/A-18, US Navy | no | no | no | all OK | – |
| November 22, 2003 | Airbus A300, DHL | no | no | no | all OK | – |
| March 6, 2005 | Airbus A320, Air Transat Flight 961 | yes | no | yes | all OK | – |

Plenty of interesting data came from thorough examinations of those casualties: the potential of using thrust for control expanded from safety purposes only to design optimisation benefits, leading to an increased popularity of propulsion controlled flying vehicles amongst researchers. Distributed electric propulsion (DEP) opens even further opportunities for propulsion controlled aircraft, introducing faster response engines with additional thrust capability (since the majority of electric motors can be overloaded for a short period of time without overheating and damaging the insulation), granting scale-free integration flexibility (efficiency, compactness, high power to weight and reliability at any scale) and no power lapse as altitude increases. Also, the DEP implementation profits from aero-propulsive coupling benefits (enhanced dynamic pressure over the wing due to the propellers being distributed along the wingspan), noise reduction with a substantially lower acoustic impact and a positive effect on the environment, as electric propulsion systems advantageously have better energy conversion efficiency and are considered environmentally friendly. Thus, the emergence of the DEP system concept as a control actuator potentiates new capabilities for future aircraft's design, efficiency and robustness, improving the performance of conventional designs, including reducing the traditional control surfaces and decreasing the aircraft's control system vulnerability to engine-out cases.
Also, propulsion control is considerably more flexible than classical control surfaces, as propulsion controlled vehicles are prone to highly fast attitude stabilisation and trajectory tracking. The author acknowledges this potential but also the challenges of control-authority limitations of the standalone propulsion control operation mode, therefore hypothesising that propulsion control might not be sufficient for full lateral-directional flight dynamics. This assumption will lead to the a priori design of a hybrid mode, although conventionally before designing the hybrid control mode, one should demonstrate that the propulsive standalone control is insufficient.
Hence, the present work addresses the issue of robust lateral-directional dynamics control for a hybrid distributed electric propulsion controlled aircraft with parameter uncertainties. Concretely, the core issue focuses on designing a hybrid robust roll-yaw controller which is able to deal with a standalone propulsion control operation mode as well as a conventional mode, combining, if needed, both propulsion control and control surface operation. The proposed methods are then validated through computational analytical methods and simulation on realistic flight scenarios.

## 1.1 Objectives

Motivated to investigate the aforementioned problematic, addressing the issue of lateral-directional dynamics propulsion control, this work aims at answering the following questions:

1. **How to robustly control an aircraft through its distributed electric propulsion system?**
2. **How to use this capability to introduce improvements in an aircraft's design?**

However, answering these two questions is rather challenging, since they involve examining different aspects of the propulsion control system and its integration. Therefore, those research questions were broken into sub questions, setting smaller goals by separating the different aspects that influence the conclusions of this thesis.

Breaking down the first question, this work intents to answer the subsequent points:

- What is the generic relevance of the model used?
- Was that model appropriately chosen?

- Which gain design is more suitable in terms of robustness for this study: $LQR$ or $H_\infty$?
- How will the propulsion controller be structured?
- Can the standalone propulsion mode handle a coordinated turn? To what extent?
- Can the standalone propulsion mode handle engine failures? To what extent?
- Which control authority limitations are implied in the standalone propulsion mode?

Similarly, breaking down the second question into seven topics:

- What are the improvements in terms of weight?
- What are the improvements in terms of drag?
- What are the improvements in terms of vertical empennage sizing?
- Will the improvements worsen the aircraft's take-off field length?
- What is the generic relevance of those improvements?
- How conservative are the results?
- What are the certification/implementation challenges associated with those improvements?

## 1.2 Principles of aircraft control

Aircraft control can be described as a loop chain between the pilot, actuators and sensors. Thus, the actuators function as control organs to apply the forces and moments needed to generate and correct the movement of the airplane. Sensors provide information about the flight, aircraft motion and its states and the pilot (or control system) closes the chain by controlling the aircraft: operating the actuators based on the information provided by the sensors, in order to meet the specific objectives of the flight. The sensors and actuators used to transmit the information are hence key elements whose quality, accuracy and reliability establishes the quality of the control achieved.

The majority of actuators used in flight control are intended for control surface positioning. These surfaces change the pattern of air flowing and pressure distribution over and around the aircraft and can be subdivided into two groups: primary and secondary. The primary (or conventional) control surfaces are the ones required to safely control the three axes of the aircraft's body frame in-flight, which include the elevators, rudder and ailerons. Secondary control surfaces, high lift devices such as flaps, spoilers, trim tabs, slats and winglets, are meant to improve the aircraft's performance and/or alleviate control loading.

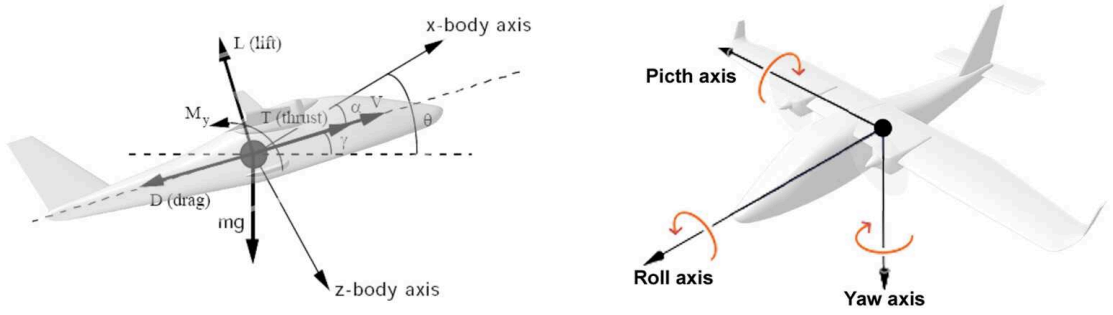


Figure 1.1: Body-fixed right handed coordinate and axis system.

In this work, a body-fixed right handed coordinate system (Figure 1.1) will be used to define the aircraft's motion, the angles defined by the right handed rotation about the three axes of a right handed system of axes are the Euler angles: $\theta$, $\phi$ and $\psi$.

The relation between the aircraft angular body rates $p, q, r$ and the attitude rates, $\dot{\phi}$, $\dot{\theta}$, $\dot{\psi}$ referred to datum axes is the following

$$p = \dot{\phi} - \dot{\psi} \cdot sen(\theta) \tag{1.1}$$
$$q = \dot{\theta} \cdot cos(\phi) + \dot{\psi} \cdot cos(\theta) \cdot sen(\phi) \tag{1.2}$$
$$r = \dot{\psi} \cdot cos(\phi) \cdot cos(\theta) - \dot{\theta} \cdot sen(\phi) \tag{1.3}$$

And,

$$\dot{\phi} = p + (q \cdot sen(\phi) + r \cdot cos(\phi)) \cdot tan(\theta) \tag{1.4}$$
$$\dot{\theta} = q \cdot cos(\phi) - r \cdot sen(\phi) \tag{1.5}$$
$$\dot{\psi} = \frac{q \cdot sen(\phi) + r \cdot cos(\phi)}{cos(\theta)} \tag{1.6}$$

The forces acting on the aircraft are the axial force ($X$), the side force ($Y$) and the normal force ($Z$). These forces can be defined according to the following coefficients

$$C_X = \frac{X}{\bar{Q} \cdot S_w} \tag{1.7}$$
$$C_Y = \frac{Y}{\bar{Q} \cdot S_w} \tag{1.8}$$
$$C_Z = \frac{Z}{\bar{Q} \cdot S_w} \tag{1.9}$$

where,
$Q$ is the dynamic pressure.
$S_w$ is the wing reference area.

These forces relate to the aerodynamic reference forces: Lift ($L$), Thrust ($T$) and Drag ($D$), according to the following equations

$$C_X = C_L \cdot sin(\alpha) + C_T \cdot cos(\alpha) - C_D \cdot cos(\alpha) \tag{1.10}$$
$$C_Z = -C_L \cdot cos(\alpha) + C_T \cdot sin(\alpha) - C_D \cdot sin(\alpha) \tag{1.11}$$

where,
$\alpha$ is the aircraft's angle of attack.

The moments acting on the aircraft are the pitch moment ($M$), the roll moment ($\bar{L}$) and the yaw moment ($N$), expressed in the coefficient form

$$C_m = \frac{M}{\bar{Q} \cdot S_w \cdot c_w} \tag{1.12}$$
$$C_l = \frac{\bar{L}}{\bar{Q} \cdot S_w \cdot b_w} \tag{1.13}$$
$$C_n = \frac{N}{\bar{Q} \cdot S_w \cdot b_w} \tag{1.14}$$

where,
$b_w$ is the aircraft's wing reference span.
$c_w$ is the aircraft's wing mean-chord.

The pitch moment defines the longitudinal symmetric dynamic motion of the aircraft around the horizontal axis, in which the centre of gravity moves in a vertical plane. This moment is controlled by the elevators, control surfaces which adjust the aircraft's altitude by generating a normal force and causing the aircraft to ascent or descent.

Roll and yaw are the moments relative to the lateral-directional asymmetrical dynamic motion of the aircraft, object of study in this work.

Roll motion is the movement around the horizontal axis that enables the aircraft's bank angle control. For achieving this lateral control, the ailerons (installed at the outer trailing edge of each wing) operate symmetrically opposite to one another, generating differential lift and, therefore, induced drag forces on each wing. The downwards deflected aileron increases the airflow exposed camber of the respective wing, increasing the wing velocity and generating more lift, while the upwards deflected aileron decreases that convexity, resulting in a lift reduction on that wing. As more lift is generated in one wing than the other, a rolling moment develops in the direction of the dropping wing, as the higher lift wing moves upwards. To maximise the moment's lever arm length, ailerons are more efficient when located at the wingtips.

Yaw motion is the movement around the vertical axis that grant's the aircraft with heading control. For achieving this directional control, the rudder (installed at the trailing edge of the vertical stabiliser) is used to generate an aerodynamic side force, similar to the production of lift by the wings. Essentially, when the rudder surface is deflected, the static pressure on the deflected-direction's side is increased while that on the opposite side is decreased, this pressure differential causes a pull force on the vertical stabiliser which results in yaw rotation. The rudder's efficiency is directly proportional to the speed of its surrounding airflow, thus the aircraft's directional control is more effective at higher speeds.

Ideally roll and yaw motions are achieved separately, however, these motions are not independent and one generates the other. A roll motion is triggered as the aircraft yaws due to the differential air-flowing exposure on the wings, that unbalances the lift produced by each wing and induces a bank angle towards the respective yaw-turn direction. Similarly, a yaw motion is triggered as the aircraft rolls due to the horizontal component of the "diagonal" lift generated by the rising wing, inducing a yaw angle towards the dropping-wing's direction. This induced aircraft yaw is desirable as it increases the aircraft's roll rate, and is higher for aircraft with higher directional stability characteristics.

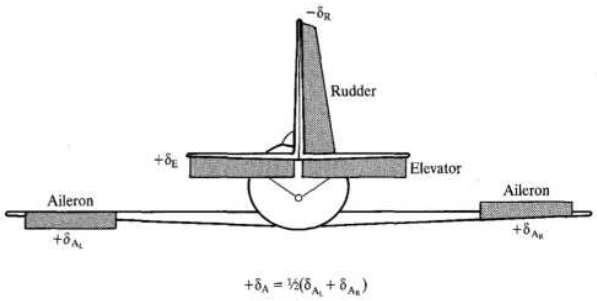


Figure 1.2: Positive convention for control surfaces deflection. [1]

Illustrated in Figure 1.2, the deflection of these surfaces (elevators, ailerons and rudder) is quantified by three angles ($\delta_e$, $\delta_a$ and $\delta_r$, respectively), by convention, the direction of the positive deflections is that which produces a negative moment, hence positive roll is right wing down, positive pitch is nose up and positive yaw is nose to the right as seen by the pilot.

### 1.2.1 Modern control theory

Aircraft have six degrees of freedom: three associated with the aircraft's centre of gravity translation and three associated with angular motion about the centre of gravity (Euler angles). The ability to change an aircraft's current state of motion is achieved through control surfaces deflection or a change in thrust, which can be obtained from the engines. In order for an aircraft to fly a straight and level flight, constant attitude corrections must be made — either through the pilot's commands or an automatic flight control system (AFCS).

Classical controllers such as proportional-integral-derivative (PID) show ineffectiveness in the presence of system model uncertainties, sensor inaccuracies, and external disturbances. Modern control theory uses the time-domain state space representation to solve control problems, where the aircraft's motion states are described as vectors in function of time and the system under analysis (plant) is represented by differential equations, both linear and non-linear. The evolution of modern computer simulation techniques enable solving increasingly complex control problems with multiple inputs and outputs (MIMO) in a convenient and compact way, with real-world (non-linear) context application, further simplifications can be implemented as those equations may be represented in matrix form (for linear systems).

A way of regulating the output of the plant to a specific set point or to make it track a changing command is through a negative feedback connection, forming a closed loop around the plant. Feedback can be defined as returning a signal obtained from a system's output to its input. In aircraft control, this negative loop compares the pilot or AFCS commanded motion with the measured motion, information provided by the aforementioned sensors, and uses that feedback to compute the control law and apply the respective gains, generating signals to the actuators to produce the control surfaces deflection or throttle setting needed to achieve the commanded motion.

The loop ends when the aircraft's measured motion corresponds to the commanded motion. In tracker and regulator applications, negative feedback changes the plant's behaviour, promoting equilibrium settling and reducing perturbation's effects. Usually, integrated flight control systems are a group of several AFCS modes (sideslip suppression augmentation, pitch attitude hold, auto-throttle, Mach hold, altitude hold, coordinated turn, et cetera) integrated in a single system, where the pilot selects particular modes according with the required task or phase of flight.

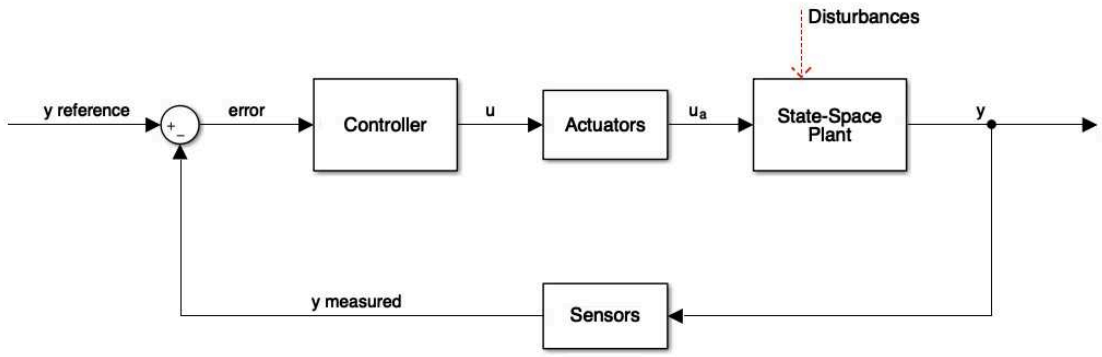


Figure 1.3: Closed loop negative feedback control system structure.

A general structure of a closed loop negative feedback control system can be represented as described in the block schematics of Figure 1.3, accounting for the controller, actuators, plant (including disturbances) and sensors.

Diverse control strategies may be implemented in order to compute de control law and gains, according to the desired controller specifications and the model considered, although in any case they must always guarantee stability in the closed loop behaviour. As aircraft system's behaviour varies significantly throughout normal operation, several different control laws are implemented, one for each behaviour mode. One of the biggest challenges in control design is precisely designing a control system that enables a stable mild transition between operation modes.
One commonly used strategy is robust control, which is able to endure uncertainty in the system's model and still perform effectively. An example of a modern robust control approach is the $H_\infty$ technique. A less recent strategy is optimal control, whose control signal optimises a determined cost function. A fairly wide used example of this method is the Linear Quadratic Regulator (LQR) technique. Both of these strategies will be adopted and compared in this work.

## 1.3 Outline

This thesis is divided into six chapters, organised as follows.

In Chapter 2 the state of the art on propulsion controlled systems for fixed-wing aircraft is reviewed, addressing the strengths and limitations of commonly used methods. This review also emphasises the peculiarities of aircraft with distributed electric propulsion systems.

In Chapter 3 two case study aircraft are presented, where the second case study is obtained from a DEP implementation study performed on the first. This study assesses the impacts of the implementation of a distributed electric propulsion controller on aircraft design. Also, the parameters for the DEP aircraft are analytically estimated and the respective applied methods validated.

In Chapter 4 the full dynamics of the aircraft is modelled, focusing on the gain design and structure of both cases' lateral-directional controllers. The gain for both an $LQR$ and an $H_\infty$ controllers is designed and its performance compared for case I, in order to prove the $H_\infty$ controller robustness and validate the controller selection. Afterwards, the corresponding conventional (control-surface actuation) controller structure is specified. For case II, the previously validated $H_\infty$ gain design is computed, and the hybrid-controller specifications as well as the corresponding structure (with a standalone propulsion control operation mode as well as a conventional mode) are described.

In Chapter 5 besides a coordinated turn simulation, a critical engine failure is also simulated for each case study and an evaluation of the results regarding the aircraft's manoeuvrability and control effectiveness is accessed and compared between the usage of conventional and propulsive controls.

In Chapter 6 the overall results from the previous chapters are analysed, assessing the strengths and limitations of the simulation and results, as well as the influence of the used methodologies in the overall conclusions. The oral presentation originated from this work is referred and guidance for further work on this research is provided.

# Chapter 2

# Critical review of Propulsion Controlled Systems

An aircraft's direction and attitude during the course of flight can be controlled by the pilot or auto-pilot through two types of changes:

- a change in the aircraft's aerodynamic configuration.
- a change in the aircraft's propulsive thrust.

The first identified change concerns the conventional aircraft control, where primary surfaces such as the ailerons, elevator and rudder provide control authority over the aircraft. The latter is the object of study of this work, where control authority is achieved through propulsive inputs. This authority can be provided either from the moment generated by the propulsive forces acting on the aircraft (essentially the thrust and propeller in-plane force) or from the interaction of the propulsive slipstream with the aircraft.
Traditionally, aircraft's flight and engine control systems operate independently from one another but the emergence of today's digital controllers, as well as multiplex data buses allowing communicating between them, has provided the means for automated integrated control solutions to optimize traditional flight control problems. Technological advances in system modelling and estimation techniques grant improved analytical tools for multivariable control law design. As so, numerous researches on integrated flight/propulsion control algorithms have been conducted, aiming to improve aircraft safety and performance.
In this Chapter the state of the art on propulsion controlled systems for fixed-wing aircraft is reviewed, addressing the strengths and limitations of commonly used methods with regard to robustness in the presence of model uncertainties, external disturbances, and sensor inaccuracies. This review also emphasises the peculiarities of aircraft with electrical distributed propulsion control systems.

## 2.1 Historical overview

Within the last century, an exponential development of aircraft control systems has been identified, beginning with the first powered flight in December 1903, achieved by the Wright brothers[26], whose success has been attributed to not only their systematic design approach, having built and used a wind tunnel, but also to the relevance they employed on their aircraft being controllable by the pilot rather than intrinsically stable. At this early point, many difficulties were still being faced when controlling aircraft, which, combined with a desire for longer flights, led to the development of the first aircraft autopilot *"Sperry Aeroplane Stabiliser"*, by the Sperry Gyroscope Company in 1912, with a proportional feedback scheme.[27]
Progress in aircraft design was greatly impulsed by World War I (1914-1918). However, at this time a human pilot was still capable of executing all the normal functions for controlling the aircraft, making the advances in automatic control slow. Even so, the development of autopilots endured, using pneumatic servomechanisms to position the control surfaces and gyroscopes as the reference sensor.[28]

Figure 2.1: 21-year-old Lawrence Sperry demonstrating his Sperry gyroscopic stabiliser on a Curtiss C-2, to win the *"Concours de la Securité en Aéroplane"* on June 18, 1914. [2]

In the 1930s, Wiley Post flew around the world in less than eight days with a triaxial Sperry autopilot (fully powered by engine-driven pumps providing hydraulic and pneumatic pressure) [29], as classical control theory was initiated — instigated by works like Black's "regeneration theory", Nyquist's frequency-domain stability criterion and Bode's complex-frequency-domain theory.
During World War II (1939-1945) and fomented by the need for radar tracking and gun-positioning servomechanism development, further advances in control theory were made. Flying at night and in bad weather conditions led to the development of navigation aids, revealing a necessity to couple these aids to the autopilot. Thus, in 1947, completely under the control of an autopilot, a transatlantic flight was made by a US Air Force C-53. [28]
The frequency response and transfer function concepts were gaining more popularity by the late 1940s, as the first analog computers became available. A major development in the design and analysis of control systems was W. R. Evans' root-locus technique (1948) [30], leading to stability and performance analysis of automatically controlled aircraft to be increasingly implemented by aircraft companies.
From 1946 to 1949, after making its first flight, the rocket-powered Bell X-1 aircraft achieved supersonic flight and reached an altitude of nearly 22000m (Figure 2.2). As in such aircraft most of its mass is concentrated along the longitudinal axis, and the speed-altitude envelope extension provoked great unpredicted variations in the dynamics of the aircraft, a number of them suffered from inertia coupling effects and spun out of control. [3] Besides the mentioned inertia coupling, many other factors contributed to the need for a more analytical approach to aircraft stability and control problems. Aircraft design innovation (mass properties, aerodynamic surfaces area, etc) caused changes in the natural modes of the aircraft, making them difficult for the pilot alone to control. Also, as the altitude limit of the aircraft was expanding, the damping of the natural modes tended to decrease, making it increasingly important to analytically predict the modes' frequency and damping.
In 1959, the X-15 rocket plane's first flight expanded the envelope for manned flight to beyond Mach 6 and above 95000m, being equipped with a Honeywell-designed adaptive control system that provided three-axis stability augmentation and a transition from aerodynamic control to reaction control. [3]
As the digital computer began to have a major impact on engineering in the early 1960s, the techniques of numerical analysis started having increasing importance, fostering the establishment of modern control theory.
On account of the digital computer, the 1970s saw great strides in computational simulation techniques, enabling realistic pilot training on the ground, as the automatic flight control system

Figure 2.2: Bell X-1 aircraft during its first flight on January 19, 1946. [8]

on board of the training aircraft allowed the dynamic behaviour of an entirely different aircraft to be simulated, such as the space shuttle Gulfstream-II. [28]

The F-16 aircraft was designed for "relaxed static stability" and all-electric (full "fly-by-wire") control, in sequence of flight control technology advances in the 1970s. Preceding this, a "high-authority" electrical control superimposed on the basic electro-hydraulic system had been implemented, for example, on the F-111, and an electrical system with mechanical backup on the Concorde. Although, electrical signals processing for these automatic flight control systems was still analog. Flight tests with digital flight control systems and with additional aerodynamic control surfaces, for providing direct-lift control or direct side-force control, were only done in the 1980s, raising interesting multivariable control problems for modern control theory. [28]

Modern aircraft evolution established a need for automatic pilot control systems and power-driven aerodynamic control surfaces, and, from the 1990s on, raised several new challenges for flight control systems. Further advances in control technology, estimation techniques, and system modelling have provided better analytical tools with which to design multivariable control laws, making room for unconventional techniques to emerge — such as propulsion control.

Flight/Propulsion control coupling (FPCC) started emerging as a technique for enhancing aircraft performance and the growing demand for this technique triggered concentrated research efforts [31;32;33;34;35;36] aimed at advancing the state-of-the-art of this technology.

Rock et al. introduced a technique for generating specifications that define how subsystems must perform within an integrated control system in order to assure performance goals are met when the integrated system is implemented [37]. In this paper, the authors claimed that a specification generation procedure such as the one presented will be required to make integrated flight/propulsion control design practical, after applying those procedures to a simple flight/propulsion control system.

Back in 1990, NASA developed the Performance Seeking Control (PSC) Algorithm [38] — an adaptive, integrated flight/propulsion control algorithm, targeting total aircraft performance optimisation during steady state engine operation. The system's architecture had four primary components: a Rolm Hawk computer, a Digital Flight Control Computer (DFCC), Digital Electronic Engine Controls (DEEC) and Electronic Air Inlet Controllers (EAIC). The Hawk computer, where the majority of the algorithm's logic is located, contains all control law modules (propulsion system, engine update logic, optimisation routine and supervisory logic). This computer, along with the DFCC, calculates the optimum trim commands, that are further applied to the EAIC, that adjusts the cowl and third ramp positions on the inlet's geometry, and DEEC, that adjusts

the engine operating point and the afterburner operation. Extensive nonlinear aircraft/engine, high fidelity simulations identified significant increases in thrust (up to 15%), and reductions in specific fuel consumption (up to 3%), resulting from the algorithm's implementation. [38]

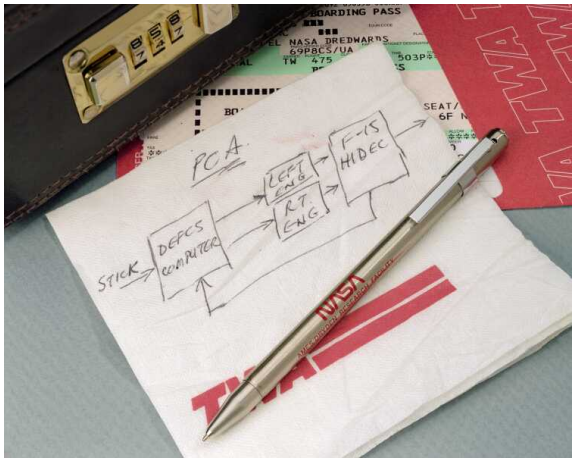


Figure 2.3: Frank W. Burcham's napkin sketch for the PCA system. [4]

In 1994, the Propulsion Controlled Aircraft (PCA) [39] concept idea came to the engineer Frank W. Burcham while travelling with NASA Dryden F-15 project manager James Stewart, leading him to roughly sketching it on a Napkin, Figure 2.3. This was an emergency backup system to be used if major primary flight controls failed, maneuvering the aircraft to a safe landing without moving the normal control surfaces, as several of this system failures had been experienced in recent flights. Longitudinal and lateral-directional control laws were developed for such scenarios, commanding the flightpath angle and augmenting phugoid damping and using differential throttle inputs to generate yaw and resultant roll motion by dihedral effect (Figure 2.5. During the testing phase, the longitudinal control system performed well but, because of wind gusts, the lateral-directional response was considered too sluggish near the ground, so some improvements and control law changes had to be made in the algorithm before flight implementation. [39] This research was a partnership between NASA and McDonnell Douglas Aerospace, St. Louis, MO, with Pratt & Whitney together with Honeywell, resulting on the first successful landing under engine-power only was achieved in August 29, 1995, by a McDonnell Douglas MD-11, in Figure 2.4.

Figure 2.4: First landing of a transportation aircraft using the PCA system. [5]

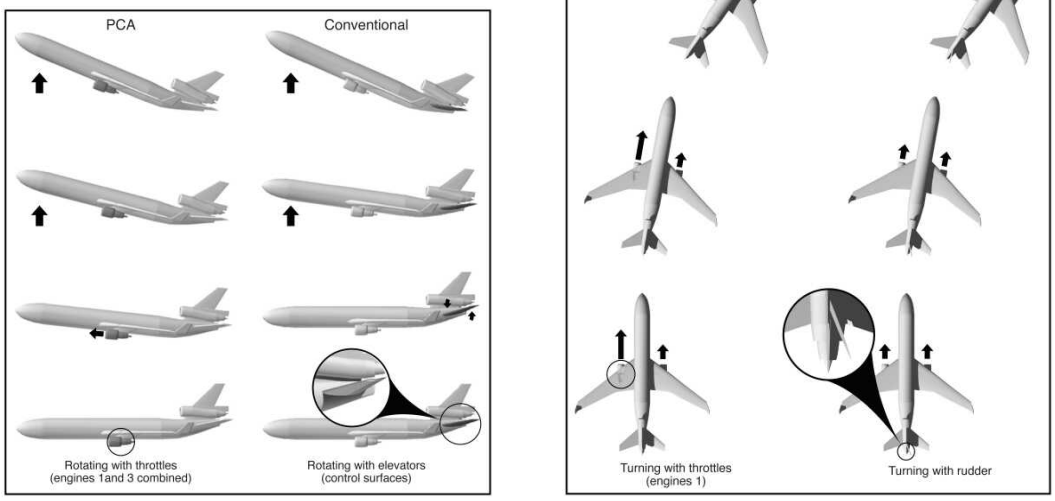


(a) Longitudinal motion (b) Lateral-directional motion

Figure 2.5: Propulsion Controlled Aircraft (PCA) concept. [5;7]

In 1996, Jonckheere et al. applied the $H_\infty$ methodology to the problem of matching the dynamically compensated throttle-actuated crippled aircraft model and the nominal control-surface-actuated aircraft model [40]. The outcome was that the responses of the crippled aircraft were almost the same as of the nominal model, demonstrating that $H_\infty$ design copes with the model matching problem in a satisfactory way. As that research only covered the longitudinal motion, in the following year, Jonckheere et al. introduced a neural network approach to gain-scheduling linear dynamic controllers for the lateral motion of PCA [41]. A demonstration of the concept through a simulation of an L-1011, confirmed the design's effectiveness for the chosen flight conditions and the family of controllers. Further research [42], allowed for an understanding that, contrary to the more popular model matching by plant state feedback, error feedback is an easier, more robust design against uncertainties. This outcome was achieved after two strategies comparison, th error feedback for longitudinal control and the crippled aircraft state feedback for lateral control.

Two new versions of PCA were presented by NASA later in 1998 — the Lite and Ultralite flight modes. Although a full implementation of this system has still not happened, these were cheaper and more adaptable versions that did not require changes in the aircraft's engine-control computer, in an attempt to make them more attractive to industry. PCA-Lite allows the pilot to use an aircraft's existing auto-throttle and engine trim commands to perform engines-only landings. Results showed that PCA-Lite is almost as effective as the full system, although it can only be implemented in aircrafts with digital engine controls. PCA-Ultralite also uses an airplane's existing auto-throttles to control pitch (climb and descent), but unlike PCA and PCA-Lite, does not require digital engine controllers. Instead, the pilot needs to manually control the throttle of each engine for directional motion control. [43] Subsequent studies into PCA further demonstrated the concept [44;45;46;47;48].

Ochi et al. designed [49] a flight control system for propulsion controlled aircraft (PCA) in 1999, which are controlled using thrust only. In this study, specifically the fases of approach and landing were considered (most critical) based on the state-space approach and employing the

$H_\infty$ state-feedback control. To make the design simpler and the gain adjustment easier, the control and guidance loops were designed at a time, instead of the conventional separated loops. The designed flight control systems (glide slope, fare and lateral-directional controls) achieved satisfactory approach and landing using the available amount of thrust (assuming that the trim thrust is 50% of the maximum cruise thrust at the flight condition), although the study didn't take into account the uncertainties of the aircraft model.

In 2000, Yu proposed a novel design algorithm for the pitch control[50] of PCA over a flight envelope for a crippled airplane. The linear controllers are synthesised at various equilibrium operating points by an $H_\infty$ method to solve the model matching problem(when the crippled airplane matches the responses of the nominal model). The radial basis networks (RBN) trained from the family of $H_\infty$ controllers is used for gain scheduling and yields controllers that provide acceptable performance over an operating range, therefore constructing the gain scheduling controller. RBN usage eliminates the difficulty of multivariable control scheduling and while maintaining the desired performance.

Concerning modern commercial airliners for emergency procedures, another study was conducted by NASA in 2004[24], still motivated by the increasing history of accidents and incidents in which some or all flight controls were lost. In these accidents, many pilots attempted to control the aircraft with throttles-only, using differential thrust to control bank angle (generating sideslip and achieving a roll motion through the aircraft's dihedral effect) and collective thrust to control flightpath, but this control method often proved unsuccessful for landing. As so, NASA studied the Manual Manipulation of Engine Throttles (TOC) for a wide range of aircraft through simulation and flight. Although, all tested aircraft showed sufficient control capability, being able to maintain most of the control effectiveness, with both flightpath and ground track angle being controlled to within a few degrees, manual TOC usage was concluded to be excessively difficult to use for safe runway landings, due to the oscillatory dutch roll and phugoid modes combined with weak control moment generation and slow engine response. [24]

Later in 2005, Ochi[51] complemented his previous study[49] by designing a controller for descent and deceleration for longitudinal motion and using a model-following control method, based on a linear quadratic regulator. The authors simulated the deceleration, descent, approach and landing and came to the conclusion that both longitudinal and lateral-directional control are successfully achieved, although speed control proves more difficult. However, if the horizontal stabiliser ain't damaged, the airspeed can be reduced to a safer landing speed.

Hitachi et al. presented in 2009 a robust PCA control system for vertical-tail-damaged aircraft by using $H_\infty$ loop transfer recovery ($H_\infty$-LTR) technique[52], and testing it both for linear and nonlinear simulations of a four-engine jet aircraft. The authors proved the system's control effectiveness under different levels of vertical tail damage, therefore validating this method as a solution to enhance the robustness of an optimal controller.

As past research had demonstrated that the engines' slow response as control actuators, when compared to conventional control surfaces, was one of the major contributors to the difficulty in landing with PCA, further research[53] was conducted in 2009, attempting to make the engine more responsive during emergency conditions. NASA carried out an example sensitivity analysis on the C-MAPSS engine, with the objective of investigating its ability to respond faster than usual, and enable an overthrust capability. This investigation concluded that engine controllers can be redesigned and/or the limits adjusted, to reach a quicker response and/or operate under overthrust conditions in emergency scenarios. However, this enhanced operation severely decreases the engine's life and increases its operability risk. [53]

Engine response time requirements in severe vertical stabiliser damage situations were exam-

ined by NASA in 2010[54]. The time constant and delay requirements for enabling the usage of aircraft engines as control effectors instead of the rudder were computed through that study, in 2010. It was observed that, as the dutch-roll damping and engine thrust decreases when the altitude increases, the engine response time needs to be quicker for high altitude and high speed operations, as engines have less thrust capability — making flight-propulsion control more effective at low airspeed and altitude. The initial conditions can interfere in the stability of the propulsion control due to engine thrust saturation, as when the engine thrust enters its limiting values, its control effectiveness is lower. Also, the yaw and roll rates' limits may be relatively small for higher airspeed and altitude, so in case the initial conditions on those rates exceed these limits, the aircraft will depart.[54] The objective of this research was that its results could be be taken into account during future aircraft design phase.

In 2012, engineer James M. Urnes reviewed the Propulsion Controlled Aircraft (PCA) flight mode concept for Multi-engine UAV Aircraft[55]. This study showed that introducing this feature not only increases control redundancy as well as decreases the need for multiple control channels, but also that the use of PCA for roll control can permit lighter wing structural weight and tailless configurations using thrust changes for directional control.

Posteriorly, Lu et al. proposed a strategy in 2015 based on differential thrust to be used as a control input to act as a "virtual" rudder and help maintain stability and control of a damaged aircraft[56]. This strategy had a $H_\infty$ loop-shaping approach in order to achieve a stable and robust flight envelope. That robust control system design's ability o stabilise the damaged aircraft was successful, as it reached steady state stability within only 15 seconds under feasible control efforts.

More recently, the authors designed a linear quadratic regulator controller[57], to study the ability of the damaged aircraft to track and mimic the behaviour of the model aircraft (reference) in an extreme scenario. An ability that the authors demonstrated through an adaptive control system design based on the Lyapunov stability approach-based model reference adaptive control methodology. Robustness and uncertainty analysis showed that uncertain plant dynamics were able to follow model plant dynamics with asymptotic stability, in the presence of 30% full block, additive uncertainty, associated with damaged aircraft dynamics, therefore achieving safe (and stable) operating conditions.

The potential of integrating propulsion controlled systems as a primary mode of aircraft control is still an ongoing research endeavour, due to the continuing trade-off between advantages and challenges associated with the implementation of this technology.

## 2.2 Advantages and Challenges

As seen in Section 2.1, propulsion control researches were mainly motivated by this concept's advantages in emergency situations where conventional flight controls were lost. However, besides safety reasons, other advantages of this control method can be identified.

Aircraft with this technology benefit from inferior acquisition and maintenance costs, due to the much simpler flight control systems. A boosted engine life and fuel efficiency are other perks. As a result of the needed engine control modes, that allow the engine to always function within its optimum operating conditions. Optimal engine control also results in less fuel burn and extended component life, provoking operating costs reduction as well.

Lighter airframe structural weight is achievable, once part of the roll and yaw moments are controlled through thrust, the wing and tail structures are allowed less rigidness and the control

surfaces require less surface area. These reductions could as well lead to aircraft wing and tail design advances, for weight optimisation.
Possible augmentation of the aircraft's flight envelope, considering the propulsion's superior effectiveness at extreme angles of attack and sideslip, when compared to the rudder and ailerons.
An increase in the control redundancy, since propulsion control augments the aircraft's conventional control and decreases the number of control channels needed.
In addition, a satisfactory performance of these systems as a control means has been proven, after many flight tests having demonstrated good enough flight path control and aircraft stabilisation.
Although there are many advantages in controlling an aircraft through its propulsive system, there're also a few challenges regarding this implementation.
A relevant issue is concerning the total quantity of engines and the respective possible lack of excess thrust available for control in some phases of the flight, for example during take-off. In addition, there's a reduction of effectiveness at high airspeed and altitude, as the engines have less thrust capability.
Engine thrust variations ought to be fast enough so that sufficient lateral-directional dynamic aircraft stability is achieved. The engine's slower actuating power in comparison to the conventional flight control surfaces is one of the main concerns regarding propulsion control efficient usage. Also, as with increased altitude the engine's thrust decreases, its response requirements are more demanding for high altitude and speed operation.
Due to the previously presented response requirement, the phugoid and dutch-roll modes control and the dangers associated with exceeding the aircraft's flight envelope limits, manual engine control is inefficient, requiring extensive practise and concentration, thus optimum engine control modes are recommended to achieve that demand.

## 2.3 Distributed Electric Propulsion

Electric propulsion could be implemented to overcome the formerly mentioned challenges, namely the need for faster response engines and additional thrust capability. Further benefits come from the implementation of a Distributed Electric Propulsion (DEP) system, as engines can be placed, sized, and operated with large flexibility, allowing to explore the aero-propulsive coupling benefits and to improve the performance of conventional designs, including reducing the traditional control surfaces and decreasing the aircraft's control system vulnerability to engine-out cases. [58] In fact, the emergence of the DEP system concept potentiates new capabilities for future aircraft's design, efficiency and robustness. Although a formal definition is yet to be established, DEP can be designated as a means for providing (by way of an electric transmission system) the necessary energy to power an array of multiple-small-independently-powered propulsive units located across the aircraft that empower the improvement of the system.
This benefit of adopting distributed propulsion to enable aircraft control was introduced by Winborn [59], Ko et al. [60], Kim and Saunders [61], and Kim et al. [62]. [58]
These works provided insight into the use of DP as a control method for aircraft flight dynamics and its role on the more traditional control surfaces potential elimination, opening new doors for vertical tail surface reduction or even elimination and aircraft weight.
Leifsson et al. [63] utilised the same approaches as the previously mentioned studies, but implementing it in a blended wing body aircraft design concept. In this BWB research the DP control

was provided by thrust vectoring, replacing the usual elevon surfaces, and the total wing weight reduction was demonstrated.

Later, considering the increased number of engines in a DEP configuration, the advantage of increased control redundancy was indicated by Ko et al.[60], emphasising on the less critical aircraft performance consequences in an engine-out scenario. In such a scenario, for a DEP aircraft, a re-arrangement of the system's total thrust is possible by re-allocating the lost engine's thrust.

Nguyen et al.[64] explored the use of DEP as a way for controlling and improving aircraft aerodynamics, by means of propulsion-induced aeroelastic responses leveraging. The authors presented an aeroelastic wing shaping control concept for DEP aircraft, proving that DP can be used to increase aerodynamic efficiency.

A great benefit of the DEP technology integration is the enhanced dynamic pressure over the wing at reduced speeds due to the propellers being distributed along the wingspan, enabling wing area reduction and high-speed cruise efficiency without jeopardising the low-speed performance.[65] Also, designing the high-lift propellers for low-speed operation instead of propulsive efficiency at cruise, avoids the oversizing of the wings for takeoff and landing sake (oversized wings have a much higher velocity during cruise then when the airframe lift-to-drag ratio is maximised).

An additional advantageous characteristic is the possibility of lowering the community noise during the take-off and landing flight phases, by increasing the effective bypass ratio (*ratio of mass flow rate of all combined air flow entering the DEP fans over that entering the engine core*[58])through increasing the number of electrically-driven fans. Besides noise reduction, a substantially lower acoustic impact is likewise verified on electric engines comparing to turbines and its components.[66]

Another favourable reason for the study of this alternative propulsion system is the visible strong impact of aviation on the environment. Besides the emissions and pollution problem, there is the fact that the amount of petroleum fuel is limited, even if it is not clear when that resource will drain.[67] As electric propulsion systems benefit from better energy conversion efficiency and can be considered zero-emission, they are attractive in that extent.

Although the environmental stand of electric vehicles can be controversial as far as the battery manufacturing impacts on greenhouse gas emissions are concerned, last year (2018) the International Council on Clean Transportation (ICCT) issued a report[68] on the subject. This council came to the conclusion that an electric engine is much cleaner than an internal combustion engine over their lifetime and that the battery manufacturing life-cycle emissions debt is quickly paid off after only 2 years.

The majority of electric motors can be overloaded for a short period of time without overheating and damaging the insulation. The continuous electric current can be exceeded beyond normal values if the motor has been running with reduced current for some time. The primary factors influencing the duration and magnitude of that admissible overload are the previous pattern of operation and the thermal time-constant. Thermal time constants dictate the temperature's rate of rise and may extent from a few seconds for small motors to many minutes to hours for large ones.[69]

As all electric motors follow the electromagnetism laws and are therefore under the same constrains imposed by the materials from which they are made, common proprieties between them can be identified:[69]

1. Rated torque is roughly proportional to the rotor, and consequently motor, volumes in motors with identical cooling systems.

2. Any given motor's admissible output is mainly constrained by its cooling arrangement.
3. Output specific power is proportional to speed.
4. The efficiency of a motor increases along with speed.
5. Small motors have a lower specific torque and are less efficient than large ones.
6. Any motor can be modified to match any voltage.

Undoubtedly, the motors, generators and electrical cables govern the electrical system's weight, dictating cautious deliberation for engine placement, cooling system's efficiency and number of motors and generators. Thus, it is preferable to avoid an excessive amount of motors and generators, as well as placing them far, requiring cable drawing across the fuselage.[70] For compensating the many electrical units and components' weight, composite materials may be a good solution. Although, if those materials were applied other difficulties such as the impacts on the airframe in a lightning strikes event, and the system's data network protection would need to be revised.

Electric engines convert electrical into mechanical energy, granting scale-free integration freedom (efficiency, compactness, high power to weight and reliability at any scale) and without experiencing a power lapse as altitude increases. With a great number of available concepts, distinct in energy conversion and storage (energy per mass and per volume) always under constant improvement, the most relevant energy storage approaches are the battery, fuel cell, solar cell, beamed energy, flywheels and generator based systems.

Even though the battery based concept may be the most popular one, some obstacles to its implementation can be identified such as temperature sensitivity, insulation and cooling requirements, fire hazard, system cost, handling issues and the total system environmental issues from mining the exotic metals to production and eventual disposal.[21]

Also, if battery systems were to be implemented on a regular basis, plans for airport infrastructure and investment concerning battery recharging and replacement would be required and certification rules and safety levels would need adaptation. One example is the matter of engine failure probability (Equation 2.1), which states that the probability of an engine failure increases linearly with the number of engines. Based on this, an aircraft with 10 propulsors would be 5 times more likely to suffer an in-flight shutdown (IFSD) of one of them than a twin-engine. Although this is indeed true, the advantage of having the power distributed along 10 engines is that this loss would only represent 10% of the total thrust versus a 50% thrust loss in the twin, making the probability of critical propulsion system failure reduce increasingly with the number of engines. The probability of $m$ engine(s) failure on an aircraft with $\bar{N}$ engines is given by[71]

$$\binom{\bar{N}}{m} \cdot p_{ef}^{m} = \frac{\bar{N}!}{m!(\bar{N}-m)!} \cdot p_{ef}^{m} \tag{2.1}$$

Electric propulsion's penalties can be summed to the energy storage's weight and cost and the certification and safety aspects. Due to the the typical flown distances and needed flight autonomy and as a result of the current state-of-the-art of energy density, energy storage is a core problem for electric propulsion application in aircraft.[67] Thus, broad advances in the energy storage and conversion fields are continuously being researched in order to grant the use of electrically-driven propulsors' increased efficiency and feasibility.[58]

Looking at the data provided in Table 2.1, it is easy to see that significant improvements still need to be made in order for battery-electric aircraft to become truly competitive with fuel-based aircraft.

Table 2.1: Battery Specific Energy and Density. [21]

| | Chemistry | Typical Values (Wh/kg) | (Wh/L) | Name |
|---|---|---|---|---|
| old | Lead-acid | 45 | 100 | Lead acid |
| | Alkaline | 100 | 300 | Alkaline |
| Nickel | NiFe | 25 | 30 | Nickel Iron |
| | NiCd | 60 | 150 | Nickel Cadmium |
| | NiH | 75 | 60 | Nickel Hydrogen |
| | NiMH | 90 | 300 | Nickel Metal Hydride |
| | NiZn | 100 | 280 | Nickel Zinc |
| Li-ion | Li-ion | 100-265 | 250-700 | Lithium ion |
| | Li-ion Polymer | 100-265 | 250-730 | Lithium Polymer |
| | LiCoO2 | 200 | — | Lithium Cobalt Oxide |
| | LiFePO4 | 120 | 170 | Lithium Iron Phosphate |
| | LiMn2O4 | 150 | — | Lithium Manganese Oxide |
| | LiNiMnCoO2 | 260 | 500 | Lithium Nickel Manganese Cobalt Oxide (NMC) |
| | LiS | 400 | 250 | Lithium Sulfur |
| | LiS (2020) | 500 | 1000 | Licerion$^2$ (LiS) |
| | Li titanate | 90 | 170 | Lithium Titanate |
| | Li-air | 500 | 200 | Lithium-Air |
| misc | Na-ion | 150 | 50 | Sodium Ion |
| | Molten salt | 220 | 290 | Molten Salt |
| | Silver Zinc | 200 | 700 | Silver Zinc |
| Comparisons | Wood | 4500 | 3600 | Wood |
| | Coal | 8000 | 10000 | Coal |
| | Jet Fuel | 11000 | 10000 | Jet Fuel |
| | Gasoline | 12000 | 9000 | Gasoline |
| | LH2 | 39406 | 2790 | Liquid Hydrogen |
| | Uranium | 2.2E+10 | 4.3E+11 | Uranium |
| | Antimatter $c^2$ | 9.0E+10 | | Antimatter |

Despite the limited currently-available specific energy density, there are already a number of electric aircraft concepts throughout the world, the majority of which being small aircraft applications. This is due to the prevailing drawback of the weight to power ratio, as to the exorbitantly hight weights of the currently available energy storage options, which constantly drive researchers to limit their electric power implementation studies to unmanned, low speed aircraft with high aspect ratios wings. [70]

### 2.3.1 Reference Projects and Actors

One of the initial Distributed Electric Propulsion concepts was the Turboelectric Distributed Propulsion (TeDP). Initially proposed by NASA [72] but since then researched by other industries, this concept basically consists of several highly-efficient and light-weight electric motors that run distributed electric fans, whose electric power is provided by independent generators driven by one or several gas turbines. The TeDP approach for power transmission allows for each electric generator to spin at any given speed, thus the propulsors can be operated at separate optimum speeds. Also, the speed ratio may change during flight, behaving like a variable-ratio gearbox, with the use of power inverters between the fan motors and the generators. Another characteristic of this technology is that a high degree of flexibility can be achieved by the use of electrical power transmission when the fan module and turboelectric generators are positioned to take advantage of the synergistic propulsive-airframe integration.

Figure 2.6: NASA N3-X aircraft concept. [8;9]

Configurations for future commercial aviation, such as the NASA N3-X[72;73;74] (Figure 2.6), the NASA Single-Aisle Turboelectric Commercial Transport with fuselage boundary layer ingestion (Figure 2.7) and the Empirical Systems Aerospace ECO-150 (Figure 2.8), employ this propulsion concept.

Figure 2.7: NASA Single-Aisle Turboelectric Commercial Transport (STARC-ABL) concept. [10;11]

Figure 2.8: ESAero's ECO-150 concept. [11]

Besides the TeDP propulsion system, more DEP propulsion systems are being proposed, researched and developed for a number of different aircraft configurations and applications. Several of them have been successfully flown and demonstrated, amongst which a 20% scale demonstrator of the Aurora XV-24 LightningStrike UAV (Figure 2.9), the Lilium jet (Figure 2.10) and the NASA GL-10 Greased Lightning UAV (Figure 2.11). Although the GL-10's developed dynamic model has been published[75], the dynamic models and controllers for the XV-24 LightningStrike UAV and Lilium jet have not been made public, nor have the respective used methods.


Figure 2.9: Aurora Flight Sciences XV-24 LightningStrike UAV concept. [12]

(a) London Landing Platform

(b) The jet

Figure 2.10: Lilium jet concept. [13;14]

In the Aurora Flight Sciences XV-24 LightningStrike UAV, a tilting-wing with 18 distributed ducted fans plus two forward canards with 3 more ducted fans each are powered by a Rolls-Royce AE1107C turboshaft engine, which generates electric power through 3 Honeywell generators. This experimental vertical takeoff and landing (VTOL) configuration with high cruise speed, was canceled in April 2018.

The Lilium jet, advertised as *"An air taxi to revolutionise the way we travel"*[76], is a five-seater VTOL fully-electric concept aiming to travel up to 300km in only one hour. The wings carry 36 tilt electric jet engines that face up for vertical take-off and landing and shift forward for horizontal flight. It is meant to serve as an "air-taxi" launched in multiple cities by 2025.

NASA's GL-10 Greased Lightning UAV has 8 electric-drive engines placed on its 3 meter wingspan tilting-wing plus 2 placed on its tilting-horizontal-stabiliser. Those propellers are placed on the leading edge, providing high speed flow and consequently increasing lift, reducing the necessary wing and stabilator surface area. It was designed to endure a loiter mission of up to 24 hours and complete multiple vertical take-offs and landings.

Figure 2.11: NASA GL-10 Greased Lightning UAV concept. [15]

Besides the three previously mentioned, there are a number of other VTOL DEP aircraft configurations for the new and emerging “air-taxi” market that aims to reduce urban traffic congestion as well as providing an “on-demand” air service[77]. Examples are the Joby Aviation S2 (Figure 2.12) and the Airbus Vahana (Figure 2.13).

Figure 2.12: Joby Aviation S2 concept. [16]

Figure 2.13: Airbus Vahana concept. [17]

A worth mentioning DEP conventional fixed-wing configuration is the NASA’s X-57 Maxwell [78; 65; 55], inspiration to this work. Employing 14 electrically-driven and battery-powered leading edge asssynchronous propeller technology (LEAPTech), 2 large ones at the wing-tips and 12 small mounted at the wing’s leading-edge, this X-plane is a modification of the baseline Italian Tecnam P2006T, by replacing its wing and propulsive system.

Figure 2.14: NASA X-57 Maxwell concept. [18; 19]

Although a number of DEP-based control configurations have been suggested, there has not been sufficient published work contributing toward the theoretical development of DEP dynamic models to enable flight controllers that take advantage of the technology.

## 2.4 Lateral-directional motion control

From the previously cited literature in this Section, it's possible to identify multiple potential ways of controlling the aircraft's lateral-directional motion.
In order to control the yaw motion, one possibility consists in producing lateral air pressure as far behind the cg as possible, pushing the tail in that force's direction and generating a turning of the aircraft around the vertical axis — this is the aerodynamic principle behind the rudder's actuation as a primary control surface.
Another possibility is generating differential drag between the two wings, accelerating the wing with less drag and generating a turning of the aircraft around the vertical axis through sideslip — this is the principle behind the differential/asymmetric thrust concept (Figure 2.15) for directional motion control, advancing the throttle(s) on one wing and retarding the other(s), lightly increasing the drag on the retarded throttle(s)' wing.
Vectored thrust (Figure 2.15) is also an option for this motion's control, although it's not an existing capacity in the majority of aircraft's current configuration, having to be installed. This concept allows a lateral thrust component to be added by changing the engine's heading vector, in order to turn the aircraft around its vertical axis.

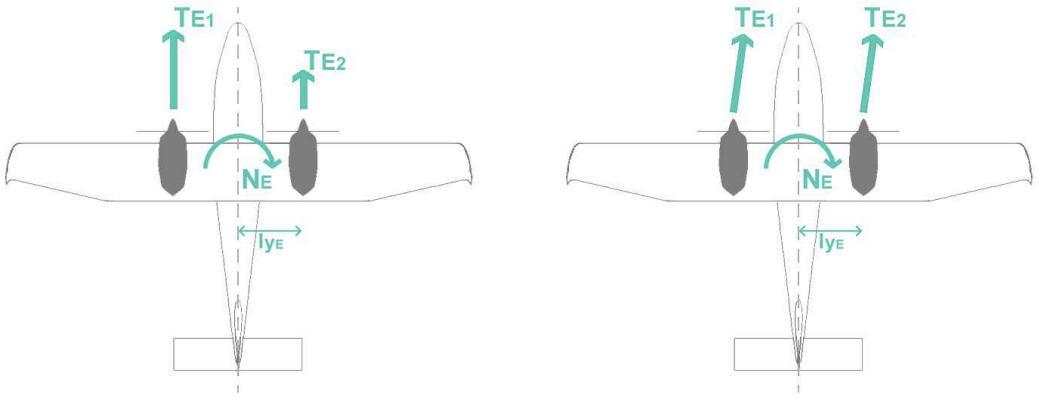


(a) Differential thrust (b) Vectored thrust

Figure 2.15: Considered propulsion control methods.

As for the roll motion, one possibility consists in producing positive-vertical air pressure on one wing tip and negative on the other, pushing each wing in the respective applied force's direction and generating a turning of the aircraft around the longitudinal axis — this is the aerodynamic principle behind the ailerons' actuation as primary control surfaces.
Although, there's a coupled roll motion in the differential thrust concept previously referred (as sideslip generates roll rate), an improved lateral motion can be achieved with this method by reducing thrust on the inboard-wing's engines or increasing thrust on the wingtip's engines. Good roll maneuverability is achieved if the aerodynamic roll moment is large and if the angular moment of inertia is small (in order to avoid interactions with pitch motion, bank angles must be kept small). As such, engine-induced roll motion could be achieved by independent thrust vectored engines.
For simplicity purposes, this work adopts the differential thrust concept for the whole lateral-directional motion dynamic, and other concepts were not explored.

# Chapter 3

## Model parameters formulation and computation

In order to fully understand the validity of this work's propulsion controller, two study cases will be compared — one is an aircraft with conventional control and the other is a modification of the same aircraft for enabling distributed propulsion control.
The selection of these case studies was inspired by the NASA X-57 Maxwell experiments [78;65;65], where the Italian conventional four-seater light aircraft — Tecnam P2006T was modified as shown in Figure 3.1, by replacing its twin-engines with distributed electric propulsion and installing an higher aspect ratio wing, in order to demonstrate technology to reduce emissions, noise and fuel consumption. The first case study will be the Tecnam P2006T aircraft and the second an optimised DEP transformation of this aircraft. This optimisation covers the selection of the engines' number and vertical empennage sizing.

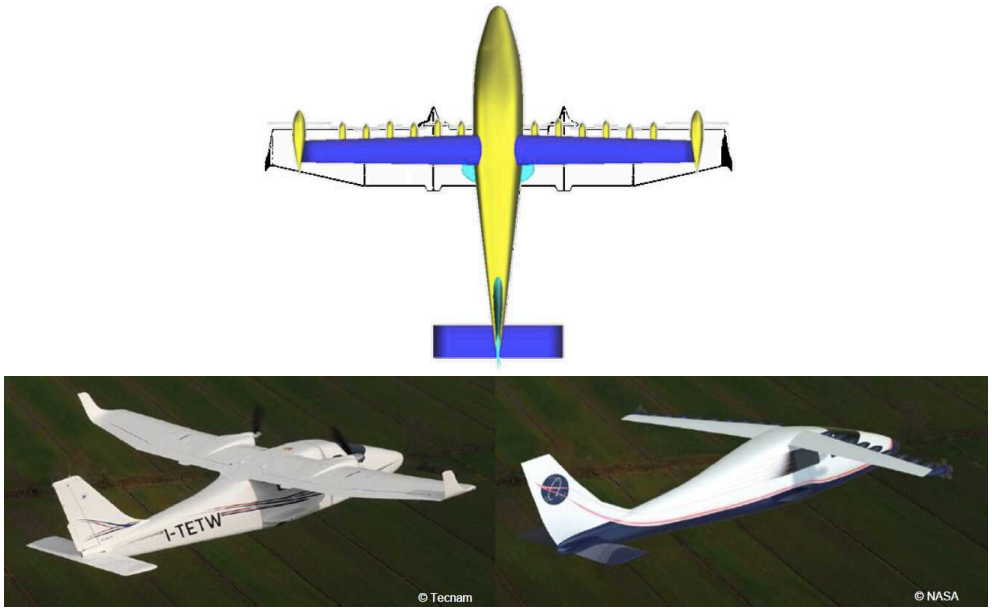


Figure 3.1: Tecnam P2006T (on the left) and NASA X-57 Maxwell (on the right) comparison. [19]

The validity of the dynamic model parameters can have an impact on the controller performance, making their correct estimation and validation relevant. As so, their model parameters were obtained from Tecnam P2006T's documentation [20;79] for Case I and through a brief and elementary analytic data estimation based on conceptual design methods for Case II, considering the modification's impacts on weight, inertia moments and products, drag, take-off performance and control and stability derivatives. A comparison between different engine arrangements was also made, in order to estimate the best DEP configuration.
In order to evaluate the limitations of the methods used to estimate these parameters, a calibration was made by also applying the method to the Tecnam P2006T and comparing the results with the aircraft's known values from publications [20]. Both cases' model parameters are presented in this chapter and will be used for the design of the control system. The International System of Units (SI) was adopted in this work's calculations, unless specifically stated otherwise.

## 3.1 Case I — Tecnam P2006T

### 3.1.1 Model parameters

Tecnam P2006T data was collected from the aircraft's type-certificate [79] and the work of Vecchia, P., Nicolosi, F. and De Marco, A. [20].
The parameters presented here will be used for the design of the control system and simulations of the following chapters. From Table 3.1 to Table 3.5 geometrical, mass, propulsion, performance and aerodynamic data of this aircraft can be found. The horizontal empennage of this airplane is a stabilator, i.e. an 'all moving tail' whose deflection is represented in this work as $\delta_e$. Aileron and rudder deflections are represented here as $\delta_a$ and $\delta_r$, respectively. In Figure 3.2, the three-view drawing of P2006T aircraft is shown.

Table 3.1: Tecnam P2006T Aircraft Geometric Characteristics.

| Geometrical Characteristics | | | |
|---|---|---|---|
| Wing span | $b_w$ | 11.4 | $m$ |
| Wing area | $S_w$ | 14.8 | $m^2$ |
| Wing mean-chord | $c_w$ | 1.3 | $m$ |
| Vertical tail span | $b_v$ | 1.6 | $m$ |
| Vertical tail area | $S_v$ | 1.60 | $m^2$ |
| Vertical tail mean-chord | $c_v$ | 1.06 | $m$ |
| Fuselage length | $l_{fus}$ | 8.7 | $m$ |
| Fuselage height | $h_{fus}$ | 2.85 | $m$ |

Table 3.2: Tecnam P2006T Aircraft Mass Characteristics.

| Mass Characteristics | | | |
|---|---|---|---|
| Maximum Take-off Weight | $W_{TO}$ | 1180 | $kg$ |
| Standard Equipped Weight | $W_{empty}$ | 760 | $kg$ |
| Standard Useful Load | $W_{useful}$ | 420 | $kg$ |
| Maximum Load Factor | $n_{max}$ | $+3.8$ | $g$ |
| Minimum Load Factor | $n_{min}$ | $-1.9$ | $g$ |
| $X_{cg}$ Maximum Forward | $X_{cg_f}$ | 16.5 | $\%MAC$ |
| $X_{cg}$ Maximum Aft | $X_{cg_a}$ | 31 | $\%MAC$ |
| Rolling mass Moment of Inertia | $Ixx$ | 1617 | $kg\ m^2$ |
| Pitching mass Moment of Inertia | $Iyy$ | 1927 | $kg\ m^2$ |
| Yawing mass Moment of Inertia | $Izz$ | 2931 | $kg\ m^2$ |
| Roll-Yaw Product of Inertia Ixy | $Ixy$ | 0 | $kg\ m^2$ |
| Yaw-Pitch Product of Inertia Iyz | $Iyz$ | 0 | $kg\ m^2$ |
| Pitch-Roll Product of Inertia Izx | $Izx$ | 0 | $kg\ m^2$ |

Table 3.3: Tecnam P2006T Aircraft Propulsion Characteristics.

| Propulsion Characteristics | | | |
|---|---|---|---|
| Engine Model | | | Rotax 912S |
| Propeller (2 Blades, Constant Speed Full Feathering) | | | MTV-21-A-C-F/CF178-05 |
| Maximum Power | $P_{max}$ | 73 | $kW$ |
| Propeller disk area | $A_{prop}$ | 2.50 | $m^2$ |
| Engine axial distance to cg | $l_{x_T}$ | 0.14 | $m$ |
| Engine side distance to cg | $l_{y_T}$ | 1.58 | $m$ |
| Engine incidence angle | $\varepsilon_{T_e}$ | 0 | $deg$ |

Table 3.4: Tecnam P2006T Aircraft Performance Characteristics.

| Performance Characteristics | | | |
|---|---|---|---|
| Maximum Speed at Sea Level | $V_{max}$ | 80 | $m/s$ |
| Cruise Speed (75%, 2740 m) | $V_{75\%,2740}$ | 75 | $m/s$ |
| Cruise speed (65%, 2100 m) | $V_{65\%,2100}$ | 70 | $m/s$ |
| Stall Speed Flap Down | $V_S$ | 24 | $m/s$ |
| Maneuvering Speed | $V_A$ | 60 | $m/s$ |
| Never Exceed Speed | $V_{NE}$ | 86 | $m/s$ |
| Climb Rate, S.L. | $_{climb}$ | 6.4 | $m/s$ |
| Climb rate, S.L., One Engine Inoperative (OEI) | $_{climb,se}$ | 1.5 | $m/s$ |
| Service Ceiling (Twin Engine) | $h_{max}$ | 4570 | $m$ |
| Single-Engine Ceiling (OEI) | $h_{se}$ | 2100 | $m$ |
| Take-off Distance | $S_{TO}$ | 361 | $m$ |
| Take-off Run | $S_G + S_R$ | 251 | $m$ |
| Landing Distance | $S_L$ | 257 | $m$ |
| Landing Run | $S_{LR}$ | 203 | $m$ |

Table 3.5: Tecnam P2006T Aircraft Aerodynamic Characteristics.

| Aerodynamic Characteristics | | | |
|---|---|---|---|
| Zero-lift drag derivative | $C_{D_0}$ | 0.0334 | $(per\ radian)$ |
| Drag due to angle of attack derivative | $C_{D_\alpha}$ | 0.222 | $(per\ radian)$ |
| Zero angle of attack lift derivative | $C_{L_0}$ | 0.289 | $(per\ radian)$ |
| Lift due to angle of attack derivative | $C_{L_\alpha}$ | 4.152 | $(per\ radian)$ |
| Pitching moment at zero angle of attack | $C_{m_0}$ | $-0.922$ | $(per\ radian)$ |
| Pitching moment due to angle of attack derivative | $C_{m_\alpha}$ | $-0.871$ | $(per\ radian)$ |
| Pitching moment due to pitch rate derivative | $C_{m_q}$ | $-14.799$ | $(per\ radian)$ |
| Pitching moment due to stabilator deflection derivative | $C_{m_{\delta_e}}$ | $-1.811$ | $(per\ radian)$ |
| Side force due to sideslip derivative | $C_{Y_\beta}$ | $-0.355$ | $(per\ radian)$ |
| Side force due to roll rate derivative | $C_{Y_p}$ | 0.254 | $(per\ radian)$ |
| Side force due to yaw rate derivative | $C_{Y_r}$ | 0.112 | $(per\ radian)$ |
| Side force due to aileron deflection derivative | $C_{Y_{\delta_a}}$ | 0.127 | $(per\ radian)$ |
| Side force due to rudder deflection derivative | $C_{Y_{\delta_r}}$ | $-0.040$ | $(per\ radian)$ |
| Yawing moment due to sideslip derivative | $C_{n_\beta}$ | 0.0135 | $(per\ radian)$ |
| Yawing moment due to roll rate derivative | $C_{n_p}$ | $-0.130$ | $(per\ radian)$ |
| Yawing moment due to yaw rate derivative | $C_{n_r}$ | $-0.106$ | $(per\ radian)$ |
| Yawing moment due to aileron deflection derivative | $C_{n_{\delta_a}}$ | $-0.009$ | $(per\ radian)$ |
| Yawing moment due to rudder deflection derivative | $C_{n_{\delta_r}}$ | $-0.0304$ | $(per\ radian)$ |
| Rolling moment due to sideslip derivative | $C_{l_\beta}$ | $-0.029$ | $(per\ radian)$ |
| Rolling moment due to roll rate derivative | $C_{l_p}$ | $-0.281$ | $(per\ radian)$ |
| Rolling moment due to yaw rate derivative | $C_{l_r}$ | 0.057 | $(per\ radian)$ |
| Rolling moment due to aileron deflection derivative | $C_{l_{\delta_a}}$ | $-0.045$ | $(per\ radian)$ |
| Rolling moment due to rudder deflection derivative | $C_{l_{\delta_r}}$ | 0.0009 | $(per\ radian)$ |

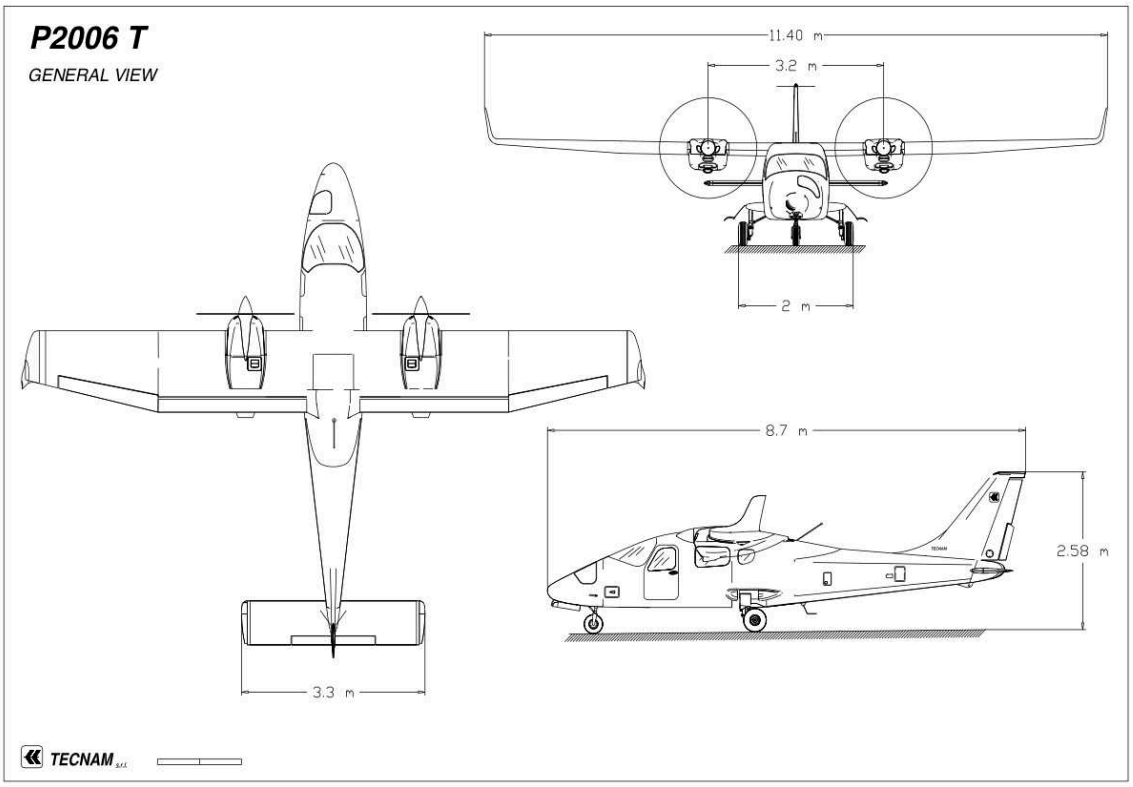


Figure 3.2: Three view drawing of P2006T Aircraft. [20]

## 3.2 Case II — DEP configuration

This case study is an optimised DEP transformation of the Tecnam P2006T aircraft. This optimisation covers the selection and integration of DEP engines on the wing and sizing of the vertical empennage accordingly. A comparison between different engine arrangements was also made, in order to estimate this study's best DEP configuration.
Published work [80] on NASA X-57 Maxwell flight demonstrator's high-lift propeller system configuration selection was consulted and the respective information was used to select the different propulsive arrangements this study will consider for case study number two, that are:

1. Ten high-lift propellers
2. Twelve high-lift propellers
3. Fourteen high-lift propellers
4. Sixteen high-lift propellers

The propellers considered are identical and equidistant along the wing, for each configuration. The size and characteristics of each propeller corresponds to the upper sized high-lift propeller on the aforementioned NASA work, since no cruise propellers will be considered for the wingtips, the wing has space for bigger and more powerful engines to be installed along the span (i.e. the 10 high-lift propellers configuration in this work possess the 8 high-lift propellers' characteristics on NASA's work).
The design advantages and impacts of the DEP implementation will be studied according to each of the four possible configurations and further compared.

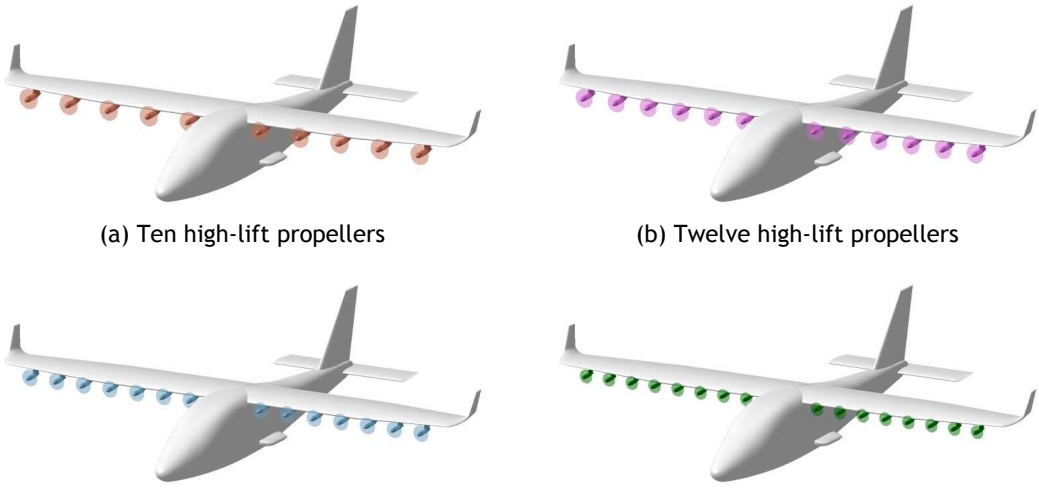

(a) Ten high-lift propellers

(b) Twelve high-lift propellers

(c) Fourteen high-lift propellers

(d) Sixteen high-lift propellers

Figure 3.3: Representation of the four different propulsive arrangements considered in this study for Case II, before the vertical empennage sizing.

### 3.2.1 Vertical empennage sizing

As previously seen in Chapter 2.3, one of the benefits of installing DEP technology is the possibility of vertical empennage reduction, allowing a weight and drag decrease.

The certification compliance of a distributed electric propulsion aircraft using differential thrust is still under discussion and there are different possible approaches on the matter. In this work, for the vertical tail sizing optimisation, Part 25 regulations[31] were followed by complying with control and stability requirements (illustrated in Figure 3.4), with the exception of §25.147(b)(1): *"The two critical engines must be inoperative with their propellers in the minimum drag position"*.

If such an optimisation were to be implemented it is not certain such regulation would be the most appropriate, as certification specifications dictate requirements based on traditional aircraft, and as so are not well-adapted to DEP aircraft. Thus, since the probability of losing specifically the two critical engines in the presented configurations is roughly as likely as losing all engines on a twin-engine, §25.147(a)(1): *"one critical engine"* was considered. Alternatives have been studied and debated in previous works[32], where new definitions and parameters are proposed as foundation to establish compliance with high level certification aims.

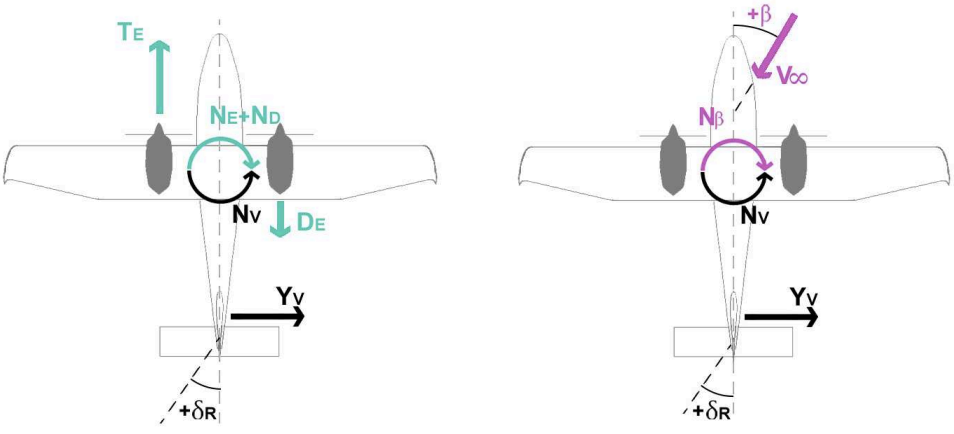


Figure 3.4: Schematics of the asymmetric power and crosswind sizing conditions, respectively.

#### 3.2.1.1 Control requirement

As stated in the certification regulations[81], the sizing of the vertical tail according to the controllability requirements is done for the engine failure during take-off case, which originates an asymmetric power condition. In this condition, the active engine symmetrically positioned to the failed engine causes an adverse yaw moment $N_E$.

$$N_E = T_E \cdot y_E \tag{3.1}$$

where,
$T_E$ is the take-off thrust of each engine.
$y_E$ is the distance perpendicular to the longitudinal axis between the vehicle center of gravity and the active engine.

The failed engine produces additional drag ($D_E$), increasing the moment around the vertical axis. For a variable pitch propeller aircraft, that moment can be estimated as

$$N_D = 0.25 \cdot N_E \tag{3.2}$$

To counteract this adverse yaw, the moment generated by the vertical tail has to be

$$N_V = N_E + N_D \tag{3.3}$$

That moment can be obtained from[83]

$$N_V = Y_V \cdot l_v = \Delta C_{Y,rudder} \cdot \frac{S_{v_f}}{S_v} \cdot K_\Lambda \cdot \bar{Q} \cdot S_v \cdot l_v \tag{3.4}$$

where,
$Y_V$ is the side force produced by the rudder deflection.
$\frac{S_{v_f}}{S_v}$ is the ratio of the rudder-affected vertical tail area to the total vertical tail area.
$K_\Lambda$ is an empirically derived correction factor that accounts for the effects of vertical tail planform.
$Q$ is the dynamic pressure, with

$$\bar{Q} = \frac{1}{2} \cdot \rho \cdot {V_{MCG}}^2 \tag{3.5}$$

where,
$\rho$ is the atmospheric density.
$V_{MCG}$ is the minimum control speed on ground.
$\Delta C_{Y,rudder}$ is the increment in airfoil subsection maximum side-force coefficient due to the rudder deflection, obtained from

$$\Delta C_{Y,rudder} = \delta_r \cdot \left[ \frac{c_{l_{\delta_r}}}{(c_{l_{\delta_r}})_{theory}} \right] \cdot (c_{l_{\delta_r}})_{theory} \cdot K' \tag{3.6}$$

where,
$(c_{l_{\delta_r}})_{theory}$ is the theoretical rudder side-force effectiveness.
$\frac{c_{l_{\delta_r}}}{(c_{l_{\delta_r}})_{theory}}$ is an empirical correction factor.
$K'$ is an empirical correction factor for nonlinear effects at high rudder deflections.

In summary, the minimum required vertical empennage area can be estimated by

$$S_v = \frac{N_E + N_D}{\delta_r \cdot \left[\frac{c_{l_{\delta_r}}}{(c_{l_{\delta_r}})_{theory}}\right] \cdot (c_{l_{\delta_r}})_{theory} \cdot K' \cdot \frac{S_{vf}}{S_v} \cdot K_\Lambda \cdot \frac{1}{2} \cdot \rho \cdot {V_{MCG}}^2 \cdot l_v} \tag{3.7}$$

#### 3.2.1.2 Stability requirement

The dimensioning flight case for the stability requirement [31] is at crosswind conditions. In such conditions, the rudder is used to correct the drift, so the vertical empennage must be sized to provide sufficient control authority in order to maintain a steady-sideslip. Thus, the moment generated by the vertical tail should counteract the sideslip angle ($\beta$), so that

$$N_V = N_\beta \tag{3.8}$$

and,

$$N_\beta = C_{n_\beta} \cdot \beta \cdot \bar{Q} \cdot S_w \cdot b_w \tag{3.9}$$

Expressed in coefficient form by dividing through by $(\beta \cdot \bar{Q} \cdot S_w \cdot b_w)$, the yawing moment due to sideslip of a wing-body-tail configuration, referred to it's center of gravity and based on the wing area and wing span, is given by [33]

$$C_{n_\beta} = (C_{n_\beta})_{WB} + \sum_v \left[ -(\Delta C_{Y_\beta})_v \cdot \frac{l_v}{b_w} \right] \tag{3.10}$$

As the subscript *v* refers to panels present in the vertical empennage, this expression can be simplified to

$$C_{n_\beta} = (C_{n_\beta})_{WB} - (\Delta C_{Y_\beta})_v \cdot \frac{l_v}{b_w} \tag{3.11}$$

where
$l_v$ is the distance parallel to the longitudinal axis between the vehicle centre of gravity and the quarter-chord point of the MAC of the vertical empennage, positive for the empennage aft of the gravity centre.
$b_w$ is the span of the wing.
$(C_{n_\beta})_{WB}$ is the contribution of the wing-body combination to the total yawing moment due to sideslip, obtained from [33]

$$(C_{n_\beta})_{WB} = -\frac{180}{\pi} \cdot K_N \cdot K_{R_l} \cdot \frac{S_{B_S}}{S_w} \cdot \frac{l_B}{b_w} \qquad (per\ radian) \tag{3.12}$$

where,
$K_N$ is an empirical factor related to the sideslip derivative for body plus wing-body interference.
$K_{R_l}$ is an empirical Reynolds-number factor.
$S_{B_S}$ is the projected side area of the body.
$l_B$ is the length of the body.

$(\Delta C_{Y_\beta})_v$ is the side force due to sideslip of the vertical empennage, obtained from [33]

$$(\Delta C_{Y_\beta})_v = -k \cdot (C_{L_\alpha})_v \cdot \left(1 + \frac{\partial \sigma}{\partial \beta}\right) \cdot \frac{q_v}{q_\infty} \cdot \frac{S_v}{S_w} \tag{3.13}$$

where,

$k$ is an empirical factor.

$(C_{L_\alpha})_v$ is the lift-curve slope of the vertical panel, determined with the effective aspect ratio of the vertical empennage.

$\left(1 + \frac{\partial \sigma}{\partial \beta}\right) \cdot \frac{q_v}{q_\infty}$ is a parameter representing the wake and side-wash effects.

$\frac{S_v}{S_w}$ is the ratio of the vertical empennage area (measured to the body centre-line) to the total wing area.

In summary, the minimum required vertical empennage area can be estimated by solving the following equation in order to $S_v$

$$\frac{-\frac{180}{\pi} \cdot K_N \cdot K_{R_l} \cdot \frac{S_{B_S}}{S_w} \cdot \frac{l_B}{b_w} + k \cdot (C_{L_\alpha})_v \cdot \left(1 + \frac{\partial \sigma}{\partial \beta}\right) \cdot \frac{q_v}{q_\infty} \cdot \frac{S_v}{S_w} \cdot \frac{l_v}{b_w} \cdot \frac{1}{2} \cdot \rho \cdot {V_{MCG}}^2 \cdot S_w \cdot b_w \cdot \beta}{\delta_r \cdot \left[\frac{c_{l_{\delta_r}}}{(c_{l_{\delta_r}})_{theory}}\right] \cdot (c_{l_{\delta_r}})_{theory} \cdot K' \cdot \frac{S_{v_f}}{S_v} \cdot K_\Lambda \cdot \frac{1}{2} \cdot \rho \cdot {V_{MCG}}^2 \cdot S_v \cdot l_v} = 1 \tag{3.14}$$

#### 3.2.1.3 Methodology implementation and calibration

Both requirements of control and stability must be met. The methodology used was to follow the set of equations described in Chapter 3.2.1.1, obtain the minimum required vertical empennage area for controllability estimation from Equation 3.7, follow the set of equations described in Chapter 3.2.1.2 and obtain the minimum required vertical empennage area for stability estimation from Equation 3.14. The equation that gives the higher area estimate corresponds to the dimensioning requirement, if Equation 3.7 results on a higher value than Equation 3.14, then the control requirement is the dimensioning requirement and the resultant estimated area is the minimum area the vertical empennage must have (and vice-versa).

In order to evaluate the limitations of the methods used to estimate the control and stability vertical empennage requirements, a calibration was made by also applying the previously used method to the Tecnam P2006T and comparing the results with the aircraft's known values from publications [20].

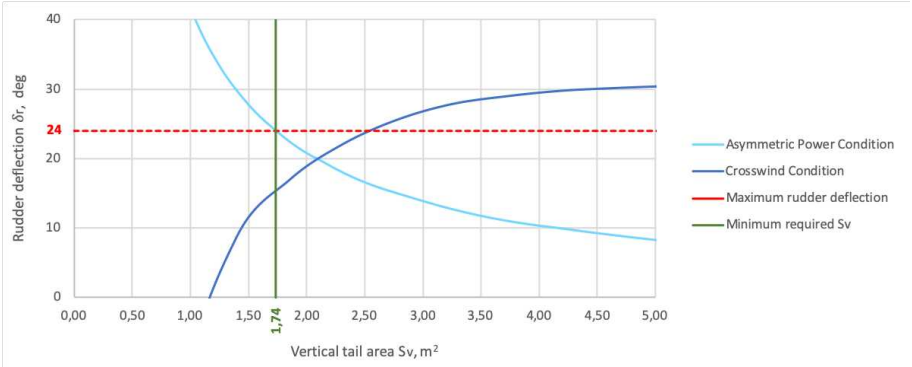


Figure 3.5: Graphical representation of P2006T's vertical empennage sizing according to requirements.

Results from Figure 3.5 allow a validation of the used methodology, as it can be observed that the real values are close to the ones obtained analytically, by a conservative error of around 8% (which is within the expected error of this methodology). This percent error was incorporated as a calibration to the method to bring the sizing results of the optimised configurations closer to their real values (results on Figure 3.6) and Table 3.6, following Equation 3.15.

$$S_{v\ (real\ value)} = 92\% \cdot S_{v\ (methodology)} \tag{3.15}$$

Implementing this calibration, it is possible to predict the percentage of allowable vertical empennage reduction on the optimised configurations, comparing to Tecnam's vertical empennage real size ($1.60m^2$).

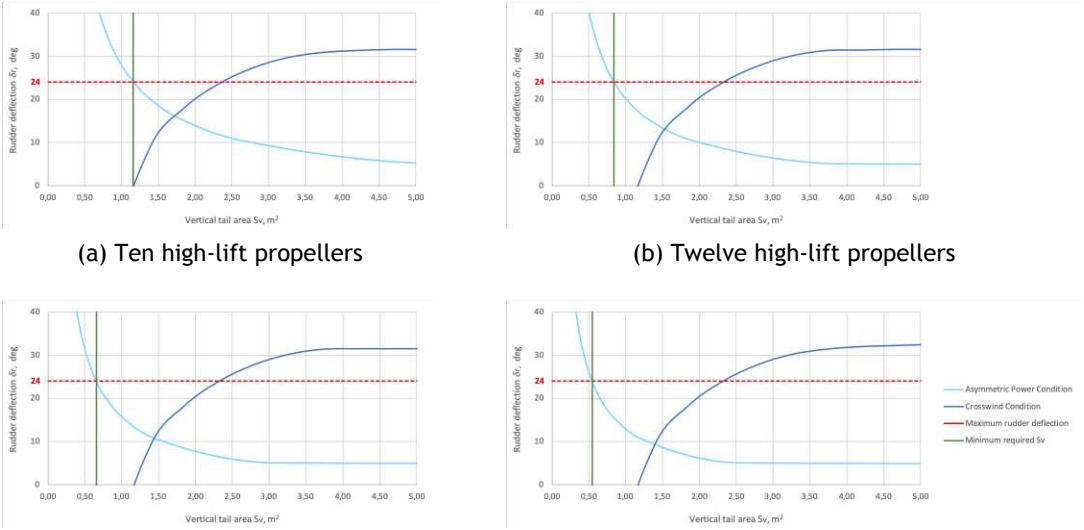


(a) Ten high-lift propellers

(b) Twelve high-lift propellers

(c) Fourteen high-lift propellers

(d) Sixteen high-lift propellers

Figure 3.6: Graphical representation of the optimised configurations' vertical empennage sizing according to requirements.

Table 3.6: Vertical empennage's sizing results calibration.

| | methodology sizing $m^2$ | real value (calibration) $m^2$ | area reduction % |
|---|---|---|---|
| Tecnam P2006T | 1.74 | 1.60 | – |
| Ten high-lift propellers | 1.16 | 1.07 | 33 |
| Twelve high-lift propellers | 0.83 | 0.77 | 52 |
| Fourteen high-lift propellers | 0.65 | 0.60 | 62 |
| Sixteen high-lift propellers | 0.54 | 0.50 | 69 |

It is due noticing that the vertical empennage area reduction results presented on Table 3.6 are for the worst possible case, covering only the current certification requirements and disregarding the potentials of the DEP technology implementation. With distributed propulsion as a form of aircraft control, the rudder deflection-envelope will most likely diminish, granting more room for a sub-sequential empennage reduction. In Figure 3.7 the CAD representations of these configurations was developed using CATIA v5[1] and OpenVSP[2]. For simplicity matters during calculations, the distance parallel to the longitudinal axis between the vertical tail's aerodynamic center and the nose of the aircraft was maintained, as well as the aspect ratio and sweep angle.

[1] CATIA v5, Dassault Systèmes S.A.

[2] OpenVSP, NASA gov

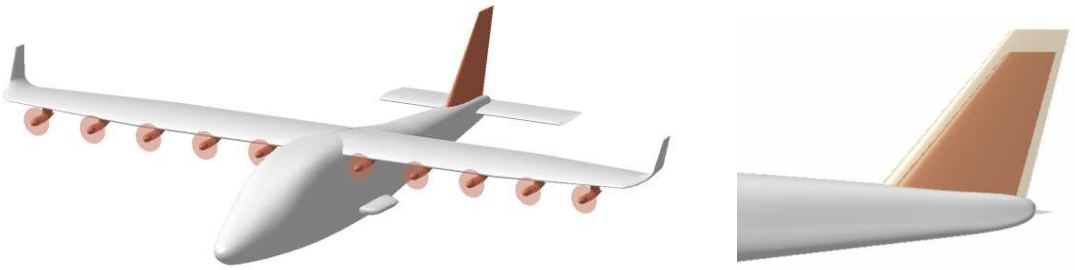

(a) Ten high-lift propellers

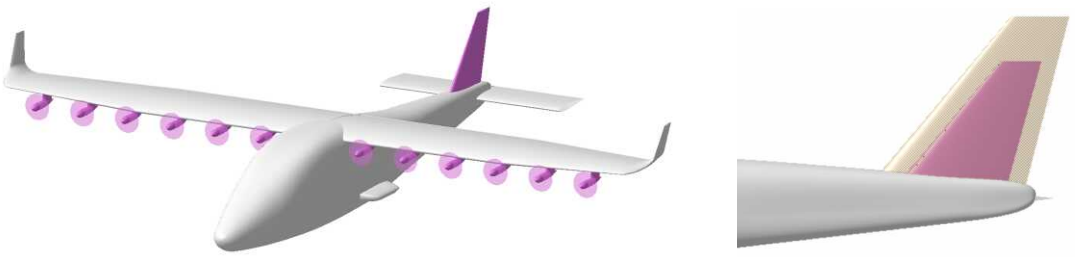

(b) Twelve high-lift propellers

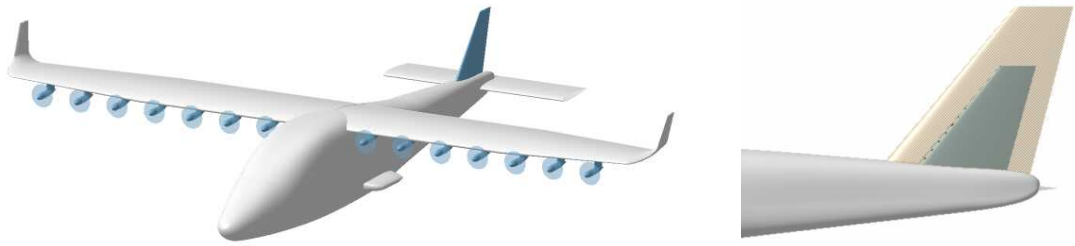

(c) Fourteen high-lift propellers

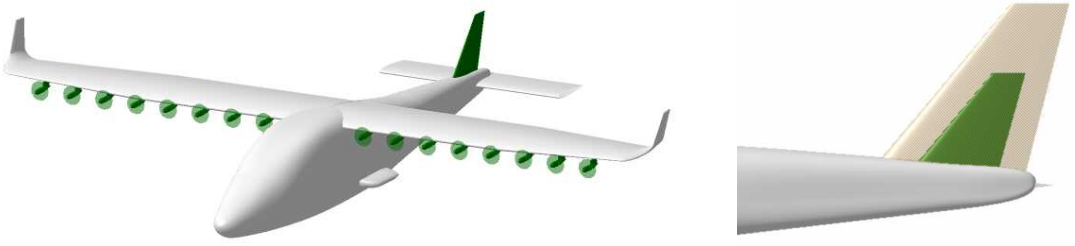

(d) Sixteen high-lift propellers

Figure 3.7: Representation of the four different propulsive arrangements considered in this study for Case II, after the vertical empennage sizing.

### 3.2.2 Impacts on aircraft design

With the proposed modifications to the vertical tail and propulsion system, some of the original aircraft's characteristics such as weight, inertia moments and products, drag and performance were altered. The impacts of such modifications were roughly estimated using mainly Roskam [34;35;36] methods.

#### 3.2.2.1 Weight

Besides the nacelles and vertical tail weight estimates, the wing and horizontal tail weight were also calculated for application in the inertial calibration. The weight variation of the engines was estimated according to published data [80] and the remaining elements followed a Class II method for estimating structural weight of general aviation airplanes [85], such as the Tecnam P2006T.
According to the Cessna Method [85], for multi-engine aircraft with horizontally opposed engines, the total nacelle weight is given by

$$W_n = 0.24 \cdot P_{TO} \tag{3.16}$$

where,
$P_{TO}$ is the total take-off power.

It is assumed that the weight for an electric engine's nacelle also obeys this formula. The battery weight associated with the proposed propulsion system installation is not considered in this work's analysis, although NASA's X-57 references [78] suggest an energetic density of around $500\ Wh/kg$. Given an energetic consumption of $10.5\ kW/h$ per engine [78], one could estimate around $20\ kg$ of battery weight per engine per hour of operation. Considering Tecnam P2006T's flight autonomy of $4.5\ hours$, this would represent roughly a $95\ kg$ battery weight per engine for obtaining the same autonomy.
The same Method [85] states that the vertical tail weight can be obtained from

$$W_v = \frac{1.68 \cdot {W_{TO}}^{0.567} \cdot {S_v}^{1.249} \cdot {A_v}^{0.482}}{639.95 \cdot {t_{r_v}}^{0.747} \cdot {cos\Lambda_{1/4_v}}^{0.882}} \tag{3.17}$$

and the horizontal tail from

$$W_h = \frac{3.184 \cdot {W_{TO}}^{0.887} \cdot {S_h}^{0.101} \cdot {A_h}^{0.138}}{174.04 \cdot {t_{r_h}}^{0.223}} \tag{3.18}$$

where,
$W_{TO}$ is the take-off weight.
$S_{v,h}$ is the vertical and horizontal tail area, respectively.
$A_{v,h}$ is the vertical and horizontal aspect ratio, respectively.
$t_{rv,h}$ is the vertical and horizontal maximum root thickness, respectively.
$\Lambda_{1/4_v}$ is the vertical tail quarter chord sweep angle.

For cantilever wings, the Method [85] gives the weight from

$$W_w = 0.04674 \cdot {W_{TO}}^{0.397} \cdot {S_w}^{0.360} \cdot {n_{ult}}^{0.397} \cdot {A_w}^{1.712} \tag{3.19}$$

where,
$A_w$ is the wing aspect ratio.
$n_{ult}$ is the design ultimate load factor.

As only the take-off weight of the Tecnam P2006T is known [79] and the Cessna Method depends on that parameter, this methodology was calibrated iteratively with that aircraft in order to obtain the new configuration's take-off weight by subtracting the variation of the engines, nacelles and

vertical tail weight, relative to the Tecnam P2006T, so that

$$W_{TO_i} = W_{TO_{(Tecnam)}} - \Delta W_{ei} - \Delta W_{ni} - \Delta W_{vi} \tag{3.20}$$

with,

$$\Delta W_{ei} = W_{e_{(Tecnam)}} - W_{e_{(methodology)_i}} \tag{3.21}$$

$$\Delta W_{ni} = W_{n_{(Tecnam)}} - W_{n_{(methodology)_i}} \tag{3.22}$$

$$\Delta W_{vi} = W_{v_{(Tecnam)}} - W_{v_{(methodology)_i}} \tag{3.23}$$

Where the *i* index represents each one of the new configurations.
Each optimised configuration's equipped/empty weight is therefore given by

$$W_{empty_i} = W_{TO_i} - W_{useful} \tag{3.24}$$

The Cessna-method weight estimation data can be found on Table 3.7. It is due noticing that the Tecnam's maximum take-off and empty weights are the aircraft's corresponding real known weights, not estimates.

Table 3.7: Cessna-method weight estimation.

| | | Tecnam P2006T | High-lift propellers | | | |
|---|---|---|---|---|---|---|
| | | | Ten | Twelve | Fourteen | Sixteen |
| Weight ($kg$) | Engines ($W_e$) | 113.4 | 48.19 | 41.91 | 39.42 | 39.4 |
| | Nacelles ($W_n$) | 21.77 | 23.13 | 20.12 | 18.92 | 18.91 |
| | Vertical tail ($W_v$) | 23.60 | 17.43 | 12.98 | 10.42 | 8.82 |
| | Horizontal tail ($W_h$) | 42.23 | 42.23 | 42.23 | 42.23 | 42.23 |
| | Wing ($W_w$) | 176.97 | 176.97 | 176.97 | 176.97 | 176.97 |
| | Maximum take-off ($W_{TO}$) | 1080 | 1110 | 1096 | 1090 | 1088 |
| | Empty ($W_{empty}$) | 760 | 690 | 676 | 670 | 668 |

#### 3.2.2.2 Inertia

Moments of inertia allow the understanding of how rotational motion changes when the mass distribution changes, characterising the resistance of a body to those changes. As the proposed configurations imply weight changes, each aircraft component's center of mass is no longer the same, therefore the moments of inertia need to be estimated for those new configurations.
The procedure employed was to consider that the aircraft is divided into six main components: the vertical and horizontal tails, the wing, the propulsive system (nacelles plus engines and propellers), the landing gear and the fuselage. Where the fuselage here is assumed to include all components not acknowledged before as main, such as power-plant and fixed equipment, so that its weight equals the known aircraft total weight minus the estimated weight of the other main components.
After that, and except for the fuselage component, the mass center of each main component was predicted using the developed CAD models, assuming constant densities for each one and distinguishing between the right and left sides of the aircraft.

Considering a class II method for estimating moments and products of inertia, the following applies [85]

$$I_{xx} = \sum_i m_i \cdot [(y_i - y_{cg})^2 + (z_i - z_{cg})^2] \tag{3.25}$$

$$I_{yy} = \sum_i m_i \cdot [(z_i - z_{cg})^2 + (x_i - x_{cg})^2] \tag{3.26}$$

$$I_{zz} = \sum_i m_i \cdot [(x_i - x_{cg})^2 + (y_i - y_{cg})^2] \tag{3.27}$$

$$I_{xy} = \sum_i m_i \cdot (x_i - x_{cg}) \cdot (y_i - y_{cg}) \tag{3.28}$$

$$I_{yz} = \sum_i m_i \cdot (y_i - y_{cg}) \cdot (z_i - z_{cg}) \tag{3.29}$$

$$I_{zx} = \sum_i m_i \cdot (z_i - z_{cg}) \cdot (x_i - x_{cg}) \tag{3.30}$$

Acknowledging that $I_{xy}$ and $I_{yz}$ are equal to zero, since all studied configurations are symmetrical.

The fuselage's centre of mass coordinates in the x and z axis were then iterated until the moments of inertia obtained from equations 3.25 to 3.27 approximately matched the ones from Tecnam P2006T data [20], and preserving the center of gravity travel envelope along the longitudinal axis [79]. The procedure is now calibrated and applicable to the new configurations, considering that the center of mass of the fuselage, wing, horizontal tail and landing-gear remains the same.

This methodology was first calibrated, by being applied to the Tecnam aircraft and verifying a conservative error of $4\%$ for the product of inertia $Izx$ and moments of inertia $Ixx$ and $Izz$ and a non conservative error of $5\%$ for the moment of inertia $Iyy$, the remaining products of inertia have no error. The corrected results for the high-lift configurations can be found on Table 3.8. It is due noticing that the Tecnam's moments of inertia are the aircraft's corresponding real known values, not estimates.

Table 3.8: Inertia estimation.

| | | Tecnam P2006T | High-lift propellers | | | |
|---|---|---|---|---|---|---|
| | | | Ten | Twelve | Fourteen | Sixteen |
| Moments of inertia ($kg\ m^2$) | $Ixx$ | 1617 | 1801 | 1723 | 1692 | 1691 |
| | $Iyy$ | 1927 | 1914 | 1809 | 1749 | 1713 |
| | $Izz$ | 2931 | 3176 | 3015 | 2934 | 2901 |
| Products of inertia ($kg\ m^2$) | $Ixy$ | 0 | 0 | 0 | 0 | 0 |
| | $Iyz$ | 0 | 0 | 0 | 0 | 0 |
| | $Izx$ | 234 | 212 | 194 | 184 | 178 |

#### 3.2.2.3 Drag

With the proposed modifications in the vertical tail and propulsion system, the original aircraft's drag was altered. To quantify these alterations a class II method for predicting the drag polar of subsonic airplanes during the preliminary design phase [86] was applied to the vertical tail and nacelles.
The subsonic vertical empennage drag coefficient is found from [86]

$$C_{D_v} = C_{D_{L_v}} + C_{D_{0_v}} \tag{3.31}$$

$C_{D_{L_v}}$ is the vertical empennage drag coefficient due to lift assumed to be zero, since vertical tails are normally installed symmetrically.
$C_{D_{0_v}}$ is the vertical empennage zero-lift drag coefficient, found by [86]

$$C_{D_{0_v}} = R_{wf} \cdot R_{LS} \cdot C_{f_v} \cdot \left[1 + L' \cdot \frac{t}{c} + 100 \cdot \left(\frac{t}{c}\right)^4\right] \cdot \frac{S_{wet_v}}{S_w} \tag{3.32}$$

where,
$R_{wf}$ is the wing/fuselage interference factor.
$R_{LS}$ is the lifting surface correction factor.
$C_{f_v}$ is the turbulent flat plate friction coefficient of the vertical empennage.
$L'$ is the airfoil thickness location parameter.
$\frac{t}{c}$ is the maximum thickness ratio associated wit the vertical empennage airfoil.
$S_{wet_v}$ is the wetted area of the vertical empennage.

The total nacelles drag coefficient may be computed from [86]

$$C_{D_n} = \sum_i (C_{D_n})_i \tag{3.33}$$

Where the index *i* equals the number of nacelles on the airplane. Each nacelle drag coefficient is computed with the following method [86]

$$(C_{D_n})_i = (C_{D_{L_n}})_i + (C_{D_{0_n}})_i \tag{3.34}$$

$(C_{D_{L_n}})_i$ is each nacelle drag coefficient due to lift, found by [86]

$$C_{D_{L_n}} = 2 \cdot {\alpha_n}^2 \cdot \frac{S_{b_n}}{S_w} + \eta \cdot c_{d_c} \cdot |\alpha_n|^3 \cdot \frac{S_{plf_n}}{S_w} \tag{3.35}$$

where,
$\alpha_n$ is the nacelle angle of attack.
$S_{b_n}$ is the nacelle base area.
$\eta$ is the ratio of the drag of a finite cylinder to the drag of an infinite cylinder.
$c_{d_c}$ is the experimental steady state cross-flow drag.
$S_{plf_n}$ is the nacelle planform area.

$(C_{D_{0_n}})_i$ is each nacelle zero-lift drag coefficient, found by [36]

$$C_{D_{0_n}} = R_{wf} \cdot C_{f_n} \cdot \left[1 + \frac{60}{(l_n/d_n)^3} + 0.0025 \cdot \frac{l_n}{d_n}\right] \cdot \frac{S_{wet_n}}{S_w} + C_{D_{b_n}} \tag{3.36}$$

where,
$R_{wf}$ is the wing/fuselage interference factor.
$C_{f_n}$ is the turbulent flat plate friction coefficient of the nacelle.
$l_n$ is the nacelle length.
$d_n$ is the maximum nacelle diameter.
$S_{wet_n}$ is the wetted area of the nacelle.
$C_{D_{b_n}}$ is the nacelle base-drag coefficient, given by [36]

$$C_{D_{b_n}} = \frac{0.029 \cdot (d_b/d_n)^3}{(C_{D_{0_{nb}}} \cdot S_w/S_n)^{1/2}} \cdot \frac{S_n}{S_w} \tag{3.37}$$

where,
$d_b$ is the nacelle base diameter.
$C_{D_{0_{nb}}}$ is the zero-lift drag coefficient of the base of the nacelle.
$S_n$ is the nacelle maximum frontal area.

As an estimate of the parasite drag coefficients of the Tecnam P2006T is known [20], this methodology was once again firstly calibrated with that aircraft before being implemented on the studied configurations. The new parasite drag coefficients were then obtained by subtracting the variation of the calculated vertical empennage and nacelles parasite drag coefficients, relative to Tecnam P2006T, so that

$$C_{D_{0\,i}} = C_{D_{0_{(Tecnam)}}} - \Delta C_{D_{0_v\,i}} - \Delta C_{D_{0_n\,i}} \tag{3.38}$$

with,

$$\Delta C_{D_{0_v\,i}} = C_{D_{0_{v_{(Tecnam)}}}} - C_{D_{0_{v_{(methodology)_i}}}} \tag{3.39}$$

$$\Delta C_{D_{0_n\,i}} = C_{D_{0_{n_{(Tecnam)}}}} - C_{D_{0_{n_{(methodology)_i}}}} \tag{3.40}$$

Here, the *i* index represents each one of the new high-lift configurations.

The Roskam-method parasite drag coefficient estimation data can be found on Table 3.9. It is due noticing that the Tecnam's total parasite drag coefficient is the aircraft's published [20] coefficient estimate.

Table 3.9: Parasite drag coefficient estimation.

| | | Tecnam P2006T | High-lift propellers | | | |
|---|---|---|---|---|---|---|
| | | | Ten | Twelve | Fourteen | Sixteen |
| Drag Coefficient | Vertical tail ($C_{D_{0_v}}$) | 0.00864 | 0.00840 | 0.00814 | 0.00792 | 0.00745 |
| | Nacelles ($C_{D_{0_n}}$) | 0.00543 | 0.00128 | 0.00147 | 0.00135 | 0.00149 |
| | Total ($C_{D_0}$) | 0.0334 | 0.02901 | 0.02895 | 0.02861 | 0.02828 |

#### 3.2.2.4 Take-off

Recalling the requirements from FAR Part 25 [31] that influence stability and control design, it is established that the minimum control speed requirements set in FAR §25.149 have a great influence in the sizing of an aircraft's vertical tail to controllability requirements. This speed is defined as "*the calibrated airspeed at which, when the critical engine is suddenly made inoperative, it is possible to maintain control of the airplane with that engine still inoperative and maintain straight flight with an angle of bank of not more than 5 degrees*" and must be established for the most critical case. That scenario is " *the calibrated airspeed during the takeoff run at which, when the critical engine is suddenly made inoperative, it is possible to maintain control of the airplane using the rudder control alone (without the use of nose-wheel steering), as limited by 150 pounds of force, and the lateral control to the extent of keeping the wings level to enable the takeoff to be safely continued using normal piloting skill*".

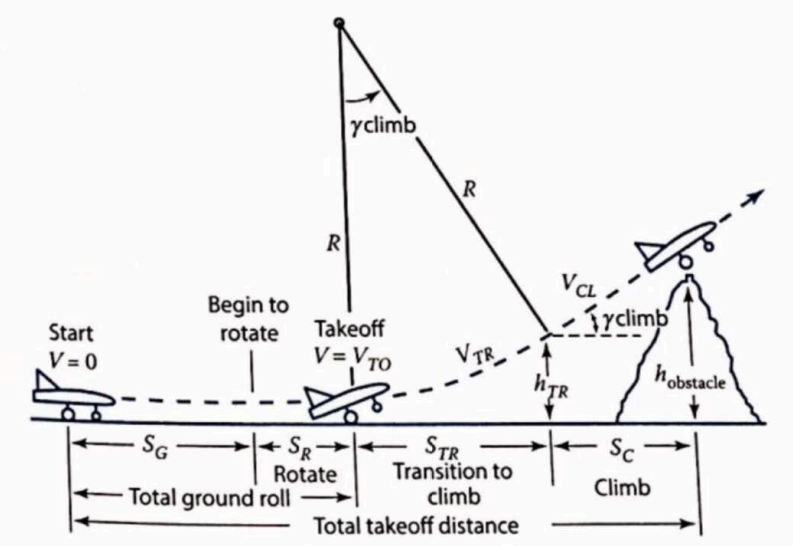


Figure 3.8: Take-off analysis. [21]

A simplified take-off analysis was implemented to insure no major disadvantageous modifications to the original aircraft's performance were made, such as a change in the minimum control speed or an increase on the total take-off field length. An empirical method [21] for determining those factors was implemented, assuming that the take-off takes place from a concrete or asphalt dry surface. As shown in Figure 3.8 ,the total take-off distance was segmented into total ground roll, which includes the level ground roll and the ground roll during rotation to the angle of attack for liftoff, the transition to climb and the climb phases.
Level ground roll can be determined by integrating velocity divided by acceleration, as follows

$$S_G = \int_{V_i}^{V_f} \frac{V}{a} dv \tag{3.41}$$

with,

$$a = g \cdot \left[ \left( \frac{T}{W} - \mu \right) + \frac{\rho}{2 \cdot W/S_w} \cdot (-C_{D_0} - K_{drag} \cdot C_L^2 + \mu \cdot C_L) \cdot V^2 \right] \tag{3.42}$$

For take-off, the initial velocity is zero, and the final velocity is $V_{TO}$, which was considered to

be 1.1 times the stall speed, found by setting maximum lift at stall speed equal to weight and solving for stall speed. Acknowledging that the thrust varies during the ground roll, an average thrust value of about 70% $(1/\sqrt{2})$ of $V_{TO}$ [21] was used.

Ground roll during rotation field length depends mostly on the pilot [21]. It was assumed that rotation takes 3 seconds and that the acceleration is negligible over that time interval, this makes the rotation ground roll distance equal to

$$S_R = 3 \cdot V_{TO} \tag{3.43}$$

During the transition to a stable climb phase, the aircraft's path was approximated to a circular arc where the average transition velocity is about $1.15\ V_{stall}$, as the aircraft accelerates from the take-off speed $1.10\ V_{stall}$ to the climb speed $1.20\ V_{stall}$. The radius of this transition arc can be calculated by [21]

$$R_{RT} = \frac{V_{TR}^2}{0.2 \cdot g} \tag{3.44}$$

The climb angle $\gamma$ at the end of this transition can be determined from

$$sin(\gamma_{climb}) = \frac{T - D}{W} \tag{3.45}$$

At this point of the take-off analysis, the obstacle height clearance needs to be calculated using Equation 3.46.

$$h_{TR} = R_{RT} \cdot (1 - cos(\gamma_{climb})) \tag{3.46}$$

If this height was cleared before the end of the transition segment, meaning $h_{TR} \geqslant h_{obstacle}$, the horizontal field distance traveled during transition is computed by Equation 3.47 and the total take-off distance is equal to the sum of these three distances: $S_G + S_R + S_{TR}$.

$$S_{TR} = \sqrt{R_{RT}^2 - (R_{RT} - h_{obstacle})^2} \tag{3.47}$$

If not and $h_{TR} \leqslant h_{obstacle}$, the transition horizontal field length is computed by Equation 3.48 and the horizontal distance travelled during the climb needs to be determined through Equation 3.49, so that the total take-off distance is equal to the sum of these four distances: $S_G + S_R + S_{TR} + S_C$.

$$S_{TR} = R_{RT} \cdot sin(\gamma_{climb}) \tag{3.48}$$

$$S_C = \frac{h_{obstacle} - h_{TR}}{tan(\gamma_{climb})} \tag{3.49}$$

Considering an obstacle height of $15\ m$, this methodology was first calibrated, by being applied to the Tecnam aircraft and verifying a conservative error of around $2\%$. The corrected take-off analysis data obtained with the described methodology for the high-lift configurations can be found on Table 3.10. It is due noticing that the Tecnam's take-off lengths data are the aircraft's published [87] estimates.

Table 3.10: Take-off field length estimation.

| | | Tecnam P2006T | High-lift propellers | | | |
|---|---|---|---|---|---|---|
| | | | Ten | Twelve | Fourteen | Sixteen |
| Field length ($m$) | Level ground roll ($S_G$) | 147 | 120 | 141 | 157 | 168 |
| | Rotation ground roll ($S_R$) | 104 | 25 | 25 | 25 | 25 |
| | Transition to climb ($S_{TR}$) | 85 | 93 | 75 | 66 | 61 |
| | Climb ($S_C$) | 24 | 11 | 32 | 47 | 56 |
| | Total take-off ($S_{TO}$) | 361 | 249 | 274 | 295 | 310 |

#### 3.2.2.5 Stability and control derivatives

The proposed reductions in the vertical tail changed the initial aircraft's aerodynamic angle-of-sideslip, roll rate, yaw rate and rudder control derivatives, namely

$$\{ C_{Y_\beta} , C_{n_\beta} , C_{l_\beta} , C_{Y_p} , C_{n_p} , C_{l_p} , C_{Y_r} , C_{n_r} , C_{l_r}, C_{Y_{\delta_r}}, C_{n_{\delta_r}}, C_{l_{\delta_r}} \} \tag{3.50}$$

The remaining aerodynamic derivatives were assumed to remain the same, for simplicity. The vertical tail contribution of mentioned stability derivatives for both study cases was calculated using preliminary design methods (found on Roskam [36] and presented below) and the resulting difference applied to the original derivatives [20], as follows

$$C_{(new)} = C_{(Tecnam)} - C_{(Tecnam)_V} + C_{(new)_V} \tag{3.51}$$

**Aerodynamic angle-of-sideslip derivatives**

The vertical tail contribution to the side force due to sideslip derivative $C_{Y_\beta}$ may be found from

$$C_{Y_{\beta_v}} = -k_v \cdot (C_{L_{a_v}}) \cdot (1 + d\sigma/d\beta) \cdot \eta_v \cdot \frac{S_v}{S_w} \tag{3.52}$$

where,
$k_v$ is an empirical factor.
$C_{L_{a_v}}$ is the vertical empennage lift curve slope.
$S_v$ is the effective vertical tail area.
and with $(1 + d\sigma/d\beta) \cdot \eta_v$ given by

$$(1 + d\sigma/d\beta) \cdot \eta_v = 0.724 + 3.06 \cdot \frac{S_v/S_w}{1 + cos(\Lambda_{c/4})} + 0.4 \cdot \frac{z_w}{z_f} + 0.009 \cdot A_w \tag{3.53}$$

where,
$\Lambda_{c/4}$ is the wing quarter chord sweep angle.
$A_w$ is the wing aspect ratio.
$z_w$ is the distance from wing root quarter chord point to the fuselage centreline (positive below fuselage centreline).
$z_f$ is the maximum fuselage depth.

The vertical tail contribution to the yawing moment due to sideslip derivative $C_{n_\beta}$ may be found from

$$C_{n_{\beta_v}} = -C_{Y_{\beta_v}} \cdot \frac{l_v \cdot cos(\alpha^*) + z_v \cdot sin(\alpha^*)}{b_w} \tag{3.54}$$

where,
$z_v$ is the vertical distance between the vertical tail's aerodynamic center and the aircraft's center of gravity.

The vertical tail contribution to the rolling moment due to sideslip derivative $C_{l_\beta}$ may be found from

$$C_{l_{\beta_v}} = C_{Y_{\beta_v}} \cdot \frac{z_v \cdot cos(\alpha^*) - l_v \cdot sin(\alpha^*)}{b_w} \tag{3.55}$$

**Roll rate derivatives**

The vertical tail contribution to the side force due to roll rate derivative $C_{Y_p}$ may be found from

$$C_{Y_{p_v}} = 2 \cdot C_{Y_{\beta_v}} \cdot \frac{z_v \cdot cos(\alpha^*) - l_v \cdot sin(\alpha^*) - z_v}{b_w} + 3 \cdot sin(\Gamma) \cdot \left[1 - \frac{4z}{b_w} \cdot sin(\Gamma)\right] \cdot (C_{l_p})_{\substack{\Gamma=0 \\ C_L=0}} \tag{3.56}$$

where,
$z$ is the vertical distance between the wing's root quarter chord point and the aircraft's center of gravity.
and with $(C_{l_p})_{\substack{\Gamma=0 \\ C_L=0}}$ given by

$$(C_{l_p})_{\substack{\Gamma=0 \\ C_L=0}} = \frac{k}{\beta} \cdot \left[\frac{\beta \cdot C_{l_p}}{k}\right]_{C_L=0} \tag{3.57}$$

The vertical tail contribution to the yawing moment due to roll rate derivative $C_{n_p}$ may be found from

$$C_{n_{p_v}} = -\frac{2}{b_w^2} \cdot (l_v \cdot cos(\alpha^*) + z_v \cdot sin(\alpha^*)) \cdot (z_v \cdot cos(\alpha^*) - l_v \cdot sin(\alpha^*) - z_v) \cdot C_{Y_{\beta_v}} \tag{3.58}$$

The vertical tail contribution to the rolling moment due to roll rate derivative $C_{l_p}$ may be found from

$$C_{l_{p_v}} = 2 \cdot \left[\frac{z_v}{b_w}\right]^2 \cdot C_{Y_{\beta_v}} \tag{3.59}$$

**Yaw rate derivatives**

The vertical tail contribution to the side force due to yaw rate derivative $C_{Y_r}$ may be found from

$$C_{Y_{r_v}} = -2 \cdot C_{Y_{\beta_v}} \cdot \frac{l_v \cdot cos(\alpha^*) + z_v \cdot sin(\alpha^*)}{b_w} \tag{3.60}$$

The vertical tail contribution to the yawing moment due to roll rate derivative $C_{n_r}$ may be found from

$$C_{n_{r_v}} = \frac{2}{b_w^2} \cdot (l_v \cdot cos(\alpha^*) + z_v \cdot sin(\alpha^*))^2 \cdot C_{Y_{\beta_v}} \tag{3.61}$$

The vertical tail contribution to the rolling moment due to roll rate derivative $C_{l_r}$ may be found from

$$C_{l_{r_v}} = -\frac{2}{b_w^2} \cdot (l_v \cdot cos(\alpha^*) + z_v \cdot sin(\alpha^*)) \cdot (z_v \cdot cos(\alpha^*) - l_v \cdot sin(\alpha^*)) \cdot C_{Y_{\beta_v}} \tag{3.62}$$

**Rudder control derivatives**

The side force due to rudder deflection derivative may be found from

$$C_{Y_{\delta_r}} = \frac{C_{L_{\alpha_v}}}{c_{l_{\alpha_v}}} \cdot K' \cdot K_b \cdot \frac{(\alpha_{\delta_r})_{C_L}}{(\alpha_{\delta_r})_{c_l}} \cdot \left[\frac{c_{l_{\delta_r}}}{(c_{l_{\delta_r}})_{theory}}\right] \cdot (c_{l_{\delta_r}})_{theory} \cdot \frac{S_v}{S_w} \tag{3.63}$$

where,

$c_{l_{\alpha_v}}$ is the vertical empennage airfoil lift curve slope.

$K_b$ is the effect of taper ratio and rudder span correction factor.

$\frac{(\alpha_{\delta_r})_{C_L}}{(\alpha_{\delta_r})_{c_l}}$ is the effect of aspect ratio and rudder-chord ratio on the three dimensional rudder effectiveness.

The yawing moment due to rudder deflection derivative may be found from

$$C_{n_{\delta_r}} = -C_{Y_{\delta_r}} \cdot \frac{(l_v \cdot cos(\alpha^*) + z_v \cdot sin(\alpha^*))}{b_w} \tag{3.64}$$

The rolling moment due to rudder deflection derivative may be found from

$$C_{l_{\delta_r}} = \frac{(z_v \cdot cos(\alpha^*) - l_v \cdot sin(\alpha^*))}{b_w} \cdot C_{Y_{\delta_r}} \tag{3.65}$$

Applying Equation 3.51, the new stability derivatives data obtained with the previous methodology for the high-lift configurations and applying Equations 3.63 to 3.65, the new rudder control derivatives data can all be found on Table 3.11 for the aircrafts's equilibrium angle of attack ($\alpha^*$). It is due noticing that the Tecnam's coefficient data are the aircraft's published [20] estimates and were not obtained with the previous method.

Table 3.11: Stability and control derivatives estimation.

| *(per radian)* | | Tecnam P2006T | High-lift propellers | | | |
|---|---|---|---|---|---|---|
| | | | Ten | Twelve | Fourteen | Sixteen |
| Aerodynamic angle-of-sideslip derivatives | side force ($C_{Y_\beta}$) | -0.355 | -0.226 | -0.143 | -0.098 | -0.071 |
| | Yawing moment ($C_{n_\beta}$) | 0.0135 | 0.0074 | 0.0035 | 0.0014 | 0.0001 |
| | Rolling moment ($C_{l_\beta}$) | -0.029 | -0.026 | -0.019 | -0.015 | -0.014 |
| Roll rate derivatives | side force ($C_{Y_p}$) | 0.254 | 0.261 | 0.274 | 0.281 | 0.285 |
| | Yawing moment ($C_{n_p}$) | -0.130 | -0.128 | -0.128 | -0.127 | -0.127 |
| | Rolling moment ($C_{l_p}$) | -0.281 | -0.281 | -0.279 | -0.279 | -0.278 |
| Yaw rate derivatives | side force ($C_{Y_r}$) | 0.112 | 0.058 | 0.023 | 0.003 | -0.008 |
| | Yawing moment ($C_{n_r}$) | -0.106 | -0.065 | -0.038 | -0.023 | -0.014 |
| | Rolling moment ($C_{l_r}$) | 0.057 | 0.054 | 0.049 | 0.046 | 0.045 |
| Rudder control derivatives | side force ($C_{Y_{\delta_r}}$) | -0.040 | -0.030 | -0.023 | -0.019 | -0.016 |
| | Yawing moment ($C_{n_{\delta_r}}$) | -0.0304 | -0.0233 | -0.0164 | -0.0131 | -0.0108 |
| | Rolling moment ($C_{l_{\delta_r}}$) | 0.0009 | 0.0008 | 0.0006 | 0.0005 | 0.0004 |

#### 3.2.2.6 Case II — configuration selection

Table 3.12: Parameter reduction Dep implementation vs Tecnam.

| | | High-lift propellers | | | |
|---|---|---|---|---|---|
| | | Ten | Twelve | Fourteen | Sixteen |
| Reduction (%) | Vertical empennage area | 33.3 | 52.0 | 62.5 | 69.0 |
| | Empty weight | 5.9 | 7.1 | 7.6 | 7.8 |
| | Parasite drag coefficient | 13.1 | 13.3 | 14.4 | 15.3 |
| | Take-off field length | 31.0 | 24.1 | 18.2 | 13.9 |

A summary of the parameter reductions from the DEP implementation is presented on Table 3.12. Graphical representations of these reductions can be observed from Figure 3.9 to 3.11, for easier comparison and understanding of the consequent relations.

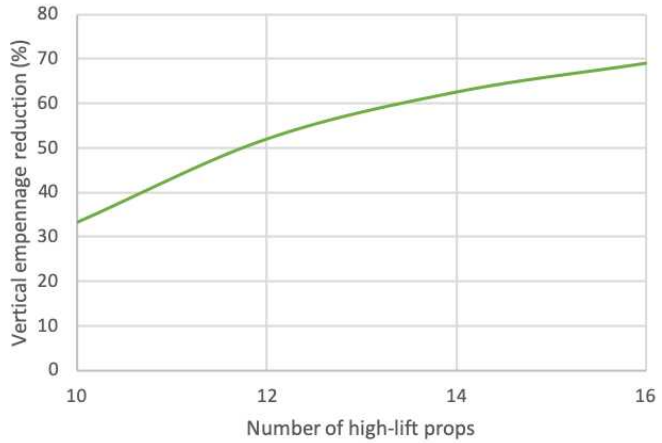


Figure 3.9: Graphical representation of the vertical empennage area reduction.

In figure 3.9, the vertical empennage area reduction was plotted versus the number of engines and it is possible to identify what is presumed to be a logarithmic relation between the two axis: the higher the number of high-lift props, the bigger the area reduction(presumably until a certain point where the stability requirement would be the dimensioning criteria). A reduction of half of vertical empennage is achieved for twelve high-lift props and of around two thirds for the studied configuration with higher number of high-lift props.

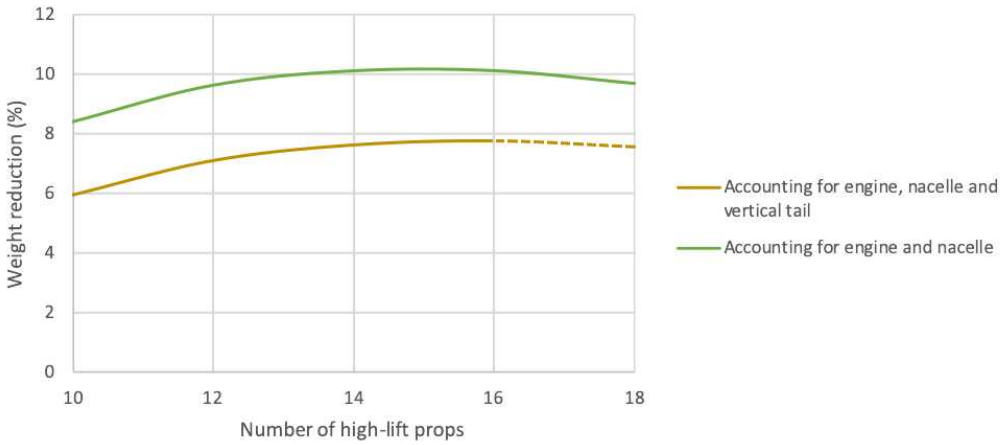


Figure 3.10: Graphical representation of the weight reduction.

In Figure 3.10, not only the data including the influences of the vertical empennage, nacelles and engines on the total weight reduction (from Table 3.12), but also the influence of the propulsion system alone (nacelles plus engines) was plotted. In this last series, the nacelles' weight was computed with Equation 3.16 and the engine data was obtained from the same published data[80]. As so, it was possible to plot the curve accounting for 18 high-props and to extrapolate that data to the other curve (dashed line). Looking at the plot, it is evident that there is no linear relation between the number of high-lift props and the weight reduction (possibly negative quadratic), and that adding more engines is only increasingly beneficial to a certain point: in this case, up to around fourteen high-lift props.

In Figure 3.11, a high slope linear relation between the number of high-lift props and the parasite drag reduction appears for three last data points, and an almost irrelevant reduction can be observed from ten to twelve high-lift props.

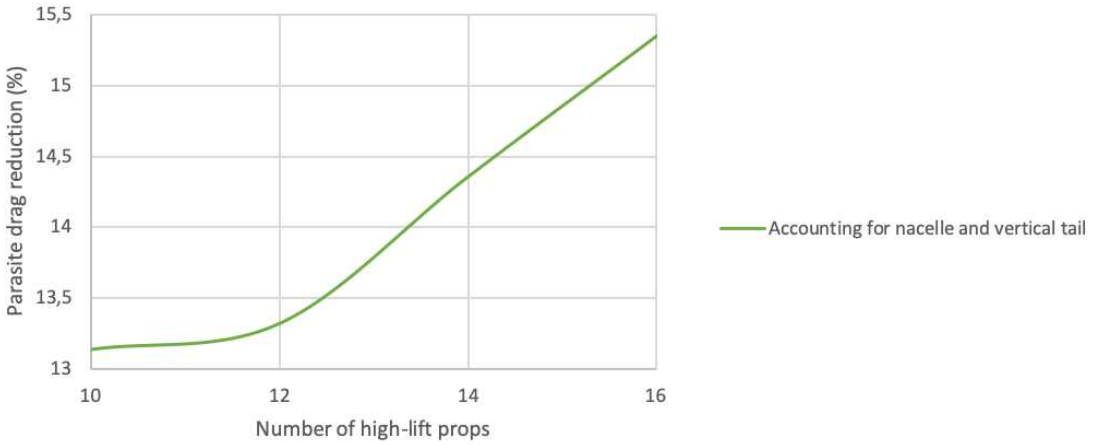


Figure 3.11: Graphical representation of the parasite drag reduction.

Contrarily to the previous graphics, in Figure 3.12 a negative slope almost linear relation can be found between the total take-off field length and the number of high lift props. This is due to the total thrust decrease as the number of electric engines increases, shown in publications[80] for the engines considered. Even so, for the most optimistic case (ten engines) uses only two thirds of the original field length for take-off.

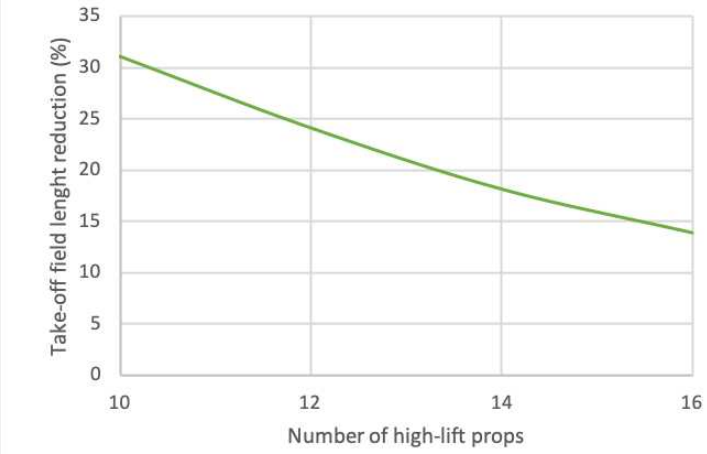


Figure 3.12: Graphical representation of the take-off field length reduction.

Although based on this data the fourteen high-lift props configuration seems to be the most promising configuration, a more accurate and complete analysis evolving a greater number of parameters would be necessary to effectively evaluate the best configuration amongst the four proposed. The author decided to choose the twelve high-lift propellers configuration, similarly to the existent Tecnam modification by NASA — X-57 Maxwell. Although this comparison didn't allow to draw a full conclusion on the choice of configuration, it is possible to see the influence of the number of engines on the vertical tail size, weight, inertia, drag and take-off field length.

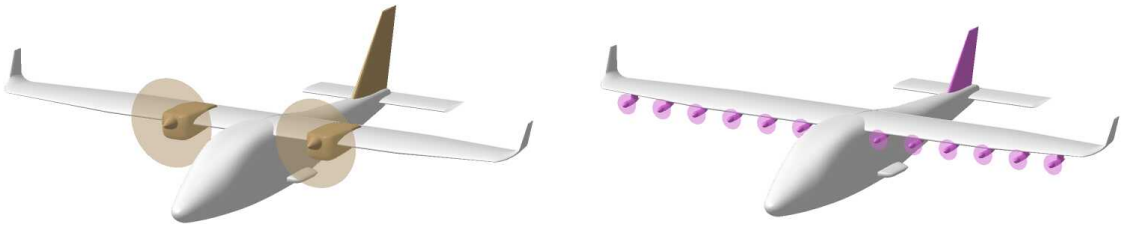

Figure 3.13: DEP implementation: Representation of the before (Case I) and after (Case II).

### 3.2.3 Model Parameters

The following parameters will be used for the design of the control system and simulations of the following chapters. From Table 3.13 to Table 3.17 data for the geometrical, mass, propulsion, performance and aerodynamic characteristics of this DEP aircraft can be found.
In Figure 3.14 the three-view drawing is shown and in Figure 3.15 an example of the distributed propulsion schematics of this configuration can be found, in order to provide a better understanding of its differential propulsion dynamic.

Table 3.13: DEP Configuration Aircraft Geometric Characteristics.

| Geometrical Characteristics | | | |
|---|---|---|---|
| Wing span | $b_w$ | 11.4 | $m$ |
| Wing area | $S_w$ | 14.8 | $m^2$ |
| Wing mean-chord | $c_w$ | 1.3 | $m$ |
| Vertical tail span | $b_v$ | 1.2 | $m$ |
| Vertical tail area | $S_v$ | 1.07 | $m^2$ |
| Vertical tail mean-chord | $c_v$ | 0.76 | $m$ |
| Fuselage length | $l_{fus}$ | 8.7 | $m$ |
| Fuselage height | $h_{fus}$ | 2.85 | $m$ |

Table 3.14: DEP Configuration Aircraft Mass Characteristics.

| Mass Characteristics | | | |
|---|---|---|---|
| Maximum Take-off Weight | $W_{TO}$ | 1096 | $kg$ |
| Standard Equipped Weight | $W_{empty}$ | 676 | $kg$ |
| Standard Useful Load | $W_{useful}$ | 420 | $kg$ |
| $X_{cg}$ Maximum Forward | $X_{cg_f}$ | 16.5 | $\%MAC$ |
| $X_{cg}$ Maximum Aft | $X_{cg_a}$ | 31 | $\%MAC$ |
| Rolling mass Moment of Inertia | $Ixx$ | 1723 | $kg\ m^2$ |
| Pitching mass Moment of Inertia | $Iyy$ | 1809 | $kg\ m^2$ |
| Yawing mass Moment of Inertia | $Izz$ | 3015 | $kg\ m^2$ |
| Roll-Yaw Product of Inertia Ixy | $Ixy$ | 0 | $kg\ m^2$ |
| Yaw-Pitch Product of Inertia Iyz | $Iyz$ | 0 | $kg\ m^2$ |
| Pitch-Roll Product of Inertia Izx | $Izx$ | 194 | $kg\ m^2$ |

Table 3.15: DEP Configuration Aircraft Propulsion Characteristics.

| Propulsion Characteristics | | | |
|---|---|---|---|
| Maximum Power | $P_{max}$ | $11.5$ | $kW$ |
| Propeller disk area | $A_{prop}$ | $0.52$ | $m^2$ |
| Engine axial distance to cg | $l_{x_T}$ | $-0.17$ | $m$ |
| Engine side distance to cg | $l_{y_{T_{(1,12)}}}$ | $\pm 4.82$ | $m$ |
| Engine side distance to cg | $l_{y_{T_{(2,11)}}}$ | $\pm 4.03$ | $m$ |
| Engine side distance to cg | $l_{y_{T_{(3,10)}}}$ | $\pm 3.24$ | $m$ |
| Engine side distance to cg | $l_{y_{T_{(4,9)}}}$ | $\pm 2.45$ | $m$ |
| Engine side distance to cg | $l_{y_{T_{(5,8)}}}$ | $\pm 1.66$ | $m$ |
| Engine side distance to cg | $l_{y_{T_{(6,7)}}}$ | $\pm 0.87$ | $m$ |
| Engine incidence angle | $\varepsilon_{T_e}$ | $0$ | $deg$ |

Table 3.16: DEP Configuration Aircraft Performance Characteristics.

| Performance Characteristics | | | |
|---|---|---|---|
| Stall Speed Flap Down | $V_S$ | $23.5$ | $m/s$ |
| Take-off Distance | $S_{TO}$ | $274$ | $m$ |
| Take-off Run | $S_G + S_R$ | $166$ | $m$ |

Table 3.17: DEP Configuration Aircraft Aerodynamic Characteristics.

| Aerodynamic Characteristics | | | |
|---|---|---|---|
| Zero-lift drag derivative | $C_{D_0}$ | $0.02895$ | $(per\ radian)$ |
| Drag due to angle of attack derivative | $C_{D_\alpha}$ | $0.222$ | $(per\ radian)$ |
| Zero angle of attack lift derivative | $C_{L_0}$ | $0.289$ | $(per\ radian)$ |
| Lift due to angle of attack derivative | $C_{L_\alpha}$ | $4.152$ | $(per\ radian)$ |
| Pitching moment at zero angle of attack | $C_{m_0}$ | $-0.922$ | $(per\ radian)$ |
| Pitching moment due to angle of attack derivative | $C_{m_\alpha}$ | $-0.871$ | $(per\ radian)$ |
| Pitching moment due to pitch rate derivative | $C_{m_q}$ | $-14.799$ | $(per\ radian)$ |
| Pitching moment due to stabilator deflection derivative | $C_{m_{\delta_e}}$ | $-1.811$ | $(per\ radian)$ |
| Side force due to sideslip derivative | $C_{Y_\beta}$ | $-0.143$ | $(per\ radian)$ |
| Side force due to roll rate derivative | $C_{Y_p}$ | $0.274$ | $(per\ radian)$ |
| Side force due to yaw rate derivative | $C_{Y_r}$ | $0.023$ | $(per\ radian)$ |
| Side force due to aileron deflection derivative | $C_{Y_{\delta_a}}$ | $0.127$ | $(per\ radian)$ |
| Side force due to rudder deflection derivative | $C_{Y_{\delta_r}}$ | $-0.023$ | $(per\ radian)$ |
| Yawing moment due to sideslip derivative | $C_{n_\beta}$ | $0.0035$ | $(per\ radian)$ |
| Yawing moment due to roll rate derivative | $C_{n_p}$ | $-0.128$ | $(per\ radian)$ |
| Yawing moment due to yaw rate derivative | $C_{n_r}$ | $-0.038$ | $(per\ radian)$ |
| Yawing moment due to aileron deflection derivative | $C_{n_{\delta_a}}$ | $-0.009$ | $(per\ radian)$ |
| Yawing moment due to rudder deflection derivative | $C_{n_{\delta_r}}$ | $-0.0164$ | $(per\ radian)$ |
| Rolling moment due to sideslip derivative | $C_{l_\beta}$ | $-0.019$ | $(per\ radian)$ |
| Rolling moment due to roll rate derivative | $C_{l_p}$ | $-0.279$ | $(per\ radian)$ |
| Rolling moment due to yaw rate derivative | $C_{l_r}$ | $0.049$ | $(per\ radian)$ |
| Rolling moment due to aileron deflection derivative | $C_{l_{\delta_a}}$ | $-0.045$ | $(per\ radian)$ |
| Rolling moment due to rudder deflection derivative | $C_{l_{\delta_r}}$ | $0.0006$ | $(per\ radian)$ |

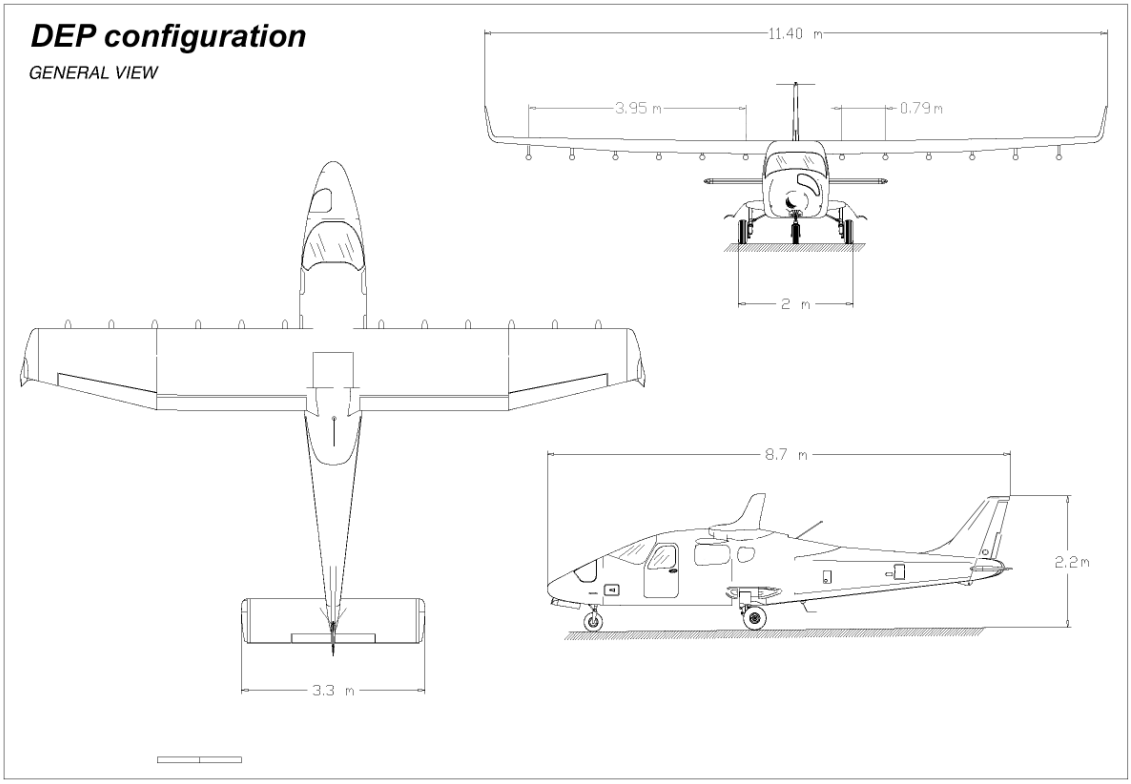


Figure 3.14: Three view drawing of DEP Configuration Aircraft.

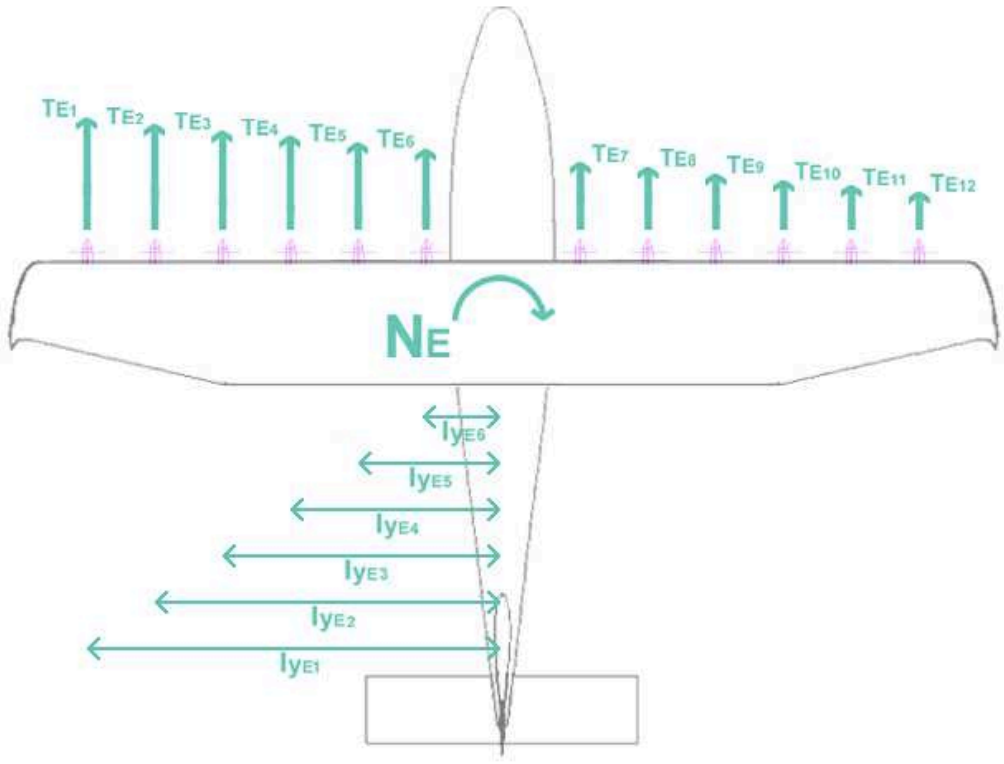


Figure 3.15: Example of propulsion schematics for the DEP Configuration Aircraft.

# Chapter 4

# Lateral-Directional Robust Controller

For a control system to operate properly in realistic scenarios it requires a particular propriety commonly named robustness. This propriety ensures that the controller performs satisfactorily not just for one plant, but for a family of plants.
Aircraft control systems need to be developed so that certain key system properties remain almost unchanged when subjected to disturbances. In the design of robust controllers it is intended to obtain a controller that meets design specifications under normal system operating conditions and ensures satisfactory performance in the presence of disturbances. The roll and yaw controller will thus be designed to meet robustness specifications related to model uncertainties, external disturbances, and/or sensor inaccuracies, for the control surface case and the hybrid case.
The LQR is a controller based on the optimal control theory that is intended for a linear system and aims to determine the optimal system solution taking into account the minimisation of a quadratic performance criterion. LQR is an optimal controller because it provides the best possible performance by providing the smallest input error. Its state feedback scheme provides a gain matrix $K$ that minimizes the objective function in order for the system to achieve a compromise between control effort use, amplitude and response time, while remaining stable.
In $H_\infty$ control theory the $H_\infty$ norm of a system measures its robustness by quantifying the worst-case behaviour of a perturbed system, performing efficiently in the face of atmospheric turbulence and other disturbances, by having a low settling time, although having a slightly high peak overshoot (due to the worst-case behaviour pursue). This method is hence used to synthesise controllers to achieve stabilisation with guaranteed performance, interpreting the control problem as a mathematical optimisation problem and solving that optimisation. One disadvantage of the $H_\infty$ technique is precisely the level of mathematical understanding needed to apply it successfully.
In this Chapter the full dynamics of the aircraft is modelled, focusing on the gain design and structure of both cases' lateral-directional controllers. The gain for an $LQR$ and an $H_\infty$ controllers is designed and compared for case I, in order to prove the $H_\infty$ controller robustness and validate the controller selection. Afterwards, the corresponding control-surface controller structure is specified. For case II, the previously validated $H_\infty$ gain design is computed, and the hybrid-controller specifications as well as the corresponding hybrid structure (with a standalone propulsion control operation mode as well as a conventional mode) are described.

## 4.1 Dynamic model

Dynamic models are the core of understanding systems' dynamics. These models may either be empirical (from data) or physics-based (from fundamental relations), relying on knowledge of the physical process. A combination of the two approaches was used in Chapter 3 and the unknown or uncertain parameters were estimated. Based on those parameters, the dynamic model of both study cases was developed as follows.

### 4.1.1 Trim model

An aircraft is said to be trimmed, when it is put in a state of equilibrium by the action of the pilot adjusting the controls. In trim there can be no translational or rotational acceleration. If the aircraft is trimmed on a steady, straight flight condition, all time derivatives are zero and there is no angular velocity about the centre of gravity, setting to zero all time derivatives, the angular velocities $p, q, r$, and the time derivatives of angular position (attitude). If the motion is restricted to symmetric flight, the bank angle is also zero. Although, the velocity components $v$ and $w$ are not necessarily zero. This is the simplest case of steady flight, making it easy to solve the nonlinear model dynamic equations for the state and control variables. As more detailedly specified in the subsection 4.1.2, aircraft's flight dynamics are essentially non-linear and their motion can be described as a function of the aircraft's state and control variables,

$$\dot{x} = f(x, u) \tag{4.1}$$

The non-linear equilibrium (or trimmed) point $(x^*, u^*)$ can then be found by solving

$$f(x^*, u^*) = 0 \tag{4.2}$$

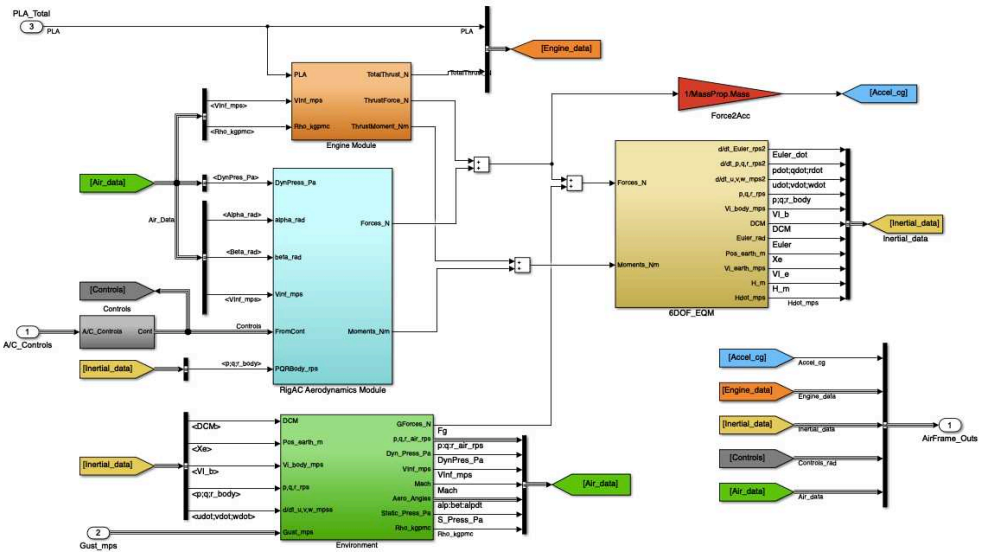


Figure 4.1: 6DoF dynamic model

A generic 6DoF Simulink[1] dynamic model, courtesy of Embraer, was modified to represent each one of the two cases being studied - the original Tecnam P2006T aircraft and the proposed modification. This model, represented in 4.1, is composed by an Engines block, a Rigid Aircraft Aerodynamics block, an Environment block and a 6DoF Motion Equations block. Both cases' models share the same block modules apart from the Engines block (detailed in Chapter 4.1.1.1), in which each engine was modelled with the same set of equations, but having a different number of propellers for each case. The parameters inserted also vary for each one of the cases both in the Engines and Rigid Aircraft Aerodynamics blocks (data from Sections 3.2.3 and 3.2.3).
A Matlab[1] script, also courtesy of Embraer, was altered to match both study-cases' aircraft states and controls, in order to be implemented in the developed Simulink[1] 6DoF model, and trim them at Mach $0.18$ and a $2450\ m$ altitude — steady, straight flight condition.

[1]MATLAB R2018a, The MathWorks Inc.

#### 4.1.1.1 Engines block

In the next figure, the Simulink[1] engine block subsystem is presented. For Case I it has one throttle input and for Case II it has twelve throttle inputs, other inputs are the airspeed $V_\infty$ and air density $\rho$. The outputs going in the 6DoF Motion Equations block are the total Thrust, each component ($X$,$Y$ and $Z$) of the Thrust Force and each component ($\bar{L}$,$M$ and $N$) of the Thrust Moment.

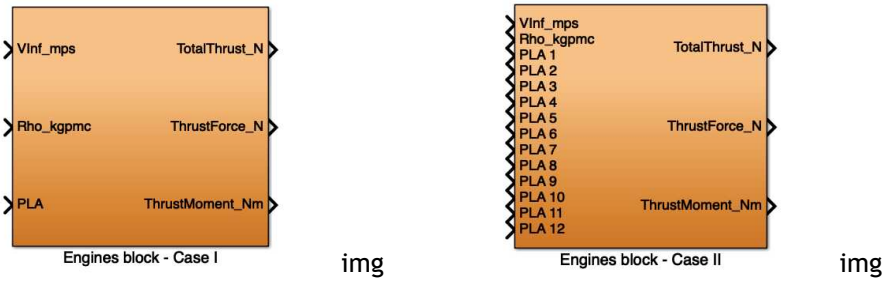


(a) Case I img (b) Case II img

Figure 4.2: 6DoF dynamic model - Engines block

The engine's power $P_e$ depending on the engine's throttle $\delta_{th}$, was modelled according to the following equations

$$P_0 = P_{max} \cdot \delta_{th} \tag{4.3}$$

$$P_e = \left(\frac{\rho}{\rho_0} - \frac{\rho/\rho_0 + 1}{7.55}\right) \cdot P_0 \tag{4.4}$$

where,
$P_O$ is the engine's power for the set throttle, at sea level.
$\delta_{th}$ is the throttle position.
$P_{max}$ is the engine's maximum power.
$P_e$ is the engine's power.

For the DEP engines $P_e$ was assumed to be equal to $P_O$. The correspondent engine's thrust $T$ is assumed to be a function of airspeed, power and propeller efficiency, which is a function of altitude and propeller area, so that *(in imperial units)* each engine thrust is given by

$$T = \frac{\eta_P \cdot P_e \cdot 550}{V} \tag{4.5}$$

$$\eta_P = \frac{V}{V + v_i} \tag{4.6}$$

$$v_i = -\frac{V}{2} + \sqrt{\left(\frac{V}{2}\right)^2 + \frac{T}{2 \cdot A_{prop} \cdot \rho}} \tag{4.7}$$

[1] MATLAB R2018a, The MathWorks Inc.

where,
$T$ is the engine's thrust.
$\eta_P$ is the propellers's efficiency.
$V$ is the flight velocity.
$v_i$ is the induced velocity.
$A_{prop}$ is the propeller disk area.

The engine's dynamics were modelled according to the following first order differential equation

$$\dot{T} = \frac{1}{\tau_e} \cdot \left(\delta_{th} \cdot T_{max}(h, V) - T\right) \tag{4.8}$$

With $\tau_e$ being the engine's time constant, given by

$$\tau_e = \frac{1}{5} \cdot t_{Tr} \tag{4.9}$$

where,
$t_{Tr}$ is the engine's thrust response time, also known as settling time and defined as the time within which the desired system's response is attained and remains within a $\pm 2\%$ error margin of its stationary Thrust value.
Publications [38] suggest this Thrust response time for an electric engine to be about 0.2 seconds, so the author considered that time interval during simulations.
The forces associated with engine thrust were modelled as follows

$$\begin{aligned} X_T &= X_{T_{e_1}} + X_{T_{e_2}} + ... + X_{T_{e_n}} \\ &= T_{e_1} \cdot cos(\varepsilon_{T_{e_1}}) + T_{e_2} \cdot cos(\varepsilon_{T_{e_2}}) + ... + T_{e_n} \cdot cos(\varepsilon_{T_{e_n}}) \end{aligned} \tag{4.10a}$$

$$Y_T = (L_{sec_1} - W_{sec_1}) \cdot sin(\phi) + (L_{sec_2} - W_{sec_2}) \cdot sin(\phi) + ... + (L_{sec_n} - W_{sec_n}) \cdot sin(\phi) \tag{4.10b}$$

$$\begin{aligned} Z_T &= Z_{T_{e_1}} + Z_{T_{e_2}} + ... + Z_{T_{e_n}} \\ &= (T_{e_1} \cdot sin(\varepsilon_{T_{e_1}}) + F_{T_{e_1}}) + (T_{e_2} \cdot sin(\varepsilon_{T_{e_2}}) + F_{T_{e_2}}) + ... + (T_{e_n} \cdot sin(\varepsilon_{T_{e_n}}) + F_{T_{e_n}}) \end{aligned} \tag{4.10c}$$

Lift force is proportional to the dynamic pressure that is proportional to the airspeed. Since when using differential thrust each engine's speed differs (or may differ), each propeller's speed is (or may be) different from the others, subsequently changing the dynamic pressure of the wing section affected by the engine slipstream and consequently altering the lift on that section. This lift force variation along the wing sections (illustrated in Figure 4.3) causes a roll motion.
Here, the index $n$ represents each one of the engines and the subscript ($sec_n$) concerns each engine wing affected section. The force $F_{T_{e_n}}$ is the difference between the section's weight and lift (Equation 4.11), if the difference is null in all sections the aircraft won't roll.

$$\begin{aligned} F_{T_{e_n}} &= W_{sec_n} + L_{sec_n} \cdot cos(\phi) \\ &= W_{w_{sec_n}} + W_{e_n} + L_{sec_n} \cdot cos(\phi) \end{aligned} \tag{4.11}$$

where,
$W_{w_{sec_n}}$ is the engine $n$ wing affected section's weight.
$W_{e_n}$ is each engine's weight.
$L_{sec_n}$ is the lift force in the engine $n$ wing affected section.

An aircraft's lift force equation may be written as

$$L = C_L \cdot \bar{Q} \cdot S_w \tag{4.12}$$

At cruise conditions $L = W$, considering this relation the cruise lift coefficient is given by

$$C_L = \frac{W}{\bar{Q} \cdot S_w} \tag{4.13}$$

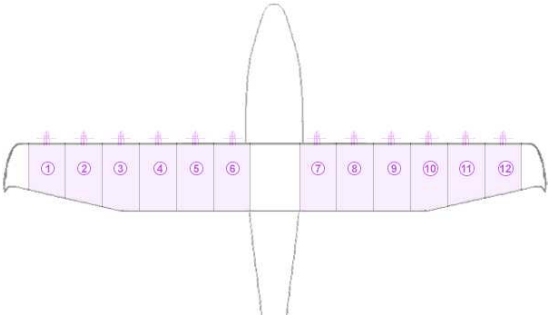


Figure 4.3: Schematics of the wing's section division.

Assuming $L_{sec_n} = W_{sec_n}$ for each section of the wing, the lift at a determined engine's $n$ wing affected section at levelled cruise is given by

$$L_{sec_n} = C_{L_{sec_n}} \cdot \bar{Q}_{sec_n} \cdot S_{sec_n} \tag{4.14}$$

with,

$$C_{L_{sec_n}} = \frac{W_{sec_n}}{\bar{Q} \cdot S_{sec_n}} \tag{4.15}$$

and assuming that the wing's weight can be approximated to vary proportionally to its area,

$$W_{w_{sec_n}} = \frac{W_w \cdot S_{sec_n}}{S_w} \tag{4.16}$$

The dynamic pressure in each wing section is given by the following equation, where the speed associated with each section ($V_{sec}$) depends on the speed induced by its respective engine

$$\bar{Q}_{sec_n} = \frac{1}{2} \cdot \rho \cdot V_{sec}^2 \tag{4.17}$$

In this case $\varepsilon_{T_e} = 0$, so the moments associated with engine thrust are given by

$$L_T = l_{y_{T_{e_1}}} \cdot Z_{T_{e_1}} + l_{y_{T_{e_2}}} \cdot Z_{T_{e_2}} + ... + l_{y_{T_{e_n}}} \cdot Z_{T_{e_n}} \tag{4.18a}$$

$$M_T = l_{x_{sec_1}} \cdot Z_{T_{e_1}} + l_{x_{sec_2}} \cdot Z_{T_{e_2}} + ... + l_{x_{sec_n}} \cdot Z_{T_{e_n}} \tag{4.18b}$$

$$N_T = l_{y_{T_{e_1}}} \cdot X_{T_{e_1}} + l_{x_{sec_1}} \cdot Y_{T_{e_1}} + l_{y_{T_{e_2}}} \cdot X_{T_{e_2}} + l_{x_{sec_2}} \cdot Y_{T_{e_2}} + ... + l_{y_{T_{e_n}}} \cdot X_{T_{e_n}} + l_{x_{sec_n}} \cdot Y_{T_{e_n}} \tag{4.18c}$$

where,
$l_{y_T}$ is the distance distance perpendicular to the longitudinal axis between the vehicle's and the engine's centre of gravity.
$l_{x_{sec}}$ is the distance distance parallel to the longitudinal axis between the vehicle's and each section's centre of gravity.

On Equation 4.18b, it is assumed that in the longitudinal dynamics, the stabilator can compensate the small pitch moment generated by this form of control with a small $\delta_e$ deflection, as the distances $l_{x_{sec_n}}$ is short and the component $Z_T$ doesn't attain large values.
It is due noticing that there are although some limitations in this engine model, such as in Equation 4.6 the ideal propeller efficiency is considered, but the actual efficiency is lower because of energy losses due to slipstream rotation, blade profile drag, non-uniform flow, compressibility effects and propeller blockage.

### 4.1.2 Linear model

When the origin a body-fixed system of coordinates is fixed at the centre of gravity of the aircraft, which is in an equilibrium (or trimmed) state of motion along a nominal flight path, then, when only small perturbations of the aircraft's motion about this equilibrium state are considered, the corresponding equations of motion can be linearised. [1]

As aircraft's flight dynamics are essentially non linear and non linear problems are significantly more complex to solve than linear problems, it's possible to linearise the dynamic model around the equilibrium (or trimmed) point to simplify the control law design.

The two most common modelling and analysis approaches for linear systems are the transfer-function approach and the state-space approach. This work will adopt the latter representation, as it allows the representation of the process under examination by systems of first-order differential equations.

A multivariable linear time-invariant dynamic system can be described in a state-space representation by an input and an output equations, defined in Equations 4.19a and 4.19b, respectively.

$$\begin{cases} \dot{x} = A \cdot x + B \cdot u & \text{(4.19a)} \\ y = C \cdot x + D \cdot u & \text{(4.19b)} \end{cases}$$

The state equation is a first order vector differential equation, which represents the equation of motion of an aircraft, and where $x \in \mathbb{R}^n$ is the state vector, $u \in \mathbb{R}^m$ the control vector, $A \in \mathbb{R}^{n \times n}$ the state coefficient matrix and $B \in \mathbb{R}^{n \times m}$ the driving matrix. The elements of vector $x$ are the state variables and the elements of the vector $u$ are the control input variables. For the lateral-directional motion, these vectors will be defined in this work according to Equations 4.20 to 4.23.

$$x_{case_I} = \begin{bmatrix} v & \phi & \psi & p & r \end{bmatrix} \tag{4.20}$$

$$x_{case_I} = \begin{bmatrix} v & \phi & \psi & p & r \end{bmatrix} \tag{4.21}$$

$$u_{case_I} = \begin{bmatrix} \delta_a & \delta_r \end{bmatrix} \tag{4.22}$$

$$u_{case_{II}} = \begin{bmatrix} \delta_a & \delta_r & \delta_{th_1} & \delta_{th_2} & \delta_{th_3} & \delta_{th_4} & \delta_{th_5} & \delta_{th_6} & \delta_{th_7} & \delta_{th_8} & \delta_{th_9} & \delta_{th_{10}} & \delta_{th_{11}} & \delta_{th_{12}} \end{bmatrix} \tag{4.23}$$

The jacobian state coefficient matrix $A$ and jacobian the driving matrix $B$ can be obtained by linearisation of the aircraft's non-linear equations of motion around the equilibrium (or trimmed) point for the steady, straight flight condition previously considered, so that

$$A = \left( \frac{\partial f}{\partial x} \right)_{\substack{x=x^* \\ u=u^*}}, \quad B = \left( \frac{\partial f}{\partial u} \right)_{\substack{x=x^* \\ u=u^*}} \tag{4.24}$$

A Matlab[1] script was developed in order to compute the previous equation and obtain both matrices for the lateral-directional motion of each case, results will be further ahead introduced.

[1] MATLAB R2018a, The MathWorks Inc.

An aircraft's flight can be affected by atmospheric turbulence and other disturbances, such factors will be considered random and taken into account by adding a third term to Equation 4.19a, where $d \in \mathbb{R}^l$ is the disturbance vector with an associated matrix $E \in \mathbb{R}^{n \times l}$, as follows

$$\dot{x} = A \cdot x + B \cdot u + E \cdot d \tag{4.25}$$

The output equation is an algebraic equation depending on the state vector $x$ and, occasionally, also on the control vector $u$, and where $y \in \mathbb{R}^p$ is the state vector, $C \in \mathbb{R}^{p \times n}$ the output matrix and $D \in \mathbb{R}^{p \times m}$ the direct matrix. The elements of vector $y$ are the output variables. For the lateral-directional motion, this vector will be defined in this work according to Equation 4.26.

$$y = \begin{bmatrix} \phi & \psi \end{bmatrix} \tag{4.26}$$

This work will adopt the proposed augmented system from Reference [89]. Considering the previously defined plant: $A$ is from now on referred to as $A_p$, $B$ as $B_p$, $C$ as $C_p$ and $x$ as $x_p$. The augmented system's state will be defined regarding the plant state $x_p$ and the integrator state $x_e$, as follows.

$$x = \begin{bmatrix} x_p & x_e \end{bmatrix} \tag{4.27}$$

Here, the integrator state's derivative can be defined as the difference between the current output and the reference output.

$$\dot{x}_e = y - y_{ref} \tag{4.28}$$

Substituting Equation 4.19b in the previous Equation, considering $D = 0$ and naming $y_{ref}$ as $r$ for simplicity, $\dot{x}_e$ is now defined to be

$$\dot{x}_e = C_p \cdot x_p - r \tag{4.29}$$

If Equations 4.29 and 4.25 are combined, then the augmented system's state can be defined in form of a system by the following Equation.

$$\begin{cases} \dot{x}_p = A_p \cdot x_p + B_p \cdot u + E \cdot d \\ \dot{x}_e = C_p \cdot x_p - r \end{cases} \tag{4.30}$$

In matrix form, this is equal to

$$\begin{bmatrix} \dot{x}_p \\ \dot{x}_e \end{bmatrix} = \begin{bmatrix} A_p & 0 \\ C_p & 0 \end{bmatrix} \cdot \begin{bmatrix} x_p \\ x_e \end{bmatrix} + \begin{bmatrix} B_p \\ 0 \end{bmatrix} \cdot u + \begin{bmatrix} E \\ 0 \end{bmatrix} \cdot d + \begin{bmatrix} 0 \\ -I \end{bmatrix} \cdot r \tag{4.31}$$

and if,

$$A = \begin{bmatrix} A_p & 0 \\ C_p & 0 \end{bmatrix}, \quad B = \begin{bmatrix} B_p \\ 0 \end{bmatrix}, \quad C = \begin{bmatrix} C_p & 0 \end{bmatrix},$$
$$\bar{E} = \begin{bmatrix} E \\ 0 \end{bmatrix}, \quad B_r = \begin{bmatrix} 0 \\ -I \end{bmatrix} \tag{4.32}$$

The augmented system's state and output equations are now defined according to the following equations, respectively.

$$\begin{cases} \dot{x} = A \cdot x + B \cdot u + \bar{E} \cdot d + B_r \cdot r & \text{(4.33a)} \\ y = C \cdot x & \text{(4.33b)} \end{cases}$$

For disregarding disturbances noises, Equation 4.19a should be used instead of Equation 4.25 in Equation 4.30.

The relation between the non-linear equilibrium (or trimmed) point $(x^*, u^*)$ and the linear equilibrium (or trimmed) point $(\bar{x}, \bar{u})$ is given by the following Equation.

$$\begin{cases} \bar{x} = x - x^* & \text{(4.34a)} \\ \bar{u} = u - u^* & \text{(4.34b)} \end{cases}$$

### 4.1.3 Controllability

Controllability means that the control input $u(t)$ independently affects all the system modes. According to Kalman, state controllability is determined by the state coefficient matrix $A$ and the driving matrix $B$ using the following equation [90]

$$U = [B \; AB \; A^2B \; ... \; A^{n-1}B] \tag{4.35}$$

The system is controllable if the controllability matrix $U$ has full rank of $n$, that is, if $U$ has $n$ linearly independent columns.

### 4.1.4 Static Stability

A lateral-directional flight is in equilibrium when the lateral force and yawing and rolling moments are all null, that is, when the side force ($C_Y$), yawing moment ($C_n$) and rolling moment ($C_l$) are all null.

When changing the sideslip angle ($\beta$) of an aircraft from a yaw equilibrium position ($\beta_{eq}$) on-flight, it is desirable for the aircraft to return to this equilibrium yaw angle $\beta_{eq}$ (without any pilot or autopilot action). If this happens, then the aircraft is statically stable at this directional equilibrium value of the sideslip angle $\beta_{eq}$. This occurs if the following condition is verified

$$C_{n_\beta} > 0 \tag{4.36}$$

The most important factor influencing lateral stability is the dihedral angle (angle between the aircraft's $xy$ plane and the wing plane), other factors are the interaction between the wing, the fuselage and the tail of the aircraft. Aircraft lateral static stability occurs if the following condition is verified

$$C_{l_\beta} < 0 \tag{4.37}$$

### 4.1.5 Flying and Handling qualities

Flying qualities may be defined as the ease and precision with which an aircraft responds to the pilot's commands. These qualities are generally described by parameters such as the damping ratio and undamped natural frequency and knowing them allows for the understanding of the aircraft's behaviour after pilot commands or disturbances.

Both flying and handling qualities depend on the aircraft's stability and control characteristics and for lateral-directional motion they're essentially the same throughout the flight, in the context of small perturbation modelling.

Handling qualities are substantially subjective, reflecting the ease with which a pilot considers an aircraft (with determined flying qualities) is piloted. These qualities are therefore dependent on pilot's opinions and can be assessed based on the Cooper-Harper [22] grade scale.

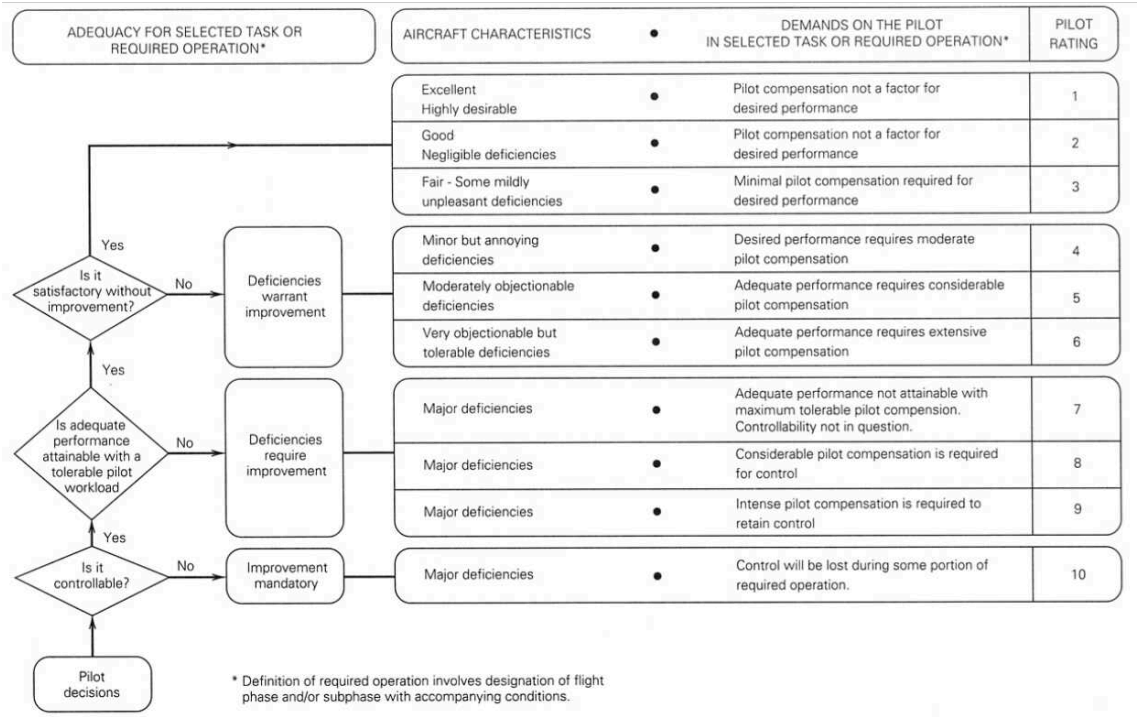


Figure 4.4: Cooper-Harper Handling qualities rating scale. [22]

This method aims to grade the dynamic behaviour of an aircraft according to the class of aircraft (I-IV) and flight phase category (A, B and C). The aircraft's dynamic characteristics are then graded between levels 1-3 as described in Tables 4.1 to 4.6 and according to Figure 4.4. For the lateral-directional motion, the three handling qualities modes (Roll, Dutch roll and Spiral) can be identified and analysed using the eigenvalues of the state matrix A. This matrix's characteristic equation is of the form

$$a_n\lambda^n + ... + a_2\lambda^2 + a_1\lambda^1 + a_0 = 0 \tag{4.38}$$

where $a_n$ are constant parameters depending on matrix A and $\lambda$ represents the matrix's eigenvalues. Equation 4.38 has $n$ solutions that correspond to the $n$ eigenvalues of the state matrix and take the form

$$\lambda = a \pm jb \tag{4.39}$$

An analysis of the aircraft's lateral-directional handling qualities can now be done by implementing the next set of equations, corresponding to the natural frequency, damping, time to double/halve and time constant, respectively.

$$\omega_n = |\lambda| \tag{4.40}$$

$$\xi = -\frac{a}{\omega_n} \tag{4.41}$$

$$T_2 = T_{\frac{1}{2}} = \frac{ln2}{|a|} \tag{4.42}$$

$$\tau = \frac{1}{|\lambda|} \tag{4.43}$$

Table 4.1: Classification of airplanes. [25]

| | |
|---|---|
| Class I | Small, light airplanes (such as light utility, primary trainer, and light observation craft) |
| Class II | Medium-weight, low-to-medium maneuverability airplanes (such as heavy utility/search and rescue, light or medium transport/cargo/tanker, reconnaissance, tactical bomber, heavy attack and trainer for Class II) |
| Class III | Large, heavy, low-to-medium maneuverability airplanes (such as heavy transport/cargo/tanker, heavy bomber, and trainer for Class III) |
| Class IV | Heavy maneuverability airplanes (such as fighter/interceptor, attack, tactical reconnaissance, observation and trainer for Class IV) |

Table 4.2: Flight phase categories. [25]

| | |
|---|---|
| Category A | Nonterminal flight phases that require rapid maneuvering, precision tracking or precise flight path control, such as air-to-air combat, in-flight refuelling (receiver), terrain-following and close formation flying (applies only to military aircraft). |
| Category B | Nonterminal flight phases that are normally accomplished using gradual manoeuvres and no precision tracking, although accurate flight path control may be required. Includes climb, cruise, loiter, descent, in-flight refuelling (tanker) and aerial delivery |
| Category C | Terminal flight phases requiring gradual manoeuvres but precise flight path control. Include takeoff, catapult takeoff, approach, wave-off/go-around, and landing. |

Table 4.3: Classification of airplanes. [25]

| | |
|---|---|
| Level 1 | Flying qualities clearly adequate for the mission flight phase. |
| Level 2 | Flying qualities adequate to accomplish the mission flight phase but with some increase in pilot workload and/or degradation in mission effectiveness. |
| Level 3 | Flying qualities such that the airplane can be controlled safely but the pilot workload is excessive and/or mission effectiveness is inadequate. |

**Rolling motion**

In this mode, only one degree of freedom is assumed: the rolling angle $\phi$. It corresponds to the largest fully real eigenvalue of A in absolute value.

Table 4.4: Lateral-Directional Handling Qualities: Roll mode. [22]

| Roll mode $-\ \tau_{max}$ (maximum time constant) | | | | |
|---|---|---|---|---|
| Class | Category | Level 1 | Level 2 | Level 3 |
| I and IV | A | 1.0 s | 1.4 s | 10 s |
| II and III | A | 1.4 s | 3.0 s | 10 s |
| All | B | 1.4 s | 3.0 s | 10 s |
| I and IV | C | 1.0 s | 1.4 s | 10 s |
| II and III | C | 1.4 s | 3.0 s | 10 s |

**Spiral stability**

It is the tendency to increase or decrease the angle of inclination of the wings after a disturbance (or lateral control), while keeping the control stick in the wing-level position without holding it. It is a non-oscillatory behaviour, that is, the aircraft is either closing or opening a curve, influenced by the characteristics of lateral and directional stability. The aircraft may have a divergent spiral (tendency to close the curve more and more) or convergent (the opposite).

The spiral motion corresponds to the smallest fully real eigenvalue in absolute value and is convergent if this eigenvalue is negative, or divergent if the corresponding eigenvalue is positive.

Table 4.5: Lateral-Directional Handling Qualities: Spiral mode. [22]

| Spiral mode $-\ T_{2,min}$ (minimum time to double) | | | | |
|---|---|---|---|---|
| Class | Category | Level 1 | Level 2 | Level 3 |
| I and IV | A | 12 s | 12 s | 4 s |
| | B and C | 20 s | 12 s | 4 s |
| II and III | All | 20 s | 12 s | 4 s |

**Dutch roll**

The Dutch roll is practically a swing that combines yaw and rolling. For some aircraft, this oscillation manifests itself primarily as sideslip and yaw, in which case the rolling momentum equation may be disregarded, hence the linear model may be simplified in this case. It corresponds to the conjugate complex eigenvalues of the state matrix A.

Table 4.6: Lateral-Directional Handling Qualities: Dutch Roll mode. [22]

| Dutch Roll mode | | | | | |
|---|---|---|---|---|---|
| Level | Category | Class | Frequency $\xi_{min}$ | $\xi \cdot \omega_{n_{min}}$ | Damping $\omega_{n_{min}}$ |
| 1 | A | I and IV | 0.19 | 0.35 rad/s | 1.0 rad/s |
| | | II and III | 0.19 | 0.35 rad/s | 0.4 rad/s |
| | B | All | 0.08 | 0.15rad/s | 0.4 rad/s |
| | C | I and IV | 0.08 | 0.15 rad/s | 1.0 rad/s |
| | | II and III | 0.08 | 0.15 rad/s | 0.4 rad/s |
| 2 | All | All | 0.02 | 0.05 rad/s | 0.4 rad/s |
| 3 | All | All | 0.02 | _ | 0.4 rad/s |

## 4.2 Case I - Conventional Aircraft Controller

Implementing the developed 6DoF trim model with the parameters found in Chapter 3.1.1, the corresponding trim lateral-directional state and control vectors are, respectively

$$x^*_{(case_I)} = \begin{bmatrix} 0 & 0 & 0 & 0 & 0 \end{bmatrix} \tag{4.44}$$

$$u^*_{(case_I)} = \begin{bmatrix} 0 & 0 \end{bmatrix} \tag{4.45}$$

Linearising the model around that point, the following lateral-directional matrices were obtained for the plant

$$A_{p_{(case_I)}} = \begin{bmatrix} -0.1278 & 9.7999 & 0 & 2.7004 & 59.7344 \\ 0 & 4.2776e-27 & 0 & 1 & 0.0366 \\ 0 & 1.1688e-25 & 0 & 0 & 1.0007 \\ -0.0839 & 0 & 0 & -4.6322 & 0.9396 \\ 0.0215 & 0 & 0 & -1.1825 & -0.9642 \end{bmatrix} \tag{4.46}$$

$$B_{p_{(case_I)}} = \begin{bmatrix} 2.7222 & 0.8574 \\ 0 & 0 \\ 0 & 0 \\ -7.7495 & -0.1550 \\ -0.8552 & 2.8888 \end{bmatrix} \tag{4.47}$$

In order to observe and control the desired states, the lateral-directional matrix $C_p$ was chosen to be

$$C_{p_{(case_I)}} = \begin{bmatrix} 0 & 1 & 0 & 0 & 0 \\ 0 & 0 & 1 & 0 & 0 \end{bmatrix} \tag{4.48}$$

Considering the previously deduced augmented system, it's possible to conclude that for the lateral-directional model

$$A_{(case_I)} = \begin{bmatrix} -0.1278 & 9.7999 & 0 & 2.7004 & 59.7344 & 0 & 0 \\ 0 & 4.2776e-27 & 0 & 1 & 0.0366 & 0 & 0 \\ 0 & 1.1688e-25 & 0 & 0 & 1.0007 & 0 & 0 \\ -0.0839 & 0 & 0 & -4.6322 & 0.9396 & 0 & 0 \\ 0.0215 & 0 & 0 & -1.1825 & -0.9642 & 0 & 0 \\ 0 & 1 & 0 & 0 & 0 & 0 & 0 \\ 0 & 0 & 1 & 0 & 0 & 0 & 0 \end{bmatrix} \tag{4.49}$$

$$B_{(case_I)} = \begin{bmatrix} 2.7222 & 0.8574 \\ 0 & 0 \\ 0 & 0 \\ -7.7495 & -0.1550 \\ -0.8552 & 2.8888 \\ 0 & 0 \\ 0 & 0 \end{bmatrix} \tag{4.50}$$

$$C_{(case_I)} = \begin{bmatrix} 0 & 1 & 0 & 0 & 0 & 0 & 0 \\ 0 & 0 & 1 & 0 & 0 & 0 & 0 \end{bmatrix} \tag{4.51}$$

$$E_{(case_I)} = \begin{bmatrix} 1 & 0 & 0 & 0 & 0 & 0 & 0 \\ 0 & 1 & 0 & 0 & 0 & 0 & 0 \\ 0 & 0 & 1 & 0 & 0 & 0 & 0 \\ 0 & 0 & 0 & 1 & 0 & 0 & 0 \\ 0 & 0 & 0 & 0 & 1 & 0 & 0 \\ 0 & 0 & 0 & 0 & 0 & 0 & 0 \\ 0 & 0 & 0 & 0 & 0 & 0 & 0 \end{bmatrix} \tag{4.52}$$

$$Br_{(case_I)} = \begin{bmatrix} 0 & 0 \\ 0 & 0 \\ 0 & 0 \\ 0 & 0 \\ 0 & 0 \\ -1 & 0 \\ 0 & -1 \end{bmatrix} \tag{4.53}$$

Based on these matrixes, it is possible to conclude that the system is controllable, as the controllability matrix $U$ has full rank of $n$, that is, $U$ has $n$ linearly independent columns.

After performing a static stability analysis, it was concluded that the aircraft is lateral-directionally statically stable as $C_{n_\beta} = 0.0135$ ($C_{n_\beta} > 0$) and $C_{l_\beta} = -0.0029$ ($C_{l_\beta} < 0$).

The eigenvalues in lateral-directional motions of the aircraft were determined according to Section 4.1.5 and are presented in Table 4.7.

Table 4.7: Eigenvalues in lateral-directional motions: Case I.

| Roll | Spiral | Dutch roll |
|---|---|---|
| $0.0528$ | $0.8731$ | $-3.3250 \pm 0.5360i$ |

Applying Tables' 4.5 to 4.6 constraints, it is possible to grade the aircraft's handling qualities according to the Cooper-Harper rating scale. The results are presented in Table 4.8.

Table 4.8: Lateral-directional handling qualities: Case I.

| Roll | Spiral | Dutch roll | | |
|---|---|---|---|---|
| $\tau_{max}$ | $T_{2,min}$ | $\xi_{min}$ | $\xi \cdot \omega_{n_{min}}$ | $\omega_{n_{min}}$ |
| s | s | – | rad/s | rad/s |
| Level 3+ | Level 3+ | Level 1 | Level 1 | Level 1 |

From Table 4.8 it is possible to see that stability-enhancing systems, means for grating appropriate flight qualities to an aircraft, are needed for this aircraft's Roll and Spiral modes. These systems are based on state feedback control concepts, and improve the stability and control of an aircraft that does not have desirable flight qualities.

### 4.2.1 Structure

A basic feedback loop structure (Figure 1.3), which allows the system to adapt its performance to meet the desired reference output response, was modified according with the employed augmented system from Equations 4.30 and 4.31. Thus, the feedback structure implemented to Case I is presented in Figure 4.5.
In this structure, the output error tracking is done inside the "Augmented Plant" subsystem and the designed control gain is applied to the current augmented plant states in the "Controller Gain" subsystem, by solving the respective control law and resulting in the new control actuation $u_{controller}$. The control $u$ input to the augmented plant is the subtraction of the control before the controller's implementation $u_0$ and the needed control computed by the controller $u_{controller}$ to track the reference output. Sensors and actuators lags and errors were not considered and both the gains design and control laws are described in the next subsection.

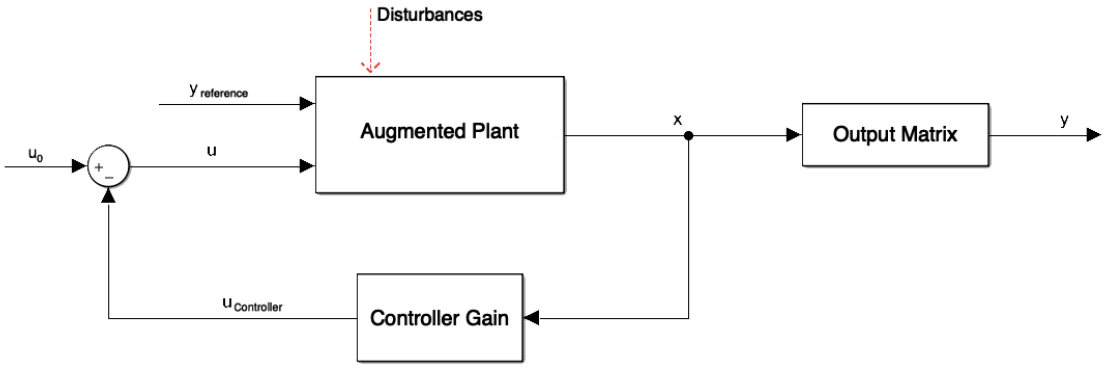


Figure 4.5: Feedback augmented plant structure.

### 4.2.2 Control law and gain design

The gain for both an $LQR$ and an $H_\infty$ controllers is designed and compared, in order to prove the $H_\infty$ controller robustness and validate the controller selection.

#### 4.2.2.1 $H_\infty$

In a typical $H_\infty$ control system design, the given specifications are at first transformed into a performance index, and then control laws which would minimize the $H_\infty$ norm of the performance index are sought. A given controller is said to be an $H_\infty$ optimal controller for a given system if, when the controller is applied to the system, the resulting closed-loop is internally stable and the $H_\infty$-norm of the closed-loop transfer matrix is equal to the infimum of the $H_\infty$-norm ($\gamma^*$). The class of controllers considered for both cases's system will be static linear-time-invariant state feedback, with a control law defined as follows [91]

$$u = -K \cdot x \tag{4.54}$$

where, $K \in \mathbb{R}^{m \times n}$ is the feedback gain matrix for the control system, such that the given performance specifications on the system are satisfactorily met. If $K = [K_1 \ K_2]$, the control law may also be written as

$$u = -K_1 \cdot x_p - K_2 \cdot x_e \tag{4.55}$$

The necessary and sufficient conditions so that a control law of the form given in Equation 4.54 exists are:

1. The state coefficient matrix $A$ and the driving matrix $B$ must be completely controllable;
2. The state coefficient matrix $A$ and the output matrix $C$ must be completely observable.

If the previous conditions are satisfied, then this feedback gain $K$ is given by[91]

$$K = \frac{R^{-1} \cdot B^T \cdot P}{2 \cdot \varepsilon} \tag{4.56}$$

where the symmetrical matrix $P \in \mathbb{R}^{n \times n}$ is the unique positive-definite solution of the control algebraic Riccati Equation 4.57[91], with attenuation constant $\gamma \neq \infty$ for some arbitrary $\varepsilon > 0$.

$$A^T P + PA - \frac{1}{\varepsilon} PBR^{-1}B^T P + \frac{1}{\gamma} PEE^T P + \frac{1}{\gamma} C^T C + \varepsilon Q = 0 \tag{4.57}$$

where $Q \in \mathbb{R}^{n \times n}$ is the state weighting matrix and $R \in \mathbb{R}^{m \times m}$ is the control weighting matrix, both symmetrical ($Q = Q^T$ and $R = R^T$), matrix $Q$ semi-definite ($Q \geq 0$) and matrix $R$ positive-definite ($R > 0$). These matrixes can be given in function of the maximum limits of each state and control input, respectively.

.

$$Q_{(i=j)} = \frac{1}{x^2_{(i=j)_{max}}}, \quad Q_{(i \neq j)} = 0, \quad R_{(i=j)} = \frac{1}{u^2_{(i=j)_{max}}}, \quad R_{(i \neq j)} = 0 \tag{4.58}$$

with $i$ and $j$ being the row and column, respectively. The author considers this method[92] to be a good starting point, choosing these matrixes based on the relative importance of the various states and controls. Further adjustments will be made to matrix Q to produce specified closed-loop eigenvalues, following Luo et al. proposed method[93]. The Hamiltonian structure $H \in \mathbb{R}^{2n \times 2n}$ of the algebraic Riccati Equation 4.57 is given by

$$H = \begin{bmatrix} -A & \frac{1}{\varepsilon} BR^{-1}B^T + \frac{1}{\gamma} EE^T \\ \frac{1}{\gamma} C^T C + \varepsilon Q & A^T \end{bmatrix} \tag{4.59}$$

The eigenvalues $\lambda$ of this matrix can be computed by solving the following equation

$$det(\lambda I - H) = 0 \tag{4.60}$$

The solution for that equation will be assigned as equal to the previously determined eigenvalues of the lateral-direction motion (Table 4.7), in order to connect those poles to the controller's feedback gains and account for more control effectiveness. While the non-diagonal values of Matrix Q remain null, the new diagonal values ($q_1, q_2, ..., q_n$) are given as the only unknown values of the previous equation so that

$$f(q_1, q_2, ..., q_n) = det(\lambda I - H) = 0 \tag{4.61}$$

In this work, an arbitrary $\varepsilon = 2$ will be chosen, as from experience the author considers that $\varepsilon < 1$ may saturate the actuators. The attenuation constant $\gamma$ that stabilises the augmented system is computed, in a first phase, as the lowest number on the power of ten series that solves the Riccati Equation 4.57 with $10^6$ precision factor. After the constant's magnitude is known, and if necessary, further adjustments can be made until the desired stability is achieved.

#### 4.2.2.2 LQR

This optimal controller aims to determine the system's optimal solutions, taking into account the minimisation of a quadratic error criterion. The control law is found by solving an optimisation problem that finds the control vector $u$ that minimizes the cost function $J$, given by [28]

$$J(u) = \int_0^\infty (x^T \cdot Q \cdot x + u^T \cdot R \cdot u)\, dt \tag{4.62}$$

The weighting matrices $Q$ and $R$ for this controller's gain design are the same as for the previous. Alike for the previous controller, they both need to be symmetrical ($Q = Q^T$ and $R = R^T$), matrix $Q$ semi-definite ($Q \geq 0$) and matrix $R$ positive-definite ($R > 0$).

The control vector to be parameterised and which minimizes the cost function in Equation 4.62, is a linear function of the state vector [28]

$$u = -K \cdot x \tag{4.63}$$

where, $K \in \mathbb{R}^{m \times n}$ is the optimal feedback gain matrix for the control system, such that the given performance specifications on the system are satisfactorily met. If $K = [K_1\ K_2]$, the control law may also be written as

$$u = -K_1 \cdot x_p - K_2 \cdot x_e \tag{4.64}$$

The necessary and sufficient conditions so that an optimal control law of the form given in Equation 4.63 exists are:

1. The state coefficient matrix $A$ and the driving matrix $B$ must be completely controllable;

2. The state coefficient matrix $A$ and the output matrix $C$ must be completely observable.

If the previous conditions are satisfied, then the optimal feedback gain $K$ is given by [28]

$$K = R^{-1} \cdot B^T \cdot P \tag{4.65}$$

where the symmetrical matrix $P \in \mathbb{R}^{n \times n}$ is the unique positive-definite solution of the control algebraic Riccati equation [91]

$$A^T P + PA - \frac{1}{\varepsilon} PBR^{-1}B^T P + \frac{1}{\gamma} PEE^T P + \frac{1}{\gamma} C^T C + \varepsilon Q = 0 \tag{4.66}$$

The Linear Quadratic Regulator is a particular case of the $H_\infty$, where $\gamma = \infty$ and $\varepsilon = 1$, so the control algebraic Riccati equation is simplified to

$$A^T P + PA - PBR^{-1}B^T P + Q = 0 \tag{4.67}$$

where the matrixes $Q$ and $R$ are in a first phase computed in function of the maximum limits of each state and control input, respectively, according to Equation 4.58. The matrix Q will suffer further adjustments to produce specified closed-loop eigenvalues, following Luo et al. proposed method [93]. The Hamiltonian structure $H \in \mathbb{R}^{2n \times 2n}$ of the algebraic Riccati Equation 4.67 is given by

$$H = \begin{bmatrix} -A & BR^{-1}B^T \\ Q & A^T \end{bmatrix} \tag{4.68}$$

The eigenvalues $\lambda$ of this matrix can be computed by solving Equation 4.60. The solution for that equation will be assigned as equal to the previously determined eigenvalues of the lateral-direction motion (Table 4.9), in order to connect those poles to the controller's feedback gains and account for more control effectiveness. While the non-diagonal values of Matrix Q remain null, the new diagonal values ($q_1, q_2, ..., q_n$) are given as the only unknown values of the previous equation so that Equation 4.31 is met.

#### 4.2.2.3 Gain Comparison

The previously described procedures to obtain the gains for a $H_\infty$ (Section 4.2.2.1) and $LQR$ (Section 4.2.2.2) controllers was implemented with Case I's parameters, and their response to an atmospheric disturbance is graphically compared below. From this comparison the most robust controller was identified and implemented on Case II.

The procedure from Section 4.2.2.1 was implemented and the resulting matrixes can be found below, from Equation 4.69 to 4.72.

The weighting matrixes were chosen as follows, by applying to Bryson's method [92] since Luo et al.'s method [93] proved too difficult to implement in this case

$$Q_{(case_I)} = \begin{bmatrix} 0.0004 & 0 & 0 & 0 & 0 & 0 & 0 \\ 0 & 0.4053 & 0 & 0 & 0 & 0 & 0 \\ 0 & 0 & 0.0253 & 0 & 0 & 0 & 0 \\ 0 & 0 & 0 & 1.6211 & 0 & 0 & 0 \\ 0 & 0 & 0 & 0 & 3.6476 & 0 & 0 \\ 0 & 0 & 0 & 0 & 0 & 1 & 0 \\ 0 & 0 & 0 & 0 & 0 & 0 & 1 \end{bmatrix} \tag{4.69}$$

$$R_{(case_I)} = \begin{bmatrix} 8.2070 & 0 \\ 0 & 4.8562 \end{bmatrix} \tag{4.70}$$

The unique positive-definite solution of the control alebraic Riccati Equation 4.57, with attenuation constant $\gamma = 1000000$ and $\varepsilon = 6$, is

$$P_{H_{\infty(case_I)}} = \begin{bmatrix} 0.0054 & -0.0314 & -0.2778 & -0.0091 & 0.0200 & -0.0433 & -0.0296 \\ -0.0314 & 5.4443 & 0.1857 & 0.8068 & 0.0566 & 2.5895 & -0.1130 \\ -0.2778 & 0.1857 & 27.0927 & -0.4658 & 2.5198 & 2.3081 & 5.2269 \\ -0.0091 & 0.8068 & -0.4658 & 0.3291 & -0.2914 & 0.3409 & -0.1308 \\ 0.0200 & 0.0566 & 2.5198 & -0.2914 & 1.9552 & 0.1064 & 0.7609 \\ -0.0433 & 2.5895 & 2.3081 & 0.3409 & 0.1064 & 2.6435 & 0.0756 \\ -0.0296 & -0.1130 & 5.2269 & -0.1308 & 0.7609 & 0.0756 & 3.2363 \end{bmatrix} \tag{4.71}$$

Finally, computing Equation 4.56, the optimal gain was found to be

$$K_{H_{\infty(case_I)}} = \begin{bmatrix} -0.0083 & 0.7781 & -0.0851 & 0.2834 & -0.0780 & 0.3474 & -0.0344 \\ -0.0131 & -0.0023 & -1.4648 & 0.1854 & -1.1759 & -0.0447 & -0.4516 \end{bmatrix} \tag{4.72}$$

The procedure from Section 4.2.2.2 was also implemented and the resulting matrixes can be found below, from Equation 4.73 to 4.74.

The weighting matrixes on Equations 4.69 and 4.70 also apply for this controller.

The unique positive-definite solution of the control algebraic Riccati Equation 4.57, with attenuation constant $\gamma = \infty$ and $\varepsilon = 1$, is

$$P_{LQR_{(case_I)}} = \begin{bmatrix} 0.0325 & -0.1885 & -1.6674 & -0.0545 & 0.1199 & -0.2602 & -0.1777 \\ -0.1885 & 32.6667 & 1.1165 & 4.8407 & 0.3394 & 15.5379 & -0.6781 \\ -1.6674 & 1.1165162.6189 & -2.7956 & 15.1228 & 13.8568 & 31.3635 & \\ -0.0545 & 4.8407 & -2.7956 & 1.9745 & -1.7484 & 2.0454 & -0.7850 \\ 0.1199 & 0.3394 & 15.1228 & -1.7484 & 11.7315 & 0.6386 & 4.5657 \\ -0.2602 & 15.5379 & 13.8568 & 2.0454 & 0.6386 & 15.8624 & 0.4533 \\ -0.1777 & -0.6781 & 31.3635 & -0.7850 & 4.5657 & 0.4533 & 19.4188 \end{bmatrix} \tag{4.73}$$

Finally, computing Equation 4.56, the optimal gain was found to be

$$K_{LQR_{(case_I)}} = \begin{bmatrix} -0.0041 & 0.3891 & -0.0426 & 0.1417 & -0.0390 & 0.1737 & -0.0172 \\ -0.0066 & -0.0012 & -0.7326 & 0.0927 & -0.5880 & -0.0224 & -0.2258 \end{bmatrix} \tag{4.74}$$

For comparing the two controllers, two simulations of a commanded roll angle of around 2 degrees and a turn rate of 15 degrees per minute. In the second simulation the aircraft encounters atmospheric disturbances, while there are no disturbances in the first.

The magnitude of the disturbance was assumed considering the disturbance vector's variables $d_v$, $d_\phi$, $d_\psi$, $d_p$ and $d_r$ random gaussian variables with null average and standard deviations as follows

$$d_v \sim N(0, \sigma_v^2), \quad with \;\; \sigma_v \in \left[0, \frac{5}{3}\right] \tag{4.75}$$

$$d_\phi \sim N(0, \sigma_\phi^2), \quad with \;\; \sigma_\phi \in \left[0, \frac{0.035}{3}\right] \tag{4.76}$$

$$d_\psi \sim N(0, \sigma_\psi^2), \quad with \;\; \sigma_\psi \in \left[0, \frac{0.035}{3}\right] \tag{4.77}$$

$$d_p \sim N(0, \sigma_p^2), \quad with \;\; \sigma_p \in \left[0, \frac{0.087}{3}\right] \tag{4.78}$$

$$d_r \sim N(0, \sigma_r^2), \quad with \;\; \sigma_r \in \left[0, \frac{0.087}{3}\right] \tag{4.79}$$

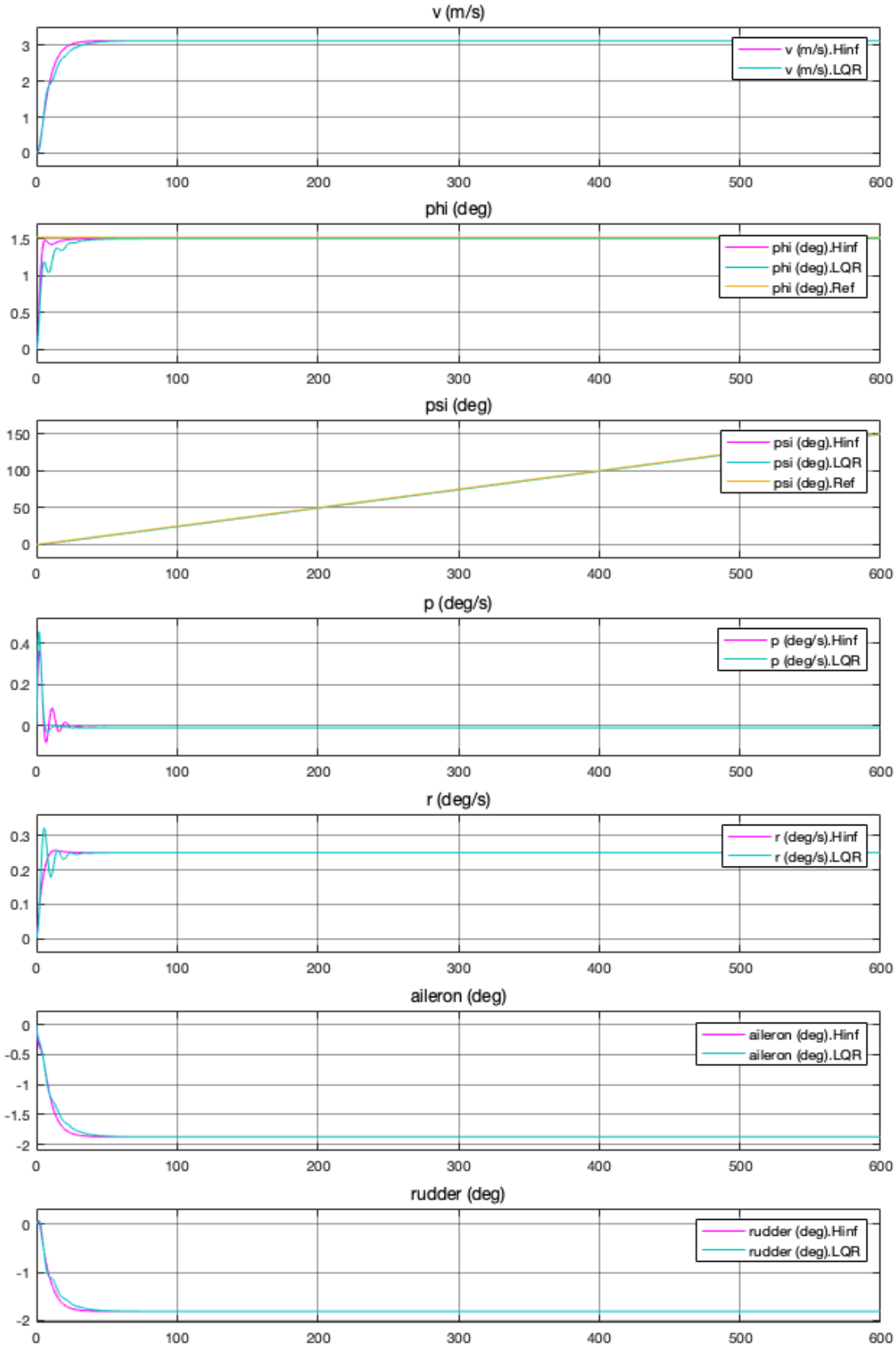


Figure 4.6: Simulation 1 results - Response without disturbance.

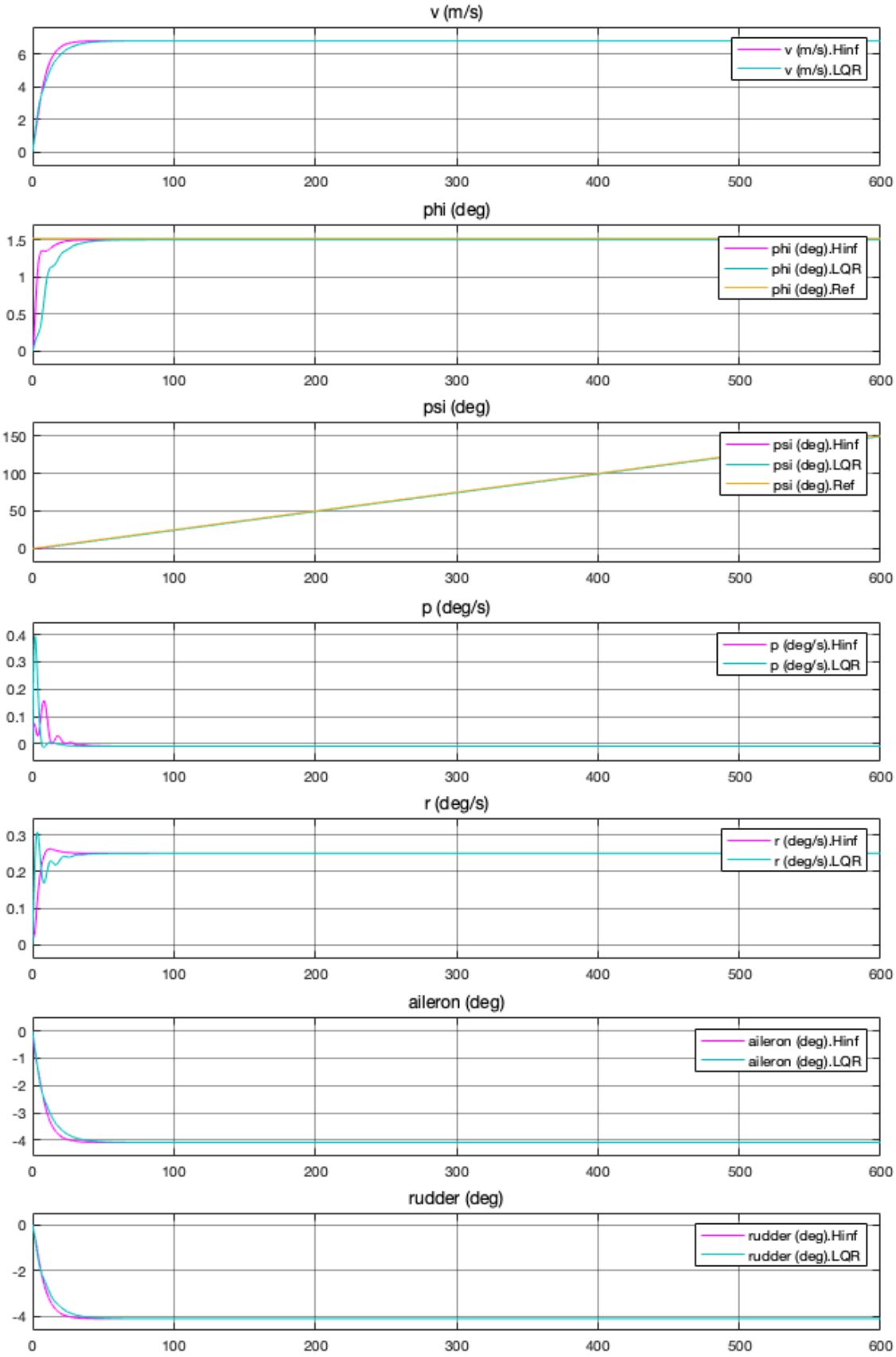


Figure 4.7: Simulation 2 results - Response to a random disturbance.

From Figures 4.6 and 4.7 is possible to compare the response of both controllers to atmospheric disturbances. Analysing both graphics it is evident that the $H_\infty$ controller performs better in the face of disturbances, settling in the desired values in slightly less time than the $LQR$ controller and with a lower peak overshoot than for the $LQR$ controller.
Comparing Figure 4.6 to Figure 4.7 it is also clear that the bigger the disturbance the bigger the difference between both controllers' peak overshoot, while the settling time doesn't vary much. In the case of aircrafts, a lower peak overshoot is more important than a slight increase in the settling time, so the $H_\infty$ controller was identified as the most robust in the face of disturbances, and therefore the most appropriate to be implemented on Case II, in order to further compare the manoeuvrability between both cases.

## 4.3 Case II - Propulsion Aircraft Controller

Implementing the developed 6DoF trim model with the parameters found in Chapter 3.2.3, the corresponding trim lateral-directional state and control vectors are, respectively

$$x^*_{(case_{II})} = \begin{bmatrix} 0 & 0 & 0 & 0 & 0 \end{bmatrix} \tag{4.80}$$

$$u^*_{(case_{II})} = \begin{bmatrix} 0 & 0 & 0.53 & 0.53 & 0.53 & 0.53 & 0.53 & 0.53 & 0.53 & 0.53 & 0.53 & 0.53 & 0.53 & 0.53 \end{bmatrix} \tag{4.81}$$

Linearising the model around that point, the following lateral-directional matrices were obtained for the plant

$$A_{p_{(case_{II})}} = \begin{bmatrix} -0.0515 & 9.7999 & 0 & 2.7437 & 59.5517 \\ 0 & -5.5259e-27 & 0 & 1.0000 & 0.0367 \\ 0 & -1.5083e-25 & 0 & 0 & 1.0007 \\ -0.0787 & 0 & 0 & -4.3176 & 0.7583 \\ 0.0054 & 0 & 0 & -1.1320 & -0.9197 \end{bmatrix} \tag{4.82}$$

$$B_{p_{(case_{II})}} = \begin{bmatrix} 2.7222 & -0.4930 & 0 & 0 & 0 & 0 & 0 \\ 0 & 0 & 0 & 0 & 0 & 0 & 0 \\ 0 & 0 & 0 & 0 & 0 & 0 & 0 \\ -7.2750 & 0.0970 & 0.0265 & 0.0293 & 0.0294 & 0.0231 & 0.0157 \\ -0.8315 & -1.5152 & -0.2697 & -0.2255 & -0.1813 & -0.1371 & -0.0929 \\ 0 & 0 & 0 & 0 & 0 & 0 & 0 \\ 0 & 0 & 0 & 0 & 0 & 0 & 0 \\ 0 & 0 & 0 & 0 & 0 & 0 & 0 \\ 0.0082 & -0.0082 & -0.0157 & -0.0231 & -0.0294 & -0.0293 & -0.0265 \\ -0.0487 & 0.0487 & 0.0929 & 0.1371 & 0.1813 & 0.2255 & 0.2697 \end{bmatrix} \tag{4.83}$$

In order to observe and control the desired states, the lateral-directional matrix $C_p$ was chosen to be

$$C_{p_{(case_{II})}} = \begin{bmatrix} 0 & 1 & 0 & 0 & 0 \\ 0 & 0 & 1 & 0 & 0 \end{bmatrix} \tag{4.84}$$

Considering the previously deduced augmented system, it's possible to conclude that for the lateral-directional model

$$A_{(case_{II})} = \begin{bmatrix} -0.0515 & 9.7999 & 0 & 2.7437 & 59.5517 & 0 & 0 \\ 0 & -5.5259e-27 & 0 & 1.0000 & 0.0367 & 0 & 0 \\ 0 & -1.5083e-25 & 0 & 0 & 1.0007 & 0 & 0 \\ -0.0787 & 0 & 0 & -4.3176 & 0.7583 & 0 & 0 \\ 0.0054 & 0 & 0 & -1.1320 & -0.9197 & 0 & 0 \\ 0 & 1 & 0 & 0 & 0 & 0 & 0 \\ 0 & 0 & 1 & 0 & 0 & 0 & 0 \end{bmatrix} \tag{4.85}$$

$$B_{p_{(case_{II})}} = \begin{bmatrix} 2.7222 & -0.4930 & 0 & 0 & 0 & 0 & 0 \\ 0 & 0 & 0 & 0 & 0 & 0 & 0 \\ 0 & 0 & 0 & 0 & 0 & 0 & 0 \\ -7.2750 & 0.0970 & 0.0265 & 0.0293 & 0.0294 & 0.0231 & 0.0157 \\ -0.8315 & -1.5152 & -0.2697 & -0.2255 & -0.1813 & -0.1371 & -0.0929 \\ 0 & 0 & 0 & 0 & 0 & 0 & 0 \\ 0 & 0 & 0 & 0 & 0 & 0 & 0 \end{bmatrix}$$

$$\begin{bmatrix} 0 & 0 & 0 & 0 & 0 & 0 & 0 \\ 0 & 0 & 0 & 0 & 0 & 0 & 0 \\ 0 & 0 & 0 & 0 & 0 & 0 & 0 \\ 0.0082 & -0.0082 & -0.0157 & -0.0231 & -0.0294 & -0.0293 & -0.0265 \\ -0.0487 & 0.0487 & 0.0929 & 0.1371 & 0.1813 & 0.2255 & 0.2697 \\ 0 & 0 & 0 & 0 & 0 & 0 & 0 \\ 0 & 0 & 0 & 0 & 0 & 0 & 0 \end{bmatrix} \tag{4.86}$$

$$C_{(case_{II})} = \begin{bmatrix} 0 & 1 & 0 & 0 & 0 & 0 & 0 \\ 0 & 0 & 1 & 0 & 0 & 0 & 0 \end{bmatrix} \tag{4.87}$$

$$E_{(case_I)} = \begin{bmatrix} 1 & 0 & 0 & 0 & 0 & 0 & 0 \\ 0 & 1 & 0 & 0 & 0 & 0 & 0 \\ 0 & 0 & 1 & 0 & 0 & 0 & 0 \\ 0 & 0 & 0 & 1 & 0 & 0 & 0 \\ 0 & 0 & 0 & 0 & 1 & 0 & 0 \\ 0 & 0 & 0 & 0 & 0 & 0 & 0 \\ 0 & 0 & 0 & 0 & 0 & 0 & 0 \end{bmatrix} \tag{4.88}$$

$$Br_{(case_I)} = \begin{bmatrix} 0 & 0 \\ 0 & 0 \\ 0 & 0 \\ 0 & 0 \\ 0 & 0 \\ -1 & 0 \\ 0 & -1 \end{bmatrix} \tag{4.89}$$

Based on these matrixes, it is possible to conclude that the system is controllable, as the con-

trollability matrix $U$ has full rank of $n$, that is, $U$ has $n$ linearly independent columns.
After performing a static stability analysis, it was concluded that the aircraft is lateral-directionally statically stable as $C_{n_\beta} = 0.0035$ ($C_{n_\beta} > 0$) and $C_{l_\beta} = -0.0019$ ($C_{l_\beta} < 0$).
The eigenvalues in lateral-directional motions of the aircraft were determined according to Section 4.1.5 and are presented in Table 4.9.

Table 4.9: Eigenvalues in lateral-directional motions: Case II.

| Roll | Spiral | Dutch roll |
|---|---|---|
| $0.1327$ | $0.5334$ | $-2.9774 \pm 0.1491i$ |

Applying Tables' 4.5 to 4.6 constraints, it is possible to grade the aircraft's handling qualities according to the. Cooper-Harper rating scale. The results are presented in Table 4.10.

Table 4.10: Lateral-directional handling qualities: Case II.

| Roll | Spiral | Dutch roll | | |
|---|---|---|---|---|
| $\tau_{max}$ | $T_{2,min}$ | $\xi_{min}$ | $\xi \cdot \omega_{n_{min}}$ | $\omega_{n_{min}}$ |
| s | s | – | rad/s | rad/s |
| Level 3 | Level 3+ | Level 1 | Level 1 | Level 1 |

From Table 4.10 it is possible to see that stability-enhancing systems, means for grating appropriate flight qualities to an aircraft, are needed for this aircraft's Spiral mode. These systems are based on state feedback control concepts, and improve the stability and control of an aircraft that does not have desirable flight qualities.

### 4.3.1 Structure

An algorithm was developed so that the hybrid systems alternates from the conventional control to the propulsion control automatically and according to the plant's current proprieties. The designed algorithm manages the controller's behaviour as follows:

1. The thrust excess in each engine is computed, so that the available thrust for differential propulsion usage is known.

2. Maintaining flight speed and altitude(without reducing the inicial throttle), additional thrust is introduced on the engines located on opposite side of the intended turn.

3. That extra thrust is increased in a loop until the engine reaches its maximum thrust or the turn is complete, whichever comes first.

4. If the engine reaches its maximum thrust before the desired turn is attained, the rudder is activated and completes the commanded maneuver.

This hybrid controller also detects if a different control command has been made before the aircraft reaches the previous one. In that case, the system re-implements the algorithm, trying to perform the maneuver with the propulsive system first. The controller allows the user to define the settling tolerance magnitude, within which the system assumes the maneuver is complete, and the maximum settling time, from which the system switches to the conventional mode in case the desired turn has not been reached.

The same basic feedback loop structure from 1.3 was modified according with the employed augmented system from Equations 4.30 and 4.31. Thus, the feedback structure implemented to Case II is presented in Figure 4.8.

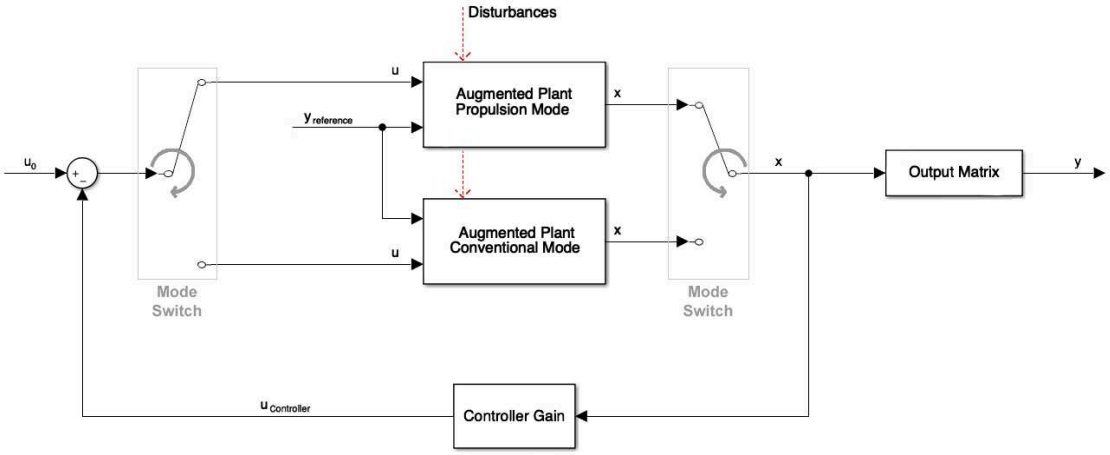


Figure 4.8: Feedback augmented plant structure.

In this structure, the output error tracking is once again done inside each mode's "Augmented Plant" subsystem and the designed control gain is applied to the current augmented plant states in the "Controller Gain" subsystem, by solving the respective control law and resulting in the new control actuation. The control $u$ input to the augmented plant is the subtraction of the control before the controller's implementation $u_0$ and the needed control computed by the controller $u_{controller}$ to track the reference output. There are also two interrelated automatic "Mode Switches", that swap up for the propulsion mode and down for the conventional mode according to the previously described algorithm. Sensors and actuators lags and errors were not considered and both the gains design and control laws are described in the next subsection.

Maximum allowable bank angle was set according to the load factor ($n$) limitations as follows,

$$n = \frac{1}{cos(\phi)} \quad \Rightarrow \quad \phi_{max} = cos^{-1}\left(\frac{1}{n_{max}}\right) \tag{4.90}$$

### 4.3.2 Control law and gain design

For this case, the gain will be designed for a $H_\infty$ controller, as proven in Chapter 4.2.2.3 to be the most robust. The procedure from Section 4.2.2.1 was implemented and the resulting matrixes can be found below for both modes, from Equation 4.91 to 4.96.

For both modes, the weighting matrixes were chosen to be

$$Q_{(case_I I)} = \begin{bmatrix} 0.0004 & 0 & 0 & 0 & 0 & 0 & 0 \\ 0 & 0.4053 & 0 & 0 & 0 & 0 & 0 \\ 0 & 0 & 0.0253 & 0 & 0 & 0 & 0 \\ 0 & 0 & 0 & 1.6211 & 0 & 0 & 0 \\ 0 & 0 & 0 & 0 & 3.6476 & 0 & 0 \\ 0 & 0 & 0 & 0 & 0 & 1 & 0 \\ 0 & 0 & 0 & 0 & 0 & 0 & 1 \end{bmatrix} \tag{4.91}$$

$$R_{(case_{II})} = \begin{bmatrix} 8.2070 & 0 & 0 & 0 & 0 & 0 & 0 & 0 & 0 & 0 & 0 & 0 & 0 & 0 \\ 0 & 4.8562 & 0 & 0 & 0 & 0 & 0 & 0 & 0 & 0 & 0 & 0 & 0 & 0 \\ 0 & 0 & 1 & 0 & 0 & 0 & 0 & 0 & 0 & 0 & 0 & 0 & 0 & 0 \\ 0 & 0 & 0 & 1 & 0 & 0 & 0 & 0 & 0 & 0 & 0 & 0 & 0 & 0 \\ 0 & 0 & 0 & 0 & 1 & 0 & 0 & 0 & 0 & 0 & 0 & 0 & 0 & 0 \\ 0 & 0 & 0 & 0 & 0 & 1 & 0 & 0 & 0 & 0 & 0 & 0 & 0 & 0 \\ 0 & 0 & 0 & 0 & 0 & 0 & 1 & 0 & 0 & 0 & 0 & 0 & 0 & 0 \\ 0 & 0 & 0 & 0 & 0 & 0 & 0 & 1 & 0 & 0 & 0 & 0 & 0 & 0 \\ 0 & 0 & 0 & 0 & 0 & 0 & 0 & 0 & 1 & 0 & 0 & 0 & 0 & 0 \\ 0 & 0 & 0 & 0 & 0 & 0 & 0 & 0 & 0 & 1 & 0 & 0 & 0 & 0 \\ 0 & 0 & 0 & 0 & 0 & 0 & 0 & 0 & 0 & 0 & 1 & 0 & 0 & 0 \\ 0 & 0 & 0 & 0 & 0 & 0 & 0 & 0 & 0 & 0 & 0 & 1 & 0 & 0 \\ 0 & 0 & 0 & 0 & 0 & 0 & 0 & 0 & 0 & 0 & 0 & 0 & 1 & 0 \\ 0 & 0 & 0 & 0 & 0 & 0 & 0 & 0 & 0 & 0 & 0 & 0 & 0 & 1 \end{bmatrix} \tag{4.92}$$

**Propulsion mode**

For this mode, the rudder contributions to the aircraft's motion were not considered in order to use propulsion only for directional control, this was achieved by setting the second column of the driving matrix $B_{(case_{II})}$ to zero. The unique positive-definite solution of the control algebraic Riccati Equation 4.57, with attenuation constant $\gamma = 1000000$ and $\varepsilon = 6$, is

$$P_{H_{\infty(case_{II})}} = \begin{bmatrix} 0.0112 & -0.0219 & -0.6004 & -0.0103 & 0.0447 & -0.0940 & -0.0358 \\ -0.0219 & 6.1766 & 0.7549 & 0.7924 & 0.9256 & 2.7871 & -0.1684 \\ -0.6004 & 0.7549 & 52.3283 & -1.2043 & 5.8172 & 6.0443 & 6.9533 \\ -0.0103 & 0.7924 & -1.2043 & 0.4421 & -0.7730 & 0.2892 & -0.2956 \\ 0.0447 & 0.9256 & 5.8172 & -0.7730 & 5.0587 & 0.4795 & 1.5393 \\ -0.0940 & 2.7871 & 6.0443 & 0.2892 & 0.4795 & 3.2729 & 0.2140 \\ -0.0358 & -0.1684 & 6.9533 & -0.2956 & 1.5393 & 0.2140 & 3.7264 \end{bmatrix} \tag{4.93}$$

Finally, computing Equation 4.56, the optimal gain was found to be

$$K_{H_{\infty(case_{II})}} = \begin{bmatrix} -0.0083 & 0.8034 & -0.2790 & 0.3170 & -0.1875 & 0.3361 & -0.0942 \\ 0 & 0 & 0 & 0 & 0 & 0 & 0 \\ 0.0123 & 0.2287 & 1.6011 & -0.2202 & 1.3851 & 0.1217 & 0.4230 \\ 0.0104 & 0.1855 & 1.3472 & -0.1873 & 1.1635 & 0.0997 & 0.3558 \\ 0.0084 & 0.1445 & 1.0902 & -0.1532 & 0.9400 & 0.0784 & 0.2878 \\ 0.0064 & 0.1086 & 0.8253 & -0.1162 & 0.7114 & 0.0590 & 0.2179 \\ 0.0043 & 0.0736 & 0.5591 & -0.0787 & 0.4819 & 0.0400 & 0.1476 \\ 0.0023 & 0.0385 & 0.2929 & -0.0412 & 0.2525 & 0.0210 & 0.0773 \\ -0.0023 & -0.0385 & -0.2929 & 0.0412 & -0.2525 & -0.0210 & -0.0773 \\ -0.0043 & -0.0736 & -0.5591 & 0.0787 & -0.4819 & -0.0400 & -0.1476 \\ -0.0064 & -0.1086 & -0.8253 & 0.1162 & -0.7114 & -0.0590 & -0.2179 \\ -0.0084 & -0.1445 & -1.0902 & 0.1532 & -0.9400 & -0.0784 & -0.2878 \\ -0.0104 & -0.1855 & -1.3472 & 0.1873 & -1.1635 & -0.0997 & -0.3558 \\ -0.0123 & -0.2287 & -1.6011 & 0.2202 & -1.3851 & -0.1217 & -0.4230 \end{bmatrix} \tag{4.94}$$

**Conventional mode**

For this mode, the propulsive contributions to the aircraft's motion were not considered, this was achieved by setting the third to last columns of the driving matrix $B_{(case_I I)}$ to zero. The unique positive-definite solution of the control algebraic Riccati Equation 4.57, with same attenuation and tuning constants, is

$$P_{H_{\infty(case_{II})}} = \begin{bmatrix} 0.0100 & -0.0289 & -0.5456 & -0.0096 & 0.0331 & -0.0847 & -0.0346 \\ -0.0289 & 5.9553 & 0.7334 & 0.8169 & 0.6165 & 2.7550 & -0.1491 \\ -0.5456 & 0.7334 & 47.7811 & -1.0812 & 5.2991 & 5.2848 & 6.5937 \\ -0.0096 & 0.8169 & -1.0812 & 0.4278 & -0.6791 & 0.3064 & -0.2667 \\ 0.0331 & 0.6165 & 5.2991 & -0.6791 & 4.3133 & 0.3901 & 1.4076 \\ -0.0847 & 2.7550 & 5.2848 & 0.3064 & 0.3901 & 3.1368 & 0.1717 \\ -0.0346 & -0.1491 & 6.5937 & -0.2667 & 1.4076 & 0.1717 & 3.6309 \end{bmatrix} \tag{4.95}$$

Finally, computing Equation 4.56, the optimal gain was found to be

$$K_{H_{\infty(case_{II})}} = \begin{bmatrix} -0.0085 & 0.7962 & -0.2406 & 0.3136 & -0.1759 & 0.3392 & -0.0823 \\ -0.0115 & -0.1731 & -1.6196 & 0.2214 & -1.3627 & -0.1070 & -0.4410 \\ 0 & 0 & 0 & 0 & 0 & 0 & 0 \\ 0 & 0 & 0 & 0 & 0 & 0 & 0 \\ 0 & 0 & 0 & 0 & 0 & 0 & 0 \\ 0 & 0 & 0 & 0 & 0 & 0 & 0 \\ 0 & 0 & 0 & 0 & 0 & 0 & 0 \\ 0 & 0 & 0 & 0 & 0 & 0 & 0 \\ 0 & 0 & 0 & 0 & 0 & 0 & 0 \\ 0 & 0 & 0 & 0 & 0 & 0 & 0 \\ 0 & 0 & 0 & 0 & 0 & 0 & 0 \\ 0 & 0 & 0 & 0 & 0 & 0 & 0 \\ 0 & 0 & 0 & 0 & 0 & 0 & 0 \\ 0 & 0 & 0 & 0 & 0 & 0 & 0 \end{bmatrix} \tag{4.96}$$

# Chapter 5

# Simulation and Results

A program for trajectory visualisation was created using Matlab[1] for the Geodetic referential with the following set of governing equations

$$\dot{\bar{h}} = V \cdot sin(\bar{\gamma}) \tag{5.1}$$

$$\dot{\bar{\lambda}} = \frac{V \cdot cos(\bar{\gamma}) \cdot sin(\chi)}{\bar{h} \cdot cos(\varphi)} \tag{5.2}$$

$$\dot{\varphi} = \frac{V \cdot cos(\bar{\gamma}) \cdot sin(\chi)}{\bar{h}} \tag{5.3}$$

where,
$\bar{h}$ is the distance from the centre Earth's globe to the aircraft.
$\bar{\lambda}$ is the aircraft's longitude.
$\varphi$ is the aircraft's latitude.
$\bar{\gamma}$ is the aircraft's trajectory in relation to the horizontal local plane.
$\chi$ is the aircraft's flight path angle in relation to geodetic North.

In this Section's simulations, all trajectories' starting point is in Lisbon (Portugal) with the following coordinates:

- Latitude — 38° 43' 0.01" North
- Longitude — -9° 07' 59.99" West

Two simulations were tested for the designed controller, a coordinated turn and the critical engine failure. Conclusions on the manoeuvrability of the achieved control on Case II will be taken based on a comparison with the conventional controller from Case I and the conventional mode of the same configuration. It is assumed that the initial conditions of the system state at time $t = 0$ are $x^*$ and $u^*$, for Mach $0.18$ and a $2450\ m$ altitude.

## 5.1 Coordinated turn simulation

When the aircraft is flying in a steady level coordinated turn with a speed $V$ and bank angle $\phi$, by resolving the forces acting on the aircraft vertically and horizontally (shown in Figure 5.1) and eliminating the lift L between the two resulting equations it is easily shown that the radius of turn is given by [23]

$$R_{turn} = \frac{V^2}{g \cdot tan(\phi)} \tag{5.4}$$

[1] MATLAB R2018a, The MathWorks Inc.

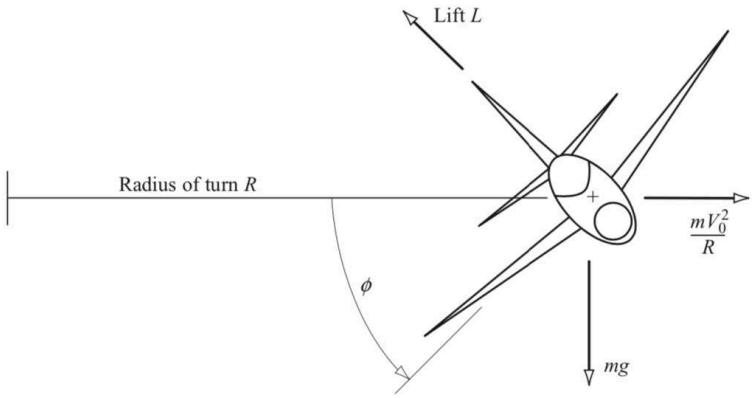


Figure 5.1: Aircraft in a steady banked turn. [23]

The time to complete one turn is given by

$$t_{turn} = \frac{2\pi \cdot \bar{h}}{V} = \frac{2\pi \cdot V}{g \cdot tan(\phi)} \tag{5.5}$$

Therefore the rate of turn is given by

$$\dot{\psi} = \frac{2\pi}{t_{turn}} = \frac{g \cdot tan(\phi)}{V} \tag{5.6}$$

During a coordinated turn, the following conditions apply

$$\dot{\phi} = \dot{\theta} = \theta = 0 \tag{5.7}$$

The coordinated turn will be tracked until the error ($\varepsilon_{turn}$) is null, i.e. the following equation equals zero.

$$\varepsilon_{turn} = \dot{\psi} - \frac{g \cdot tan(\phi)}{V} \tag{5.8}$$

The parameters, matrixes, control gains and structure for this simulation can be found on the previous section. Trim conditions were used as initial values.

First, represented on Figure 5.2, a simulation of the Conventional aircraft (case I) will be made at $\dot{\psi} = 30°/min$ for reference and future comparison, besides Figure 4.6, also for Mach $0.18$ and a $2450\ m$ altitude.
While maintaining Mach $0.18$ and a $2450\ m$ altitude (as no longitudinal model was developed, this is assured by maintaining $\delta_{th} \geq \delta_{th}^*$), different rates of turn will be simulated for the DEP configuration(case II):

- $\dot{\psi} = 5°/min$ – Figures 5.3 and 5.4
- $\dot{\psi} = 15°/min$ – Figures 5.5 and 5.6
- $\dot{\psi} = 30°/min$ – Figures 5.7 and 5.8
- $\dot{\psi} = 45°/min$ – Figures 5.9 and 5.10
- $\dot{\psi} = 55°/min$ – Figures 5.11 and 5.12

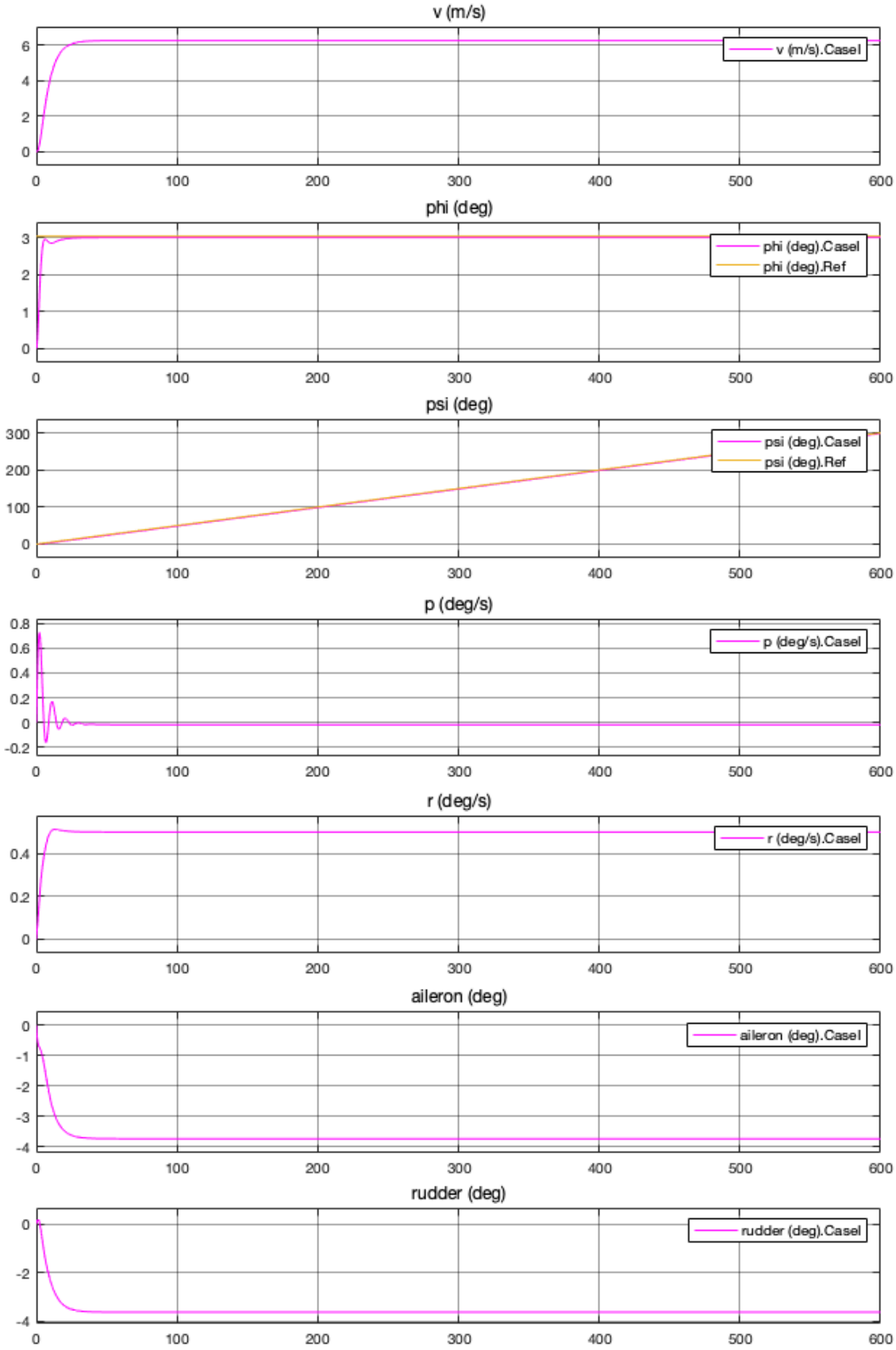


Figure 5.2: Simulation $\dot{\psi} = 30°/min$ results for Case I.

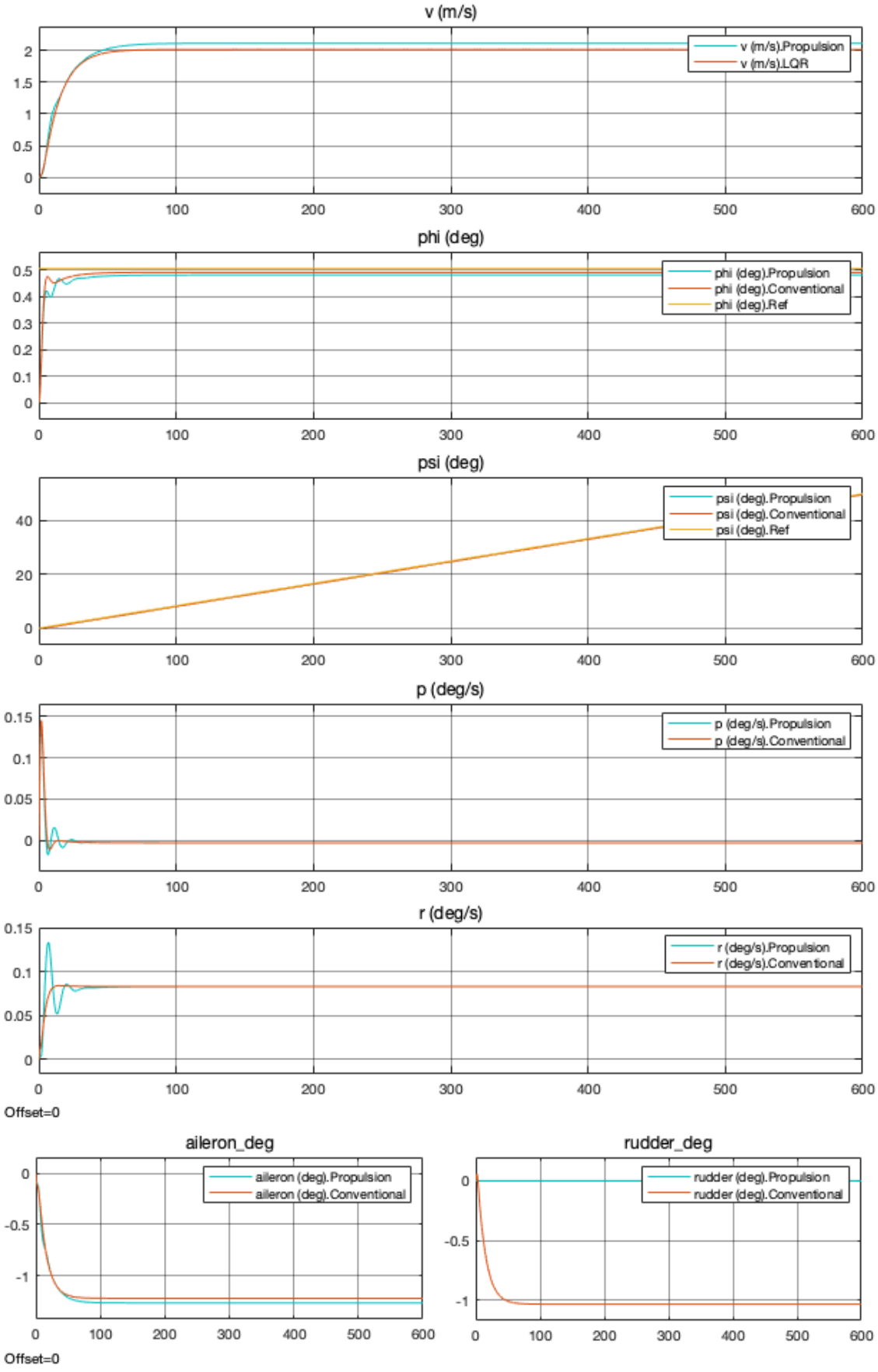


Figure 5.3: Simulation $\dot{\psi} = 5°/min$ DEP results - States and Conventional Controls.

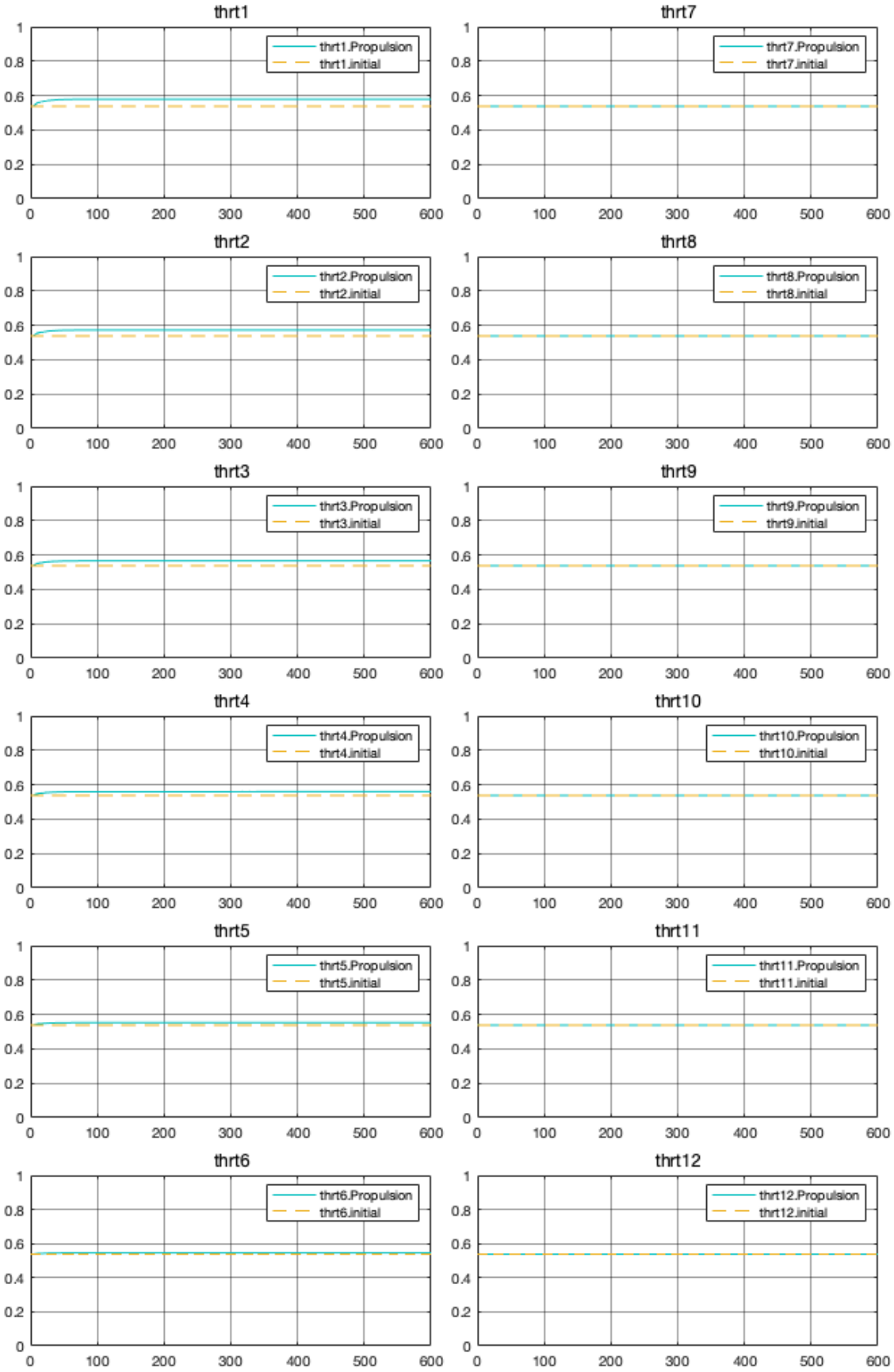


Figure 5.4: Simulation $\dot{\psi} = 5°/min$ DEP results - Propulsive Controls.

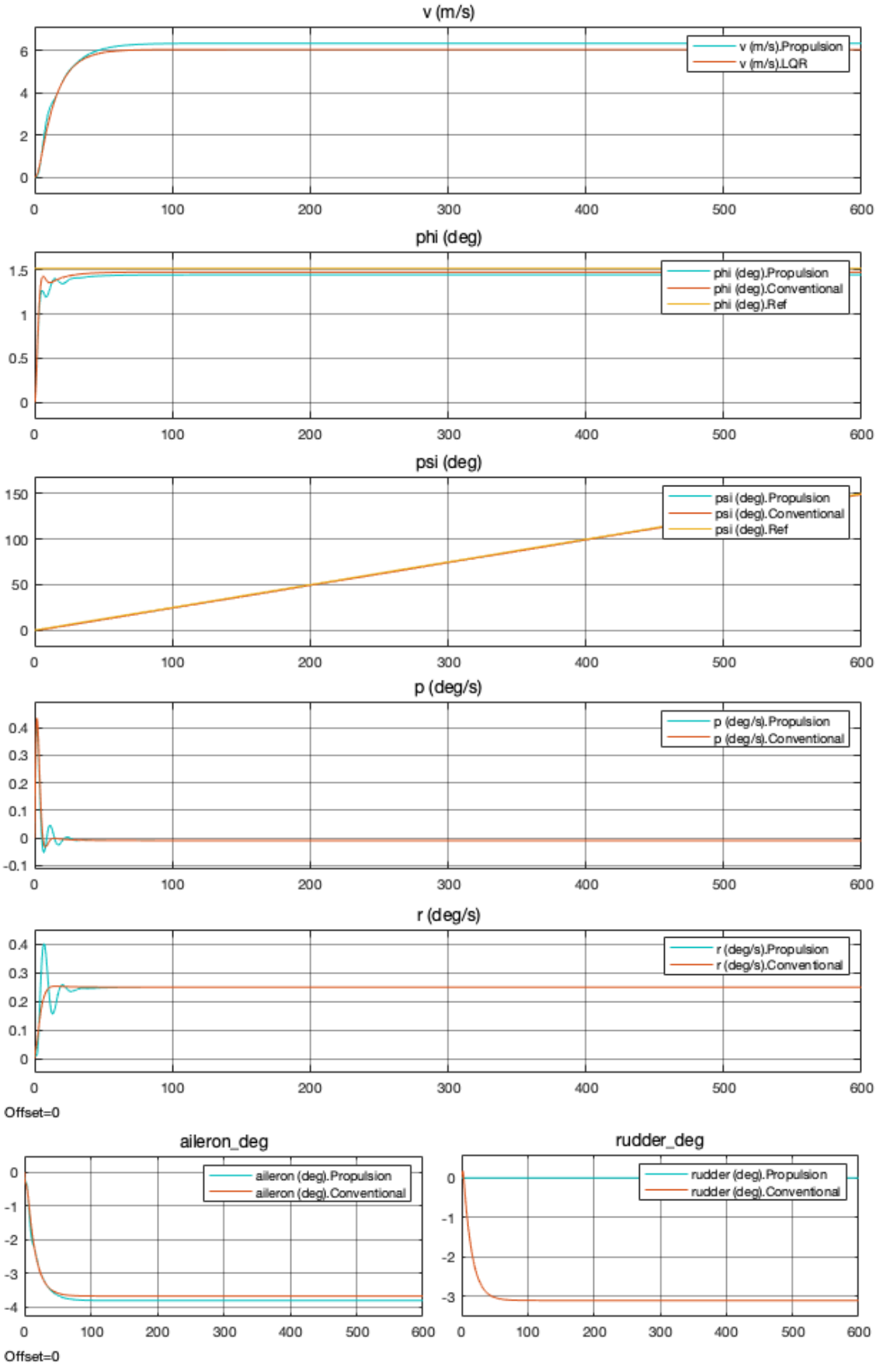


Figure 5.5: Simulation $\dot{\psi} = 15°/min$ DEP results - States and Conventional Controls.

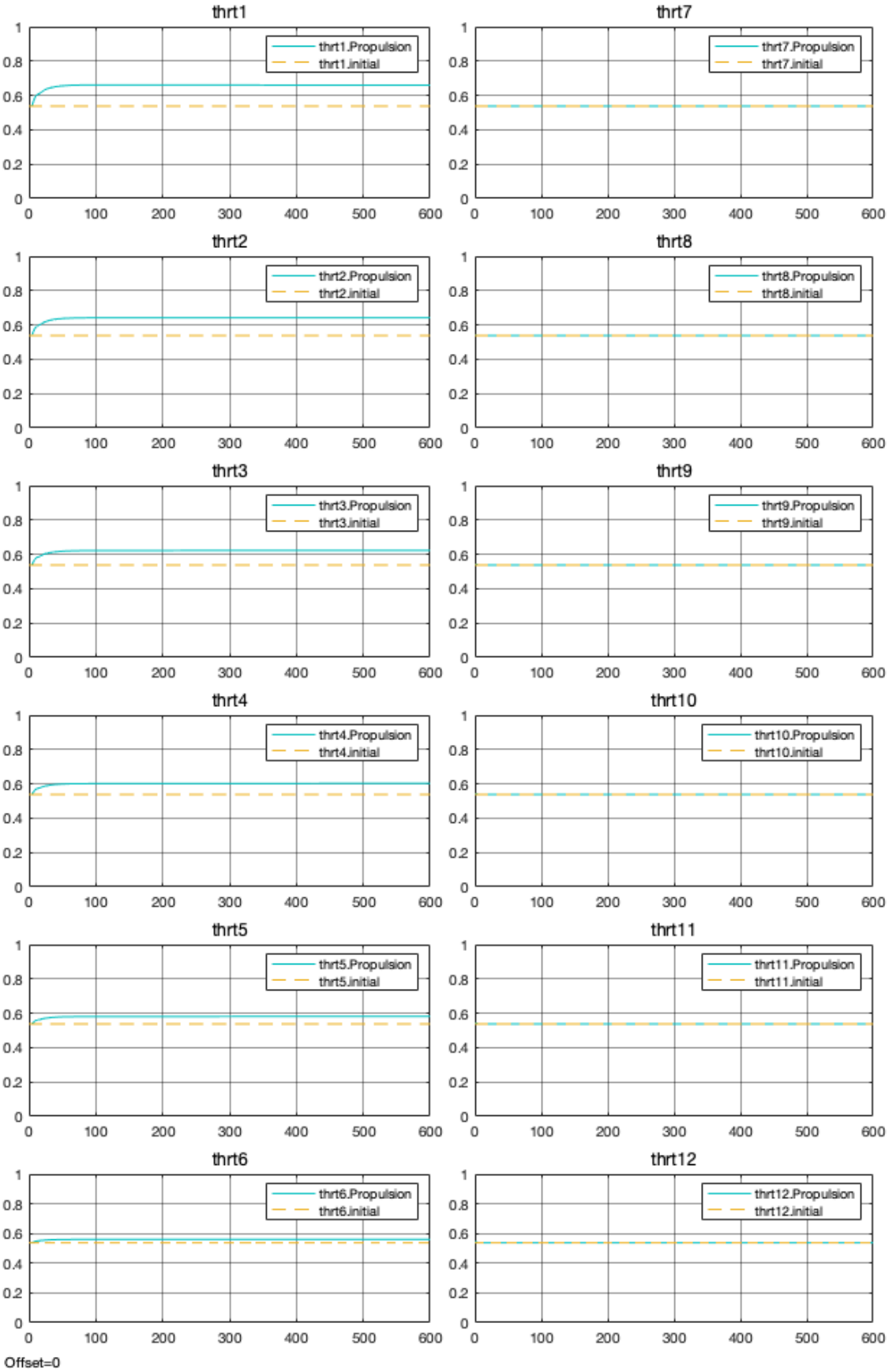


Figure 5.6: Simulation $\dot{\psi} = 15°/min$ DEP results - Propulsive Controls.

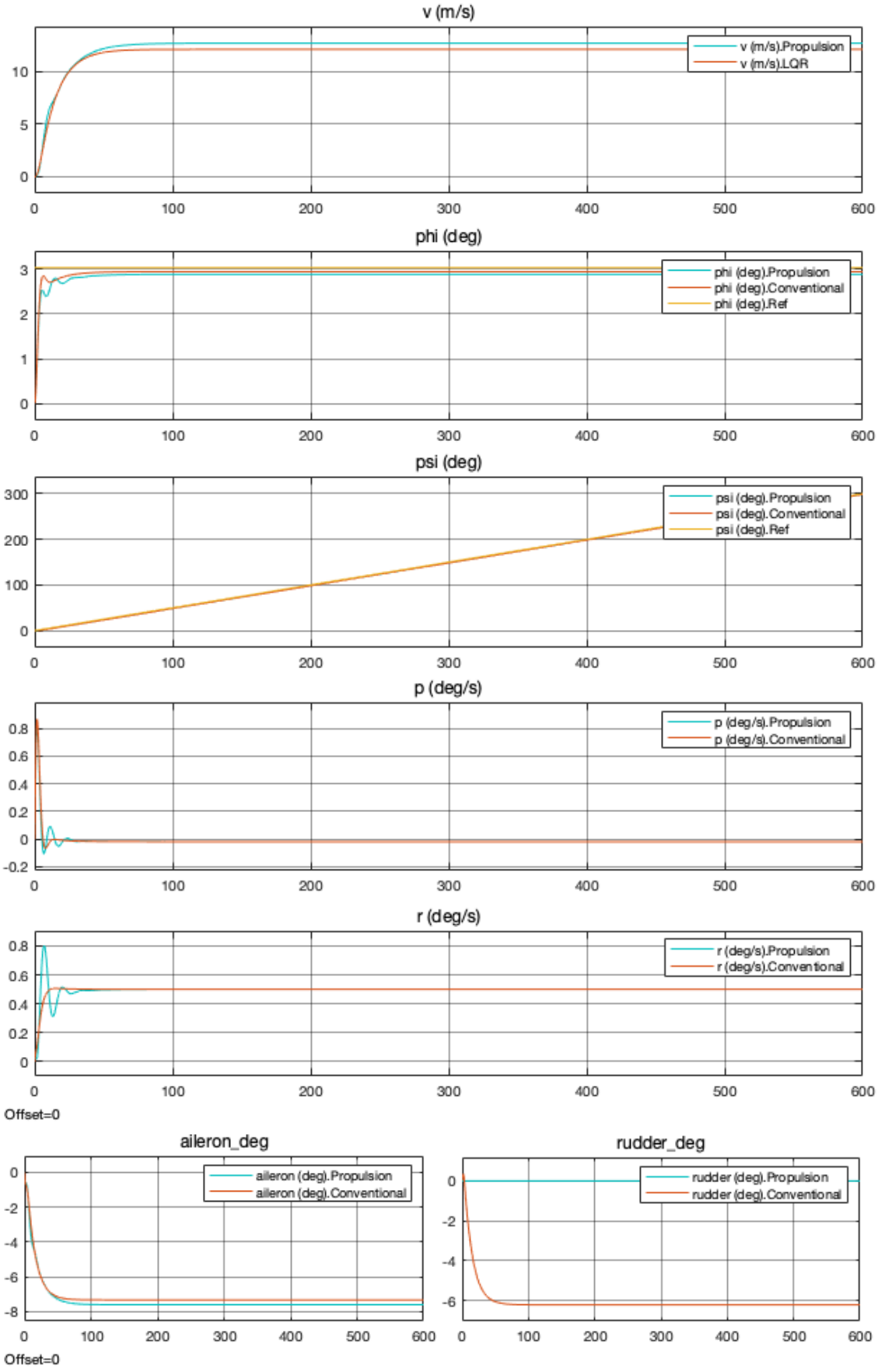


Figure 5.7: Simulation $\dot{\psi} = 30°/min$ DEP results - States and Conventional Controls.

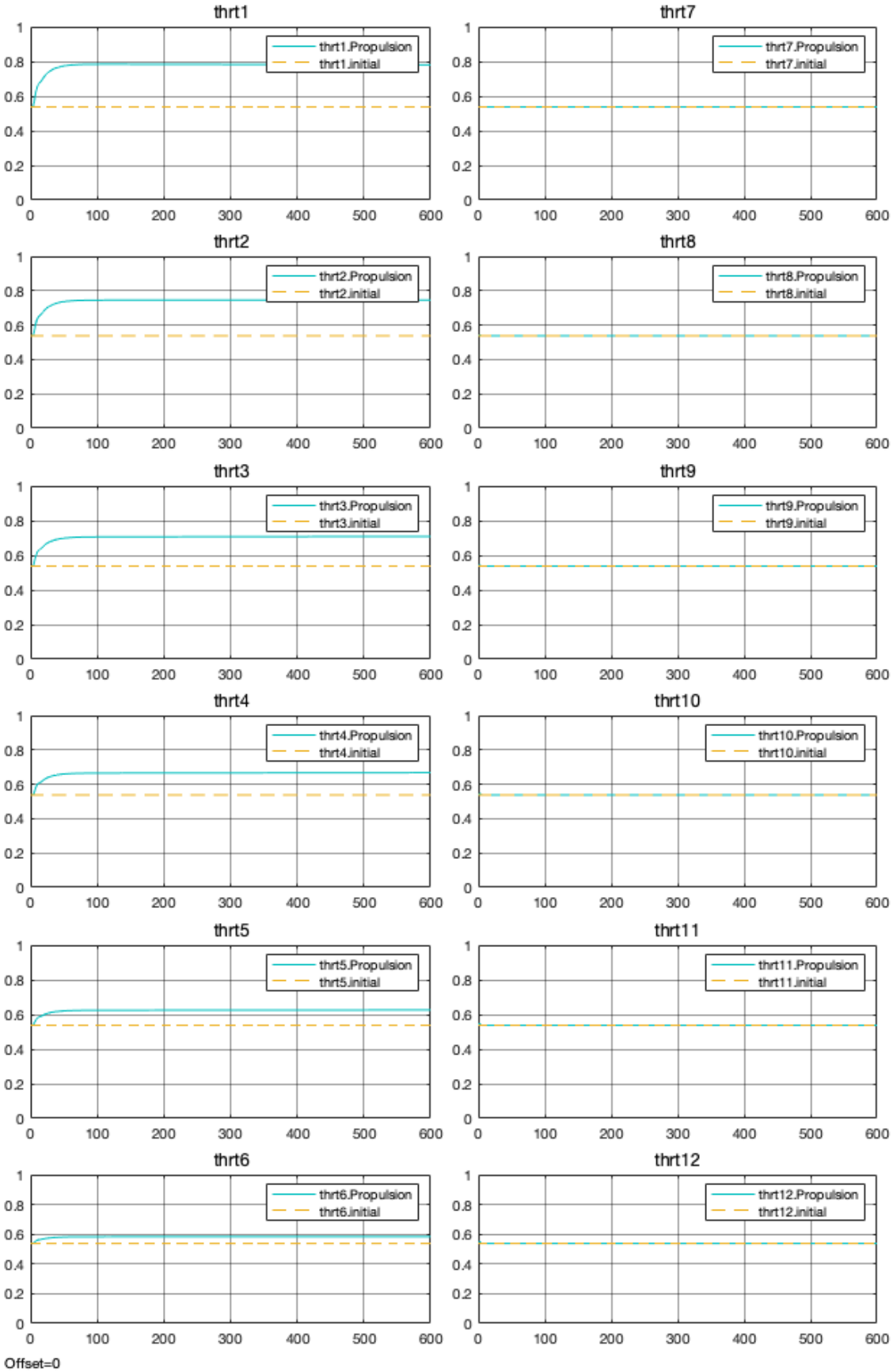


Figure 5.8: Simulation $\dot{\psi} = 30°/min$ DEP results - Propulsive Controls.

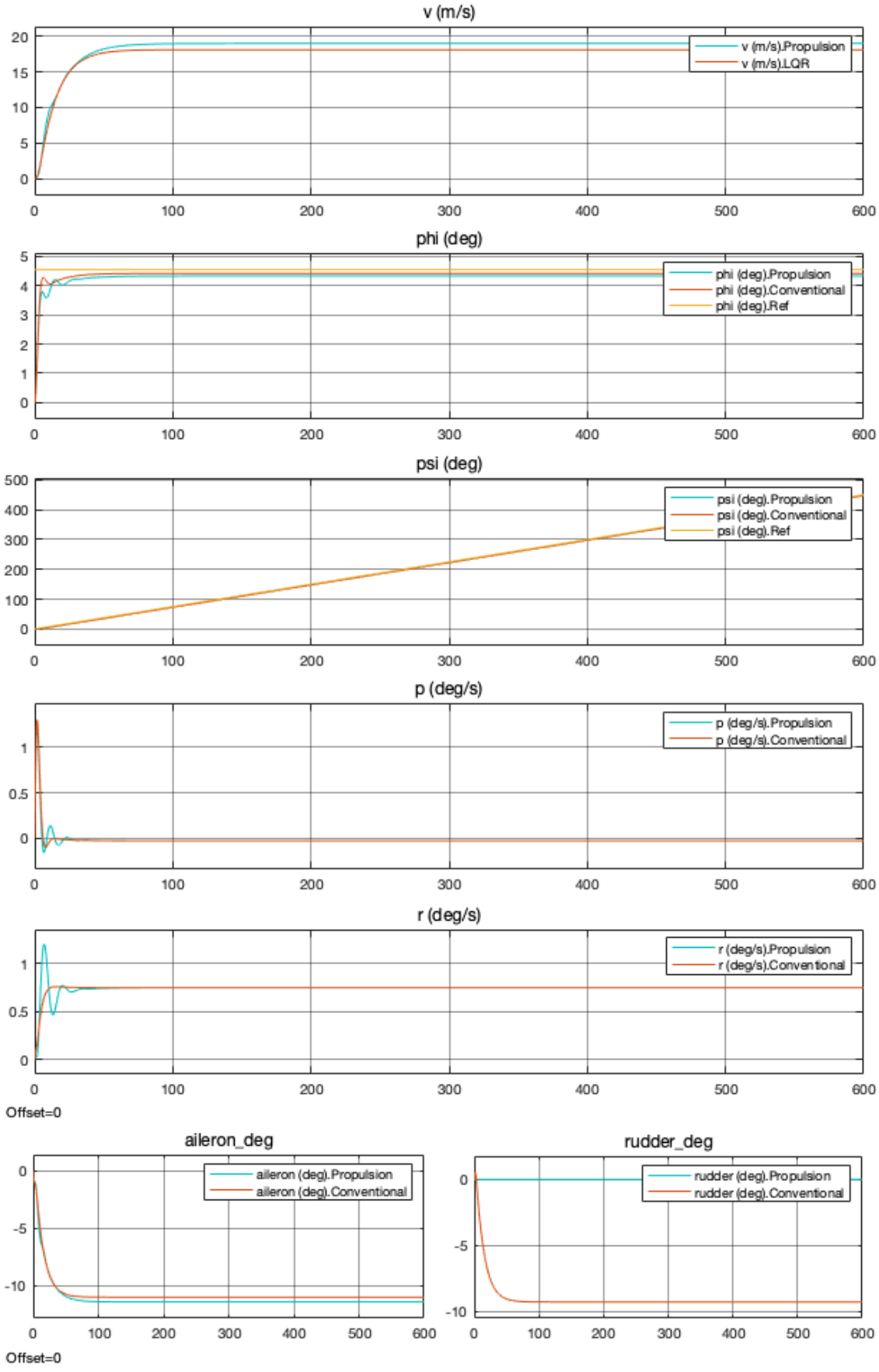


Figure 5.9: Simulation $\dot{\psi} = 45°/min$ DEP results - States and Conventional Controls.

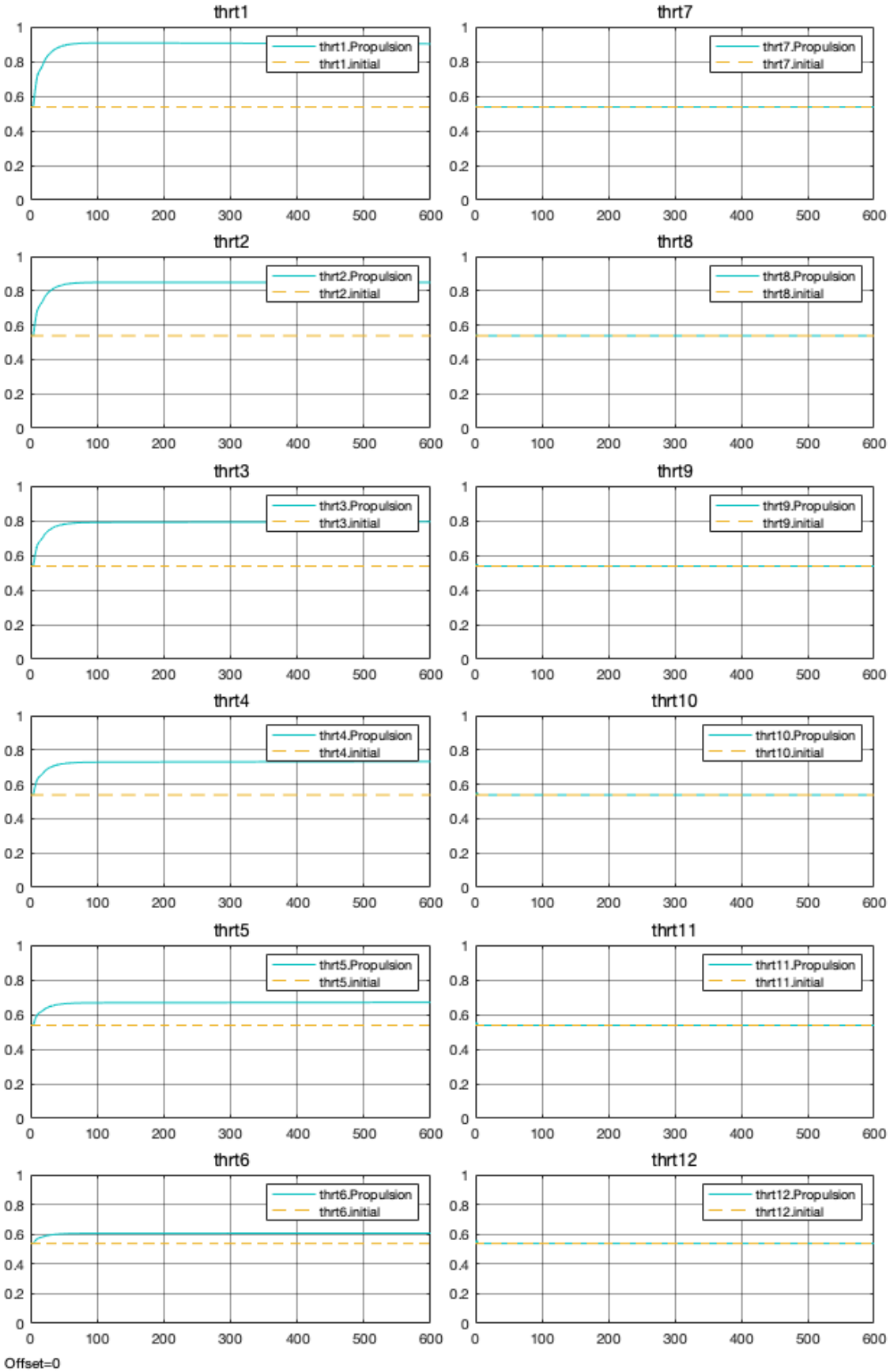


Figure 5.10: Simulation $\dot{\psi} = 45°/min$ DEP results - Propulsive Controls.

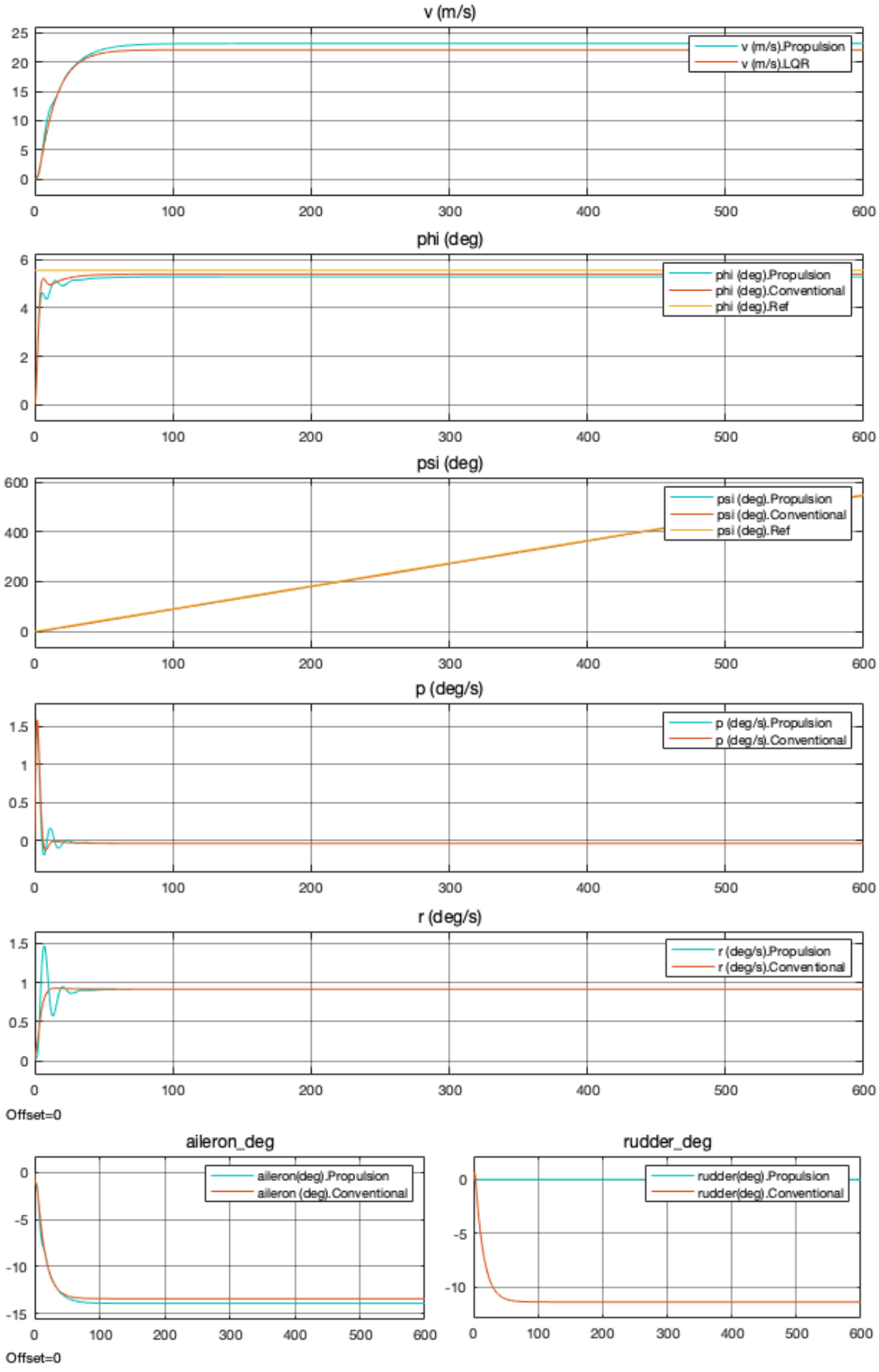


Figure 5.11: Simulation $\dot{\psi} = 55°/min$ DEP results - States and Conventional Controls.

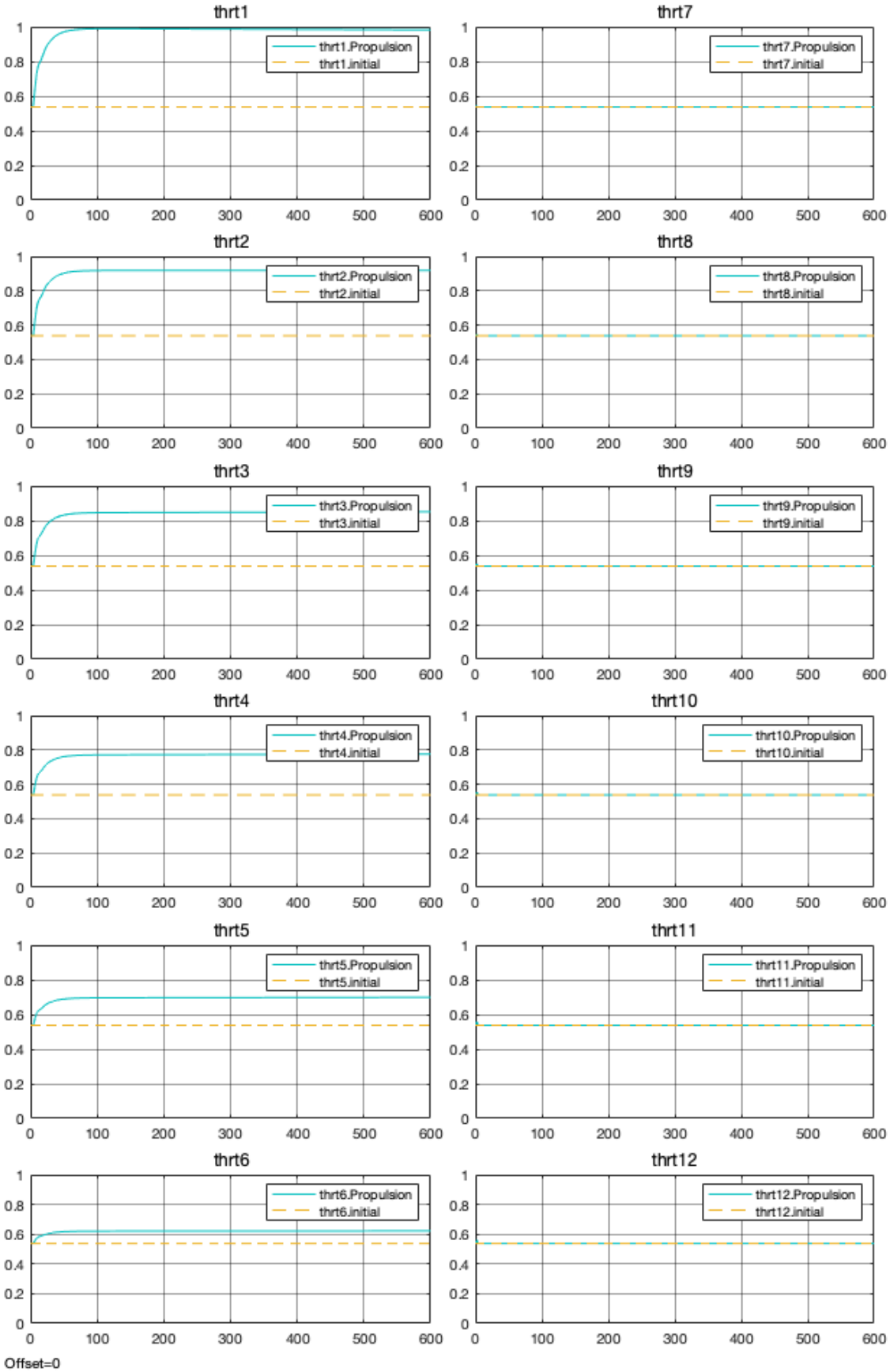


Figure 5.12: Simulation $\dot{\psi} = 55°/min$ DEP results - Propulsive Controls.

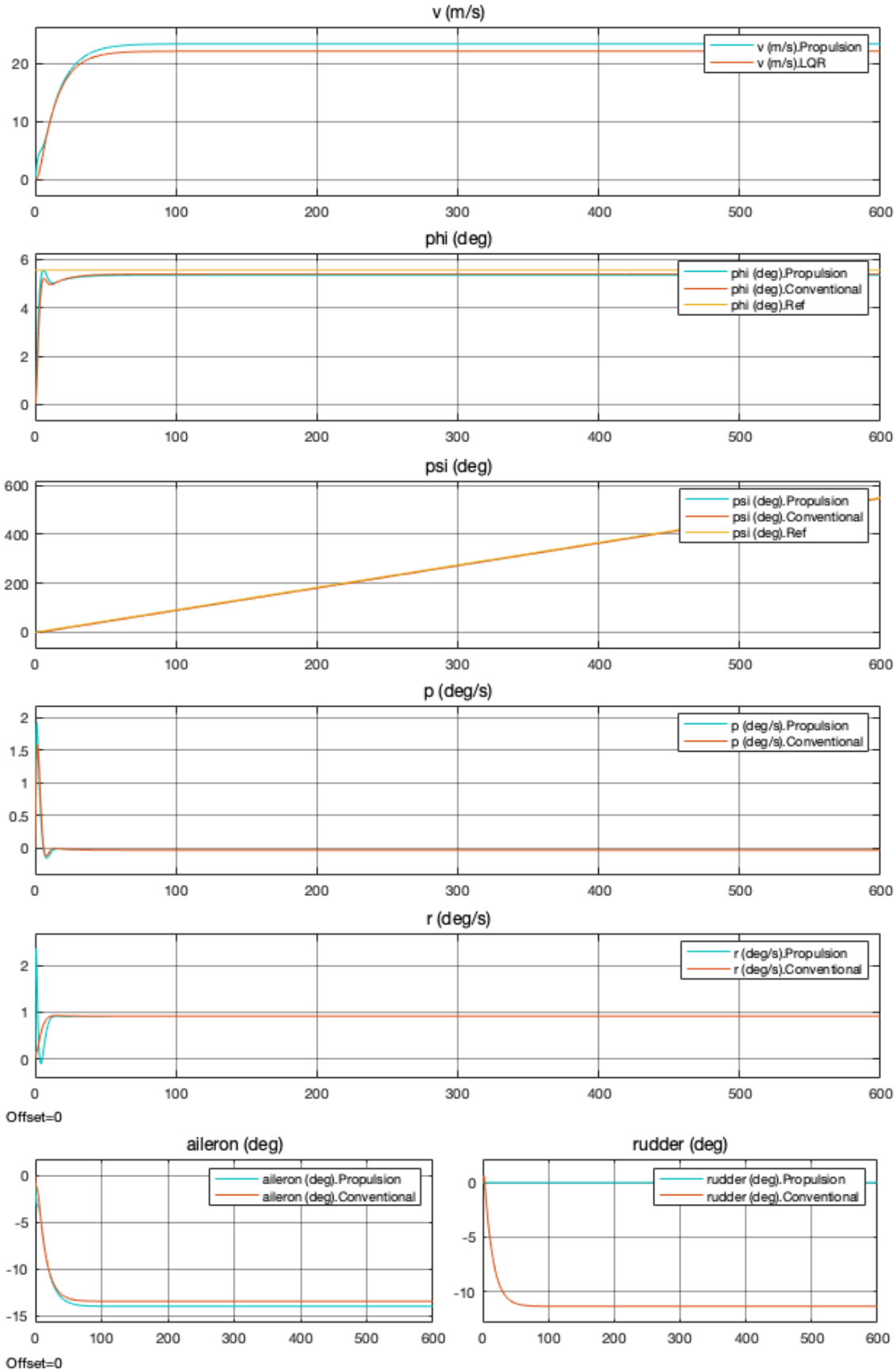


Figure 5.13: Simulation $\dot{\psi} = 55°/min$ DEP results - States and Conventional Controls for Propulsive Controls without restrictions.

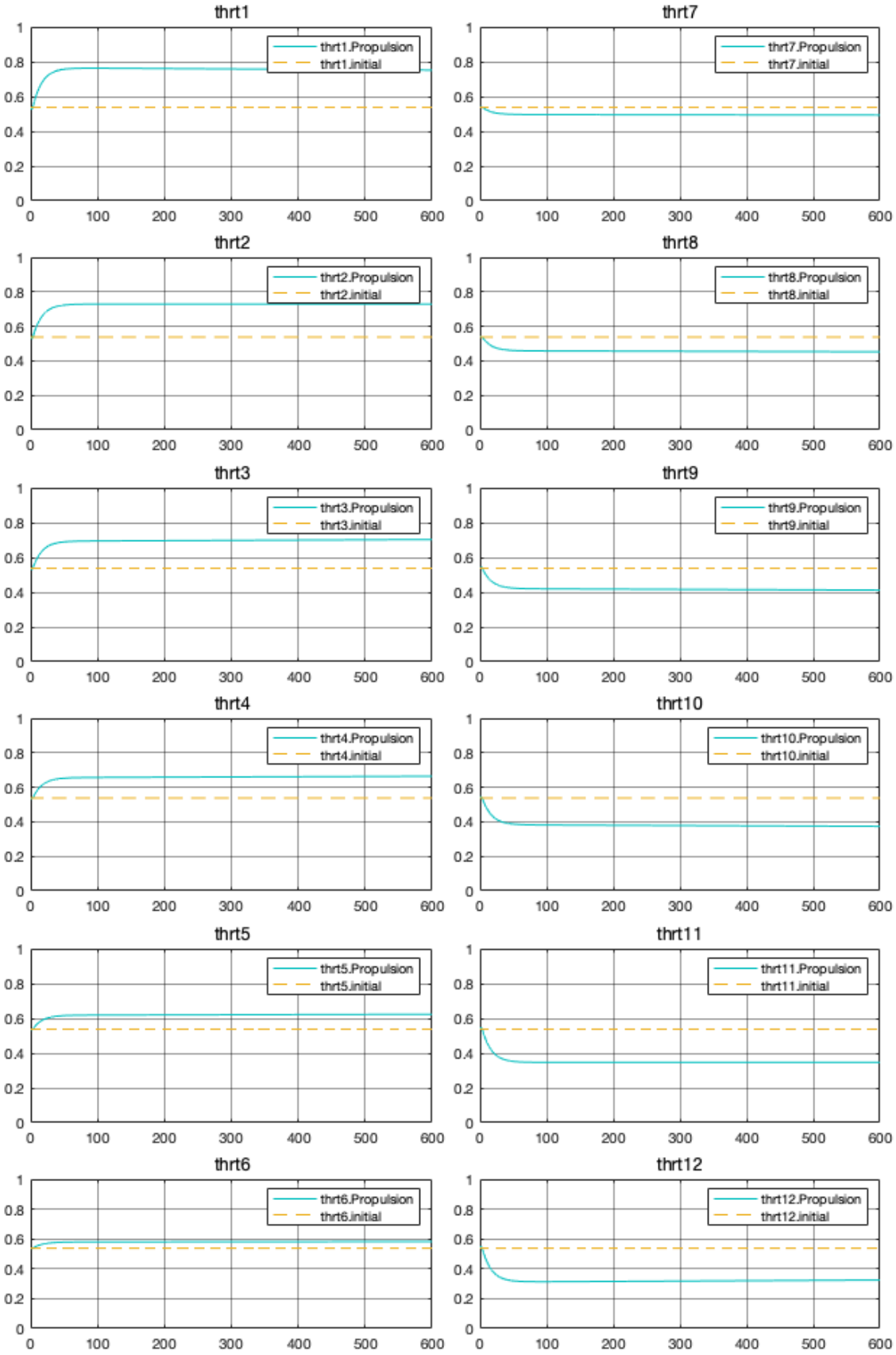


Figure 5.14: Simulation $\dot{\psi} = 55°/min$ DEP results - Propulsive Controls without restrictions.

The x axis on the simulations shows the simulation time in seconds while the sate ($v\ \phi\ \psi\ p\ r$) and control ($\delta_a\ \delta_r\ \delta_{th_1}\ \delta_{th_2}\ \delta_{th_3}\ \delta_{th_4}\ \delta_{th_5}\ \delta_{th_6}\ \delta_{th_7}\ \delta_{th_8}\ \delta_{th_9}\ \delta_{th_{10}}\ \delta_{th_{11}}\ \delta_{th_{12}}$) variables appear on the y axis.

The two study cases can be compared from Figure 5.2 to Figures 5.7 and 5.8 and from Figure 4.6 to Figures 5.5 and 5.6. Analysing the graphics it is possible to observe that the side speed is lower for the original Tecnam configuration in about $8m/s$ for $\dot{\psi} = 30°/min$ and $3m/s$ for $\dot{\psi} = 15°/min$. For both turn rates, the yaw rate and roll rate have about the same overshoot and settling time. As expected, for the new configuration, with a smaller vertical tail area, a larger rudder deflection can be identified, along with a larger aileron deflection.

It may be seen that the peak overshoot is very low for the DEP controller, for example for the yaw rate $r$ never exceeds $0.5°$, taking its larger value for the highest turn rate. For the roll rate $p$ the overshoot is even smaller, also increasing for higher turn rates.

Looking at the trends, it is clear that with the exception of the yaw rate $r$ the peak overshoot with the conventional control surfaces actuation is higher than with the propulsion as a control actuator, for the same weighting matrixes and control parameters.

From the simulations it is possible to observe that the propulsion control is able to sustain all simulated turns, only reaching the peak of the tip engine at $\dot{\psi} = 55°/min$. The results are coherent with the expected and the engines closest to the tip of the wing have higher throttle inputs generating higher yaw moments and sustaining the turn. It is due noticing that the most cost effective solution found by the controller is not raising only the engines located on the tips to the full max throttle, but instead use all engines gradually.

It is also due noticing that the fact that the engines on the right side of the wing are stagnated at the initial throttle input is an imposed condition by the author, since no longitudinal model was developed and the altitude loss due to thrust loss cannot be modelled or corrected in this work. Therefore, the engines mandatorily will have a lower limit equal to its initial position upon being activated, in this case the trim condition, although it is not their cost ideal actuation, as verified by Figure 5.14. In this Figure, it is also clear that a turn rate of $\dot{\psi} = 55°/min$ is no longer the peak for generating yaw moment with the tip engine, which was expected.

An interesting fact is that a higher aileron input is needed for the propulsion control than it would be if the aircraft was controlled conventionally, as can be seen in the graphics from all five simulations. This is due to the combined roll moment induced by the differential thrust, that is higher than the rudder's according to the approximations made on Equation 4.18a.

The side speed $v$ also assumes lower values for the conventional control than for the differential thrust control, as noted in all simulations. The approximation made to the side force component of the thrust force (Equation 4.10b), may justify this speed difference although it doesn't directly show on the driving matrix $B$ (Equation 4.86).

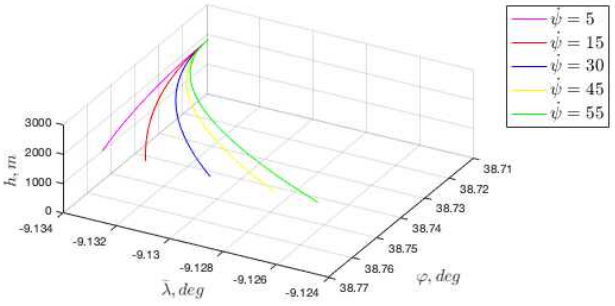


Figure 5.15: Coordinated turn simulations representation on the Geodetic referential (legend in degrees per minute).

No further rates of turn were simulated since the typical values for this study's the class of aircrafts don't exceed the simulated or reach such high rates, therefore it would be beyond the scope of this work. The trajectories of the five simulated turns are presented on Figure 5.15 on Geodetic coordinates for easier visualisation.

## 5.2 Critical engine failure simulation

During an engine failure, as described in Section 3.2.1.1, the aircraft flies under an asymmetric power condition, where the engine symmetrically positioned to the failed engine and the failed engine's drag cause an adverse yaw moment ($N_E + N_D$) that needs to be counteracted, as illustrated in Figure 5.16. To counteract this moment, the aircraft may either use the rudder or, for DEP vehicles, attempt to re-distribute the remaining engine's power in order to stabilise the flight path without actioning the rudder.

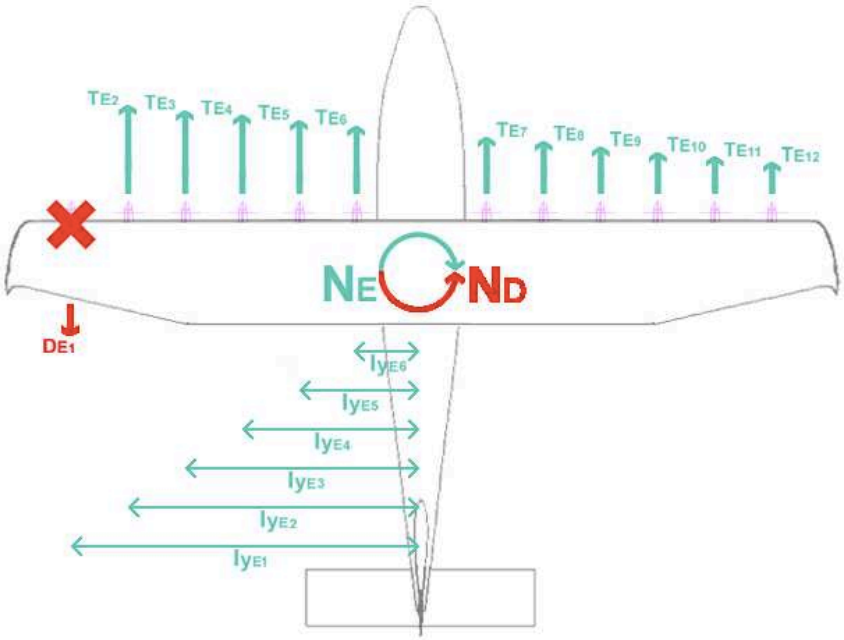


Figure 5.16: Schematics of a critical engine failure.

The parameters, matrixes, control gains and structure for this simulation can be found on the previous section. Trim conditions were used as initial values.

First, two additional simulation for trim condition will be made (i.e. $\psi = 0$ and $\phi = 0$), to see how the engines re-distribute the thrust, also at Mach $0.18$ and with a $2450\ m$ altitude. One with the same throttle limitation ($\delta_{th} \geq \delta^*_{th}$) – Figures 5.17 and 5.18, and another without – Figures 5.19 and 5.20.
Based on those results, it will be decided whether or not to impose a throttle limitation and the same rates of turn from the previous simulations will be considered:

- $\dot{\psi} = 5°/min$ – Figures 5.21 and 5.22
- $\dot{\psi} = 15°/min$ – Figures 5.23 and 5.24
- $\dot{\psi} = 30°/min$ – Figures 5.25 and 5.26
- $\dot{\psi} = 45°/min$ – Figures 5.27 and 5.28
- $\dot{\psi} = 55°/min$ – Figures 5.29 and 5.30

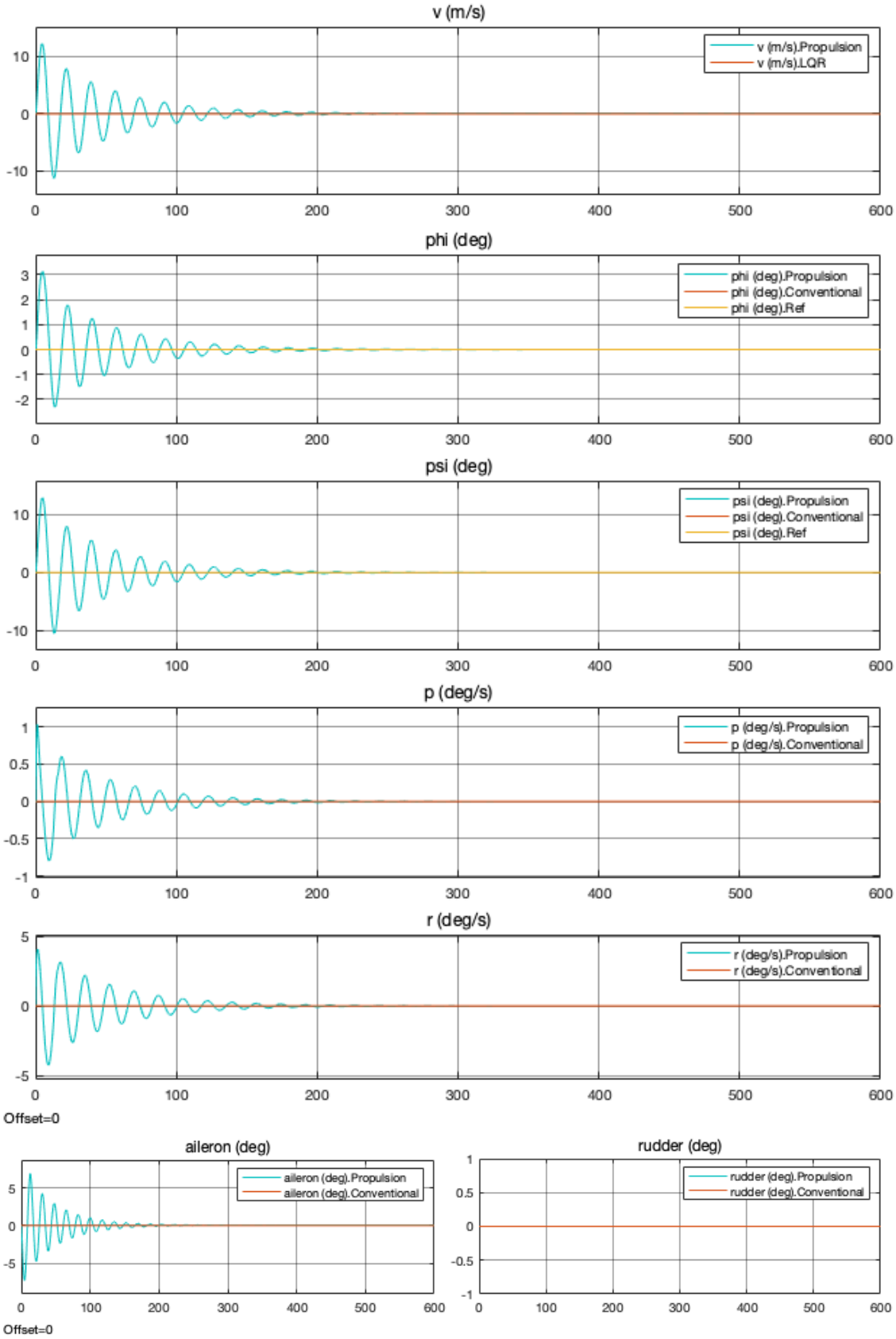


Figure 5.17: Simulation for trim condition with critical engine out DEP results - States and Conventional Controls.

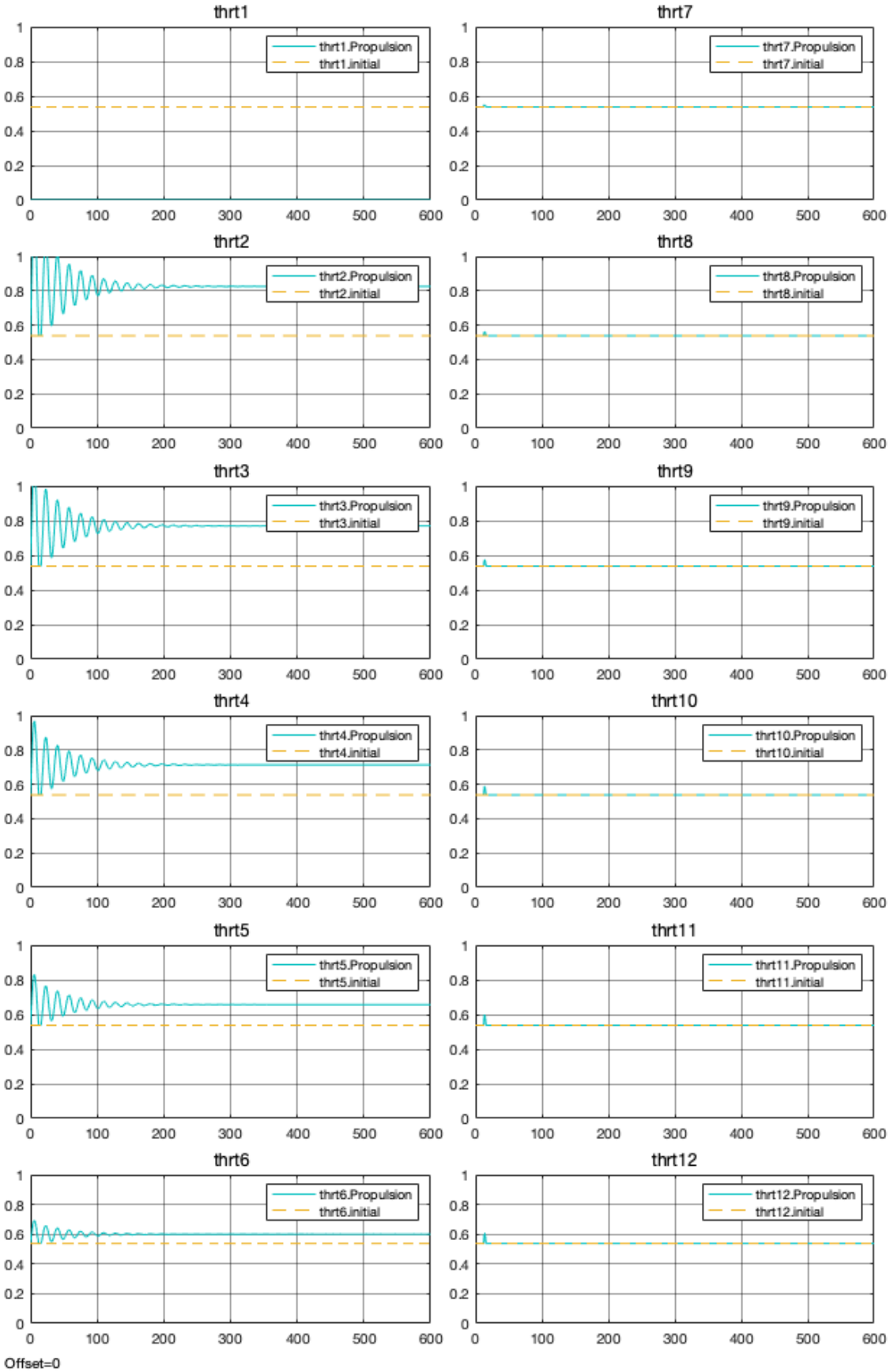


Figure 5.18: Simulation for trim condition with critical engine out DEP results - Propulsive Controls.

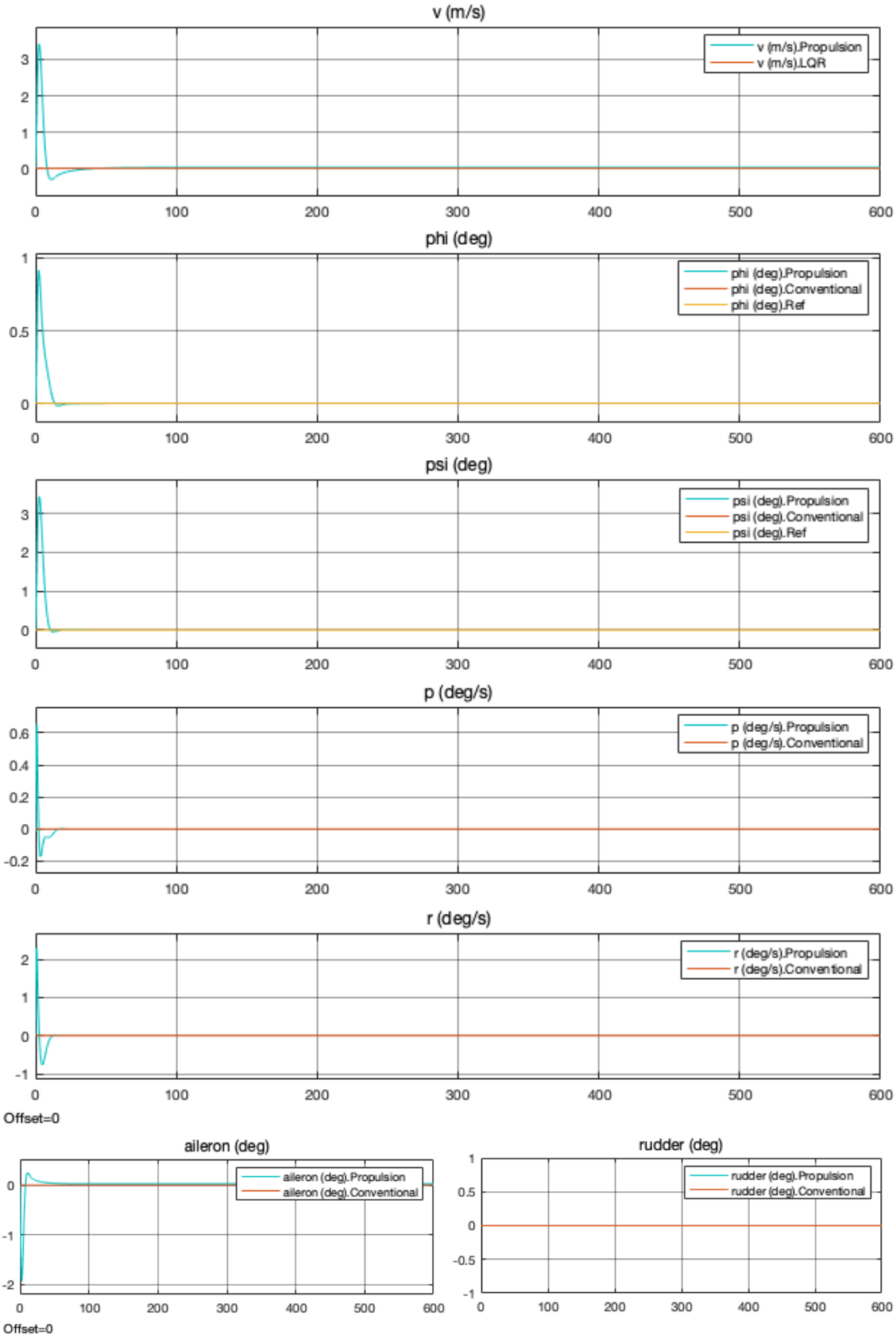


Figure 5.19: Simulation for trim condition with critical engine out DEP results - States and Conventional Controls for Propulsive Controls without restrictions.

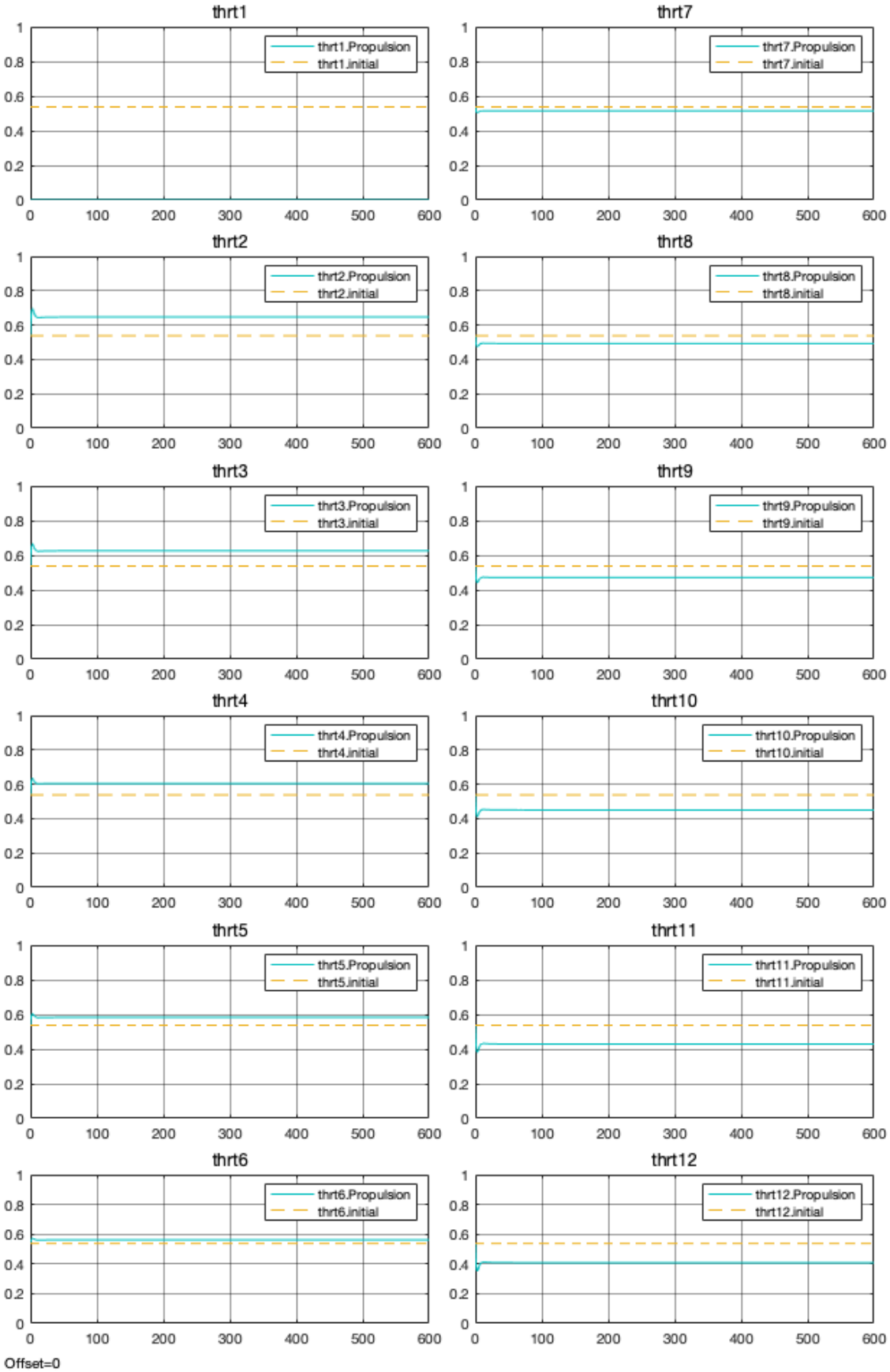


Figure 5.20: Simulation for trim condition with critical engine out DEP results - Propulsive Controls without restrictions.

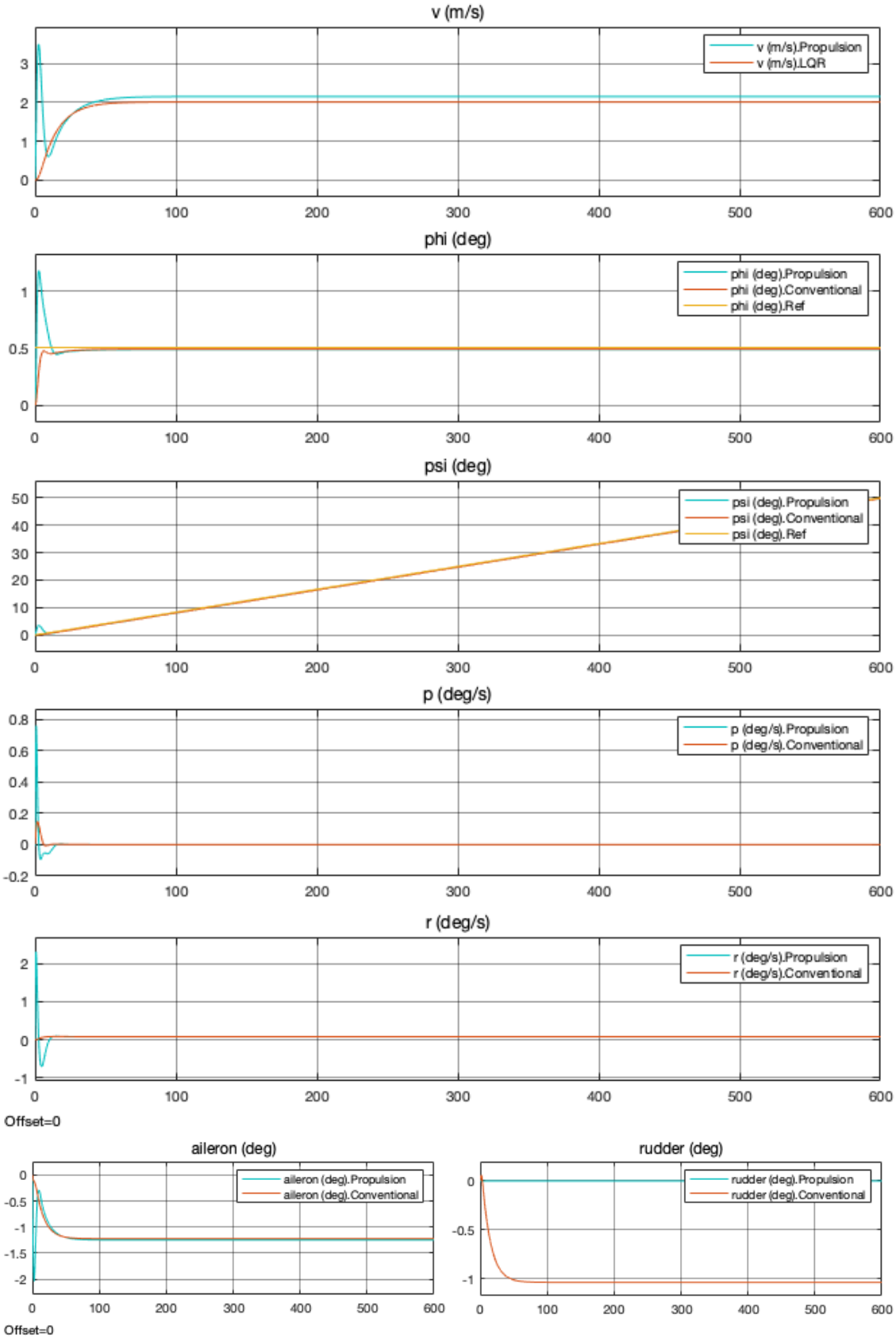


Figure 5.21: Simulation $\dot{\psi} = 5°/min$ with critical engine out DEP results - States and Conventional Controls.

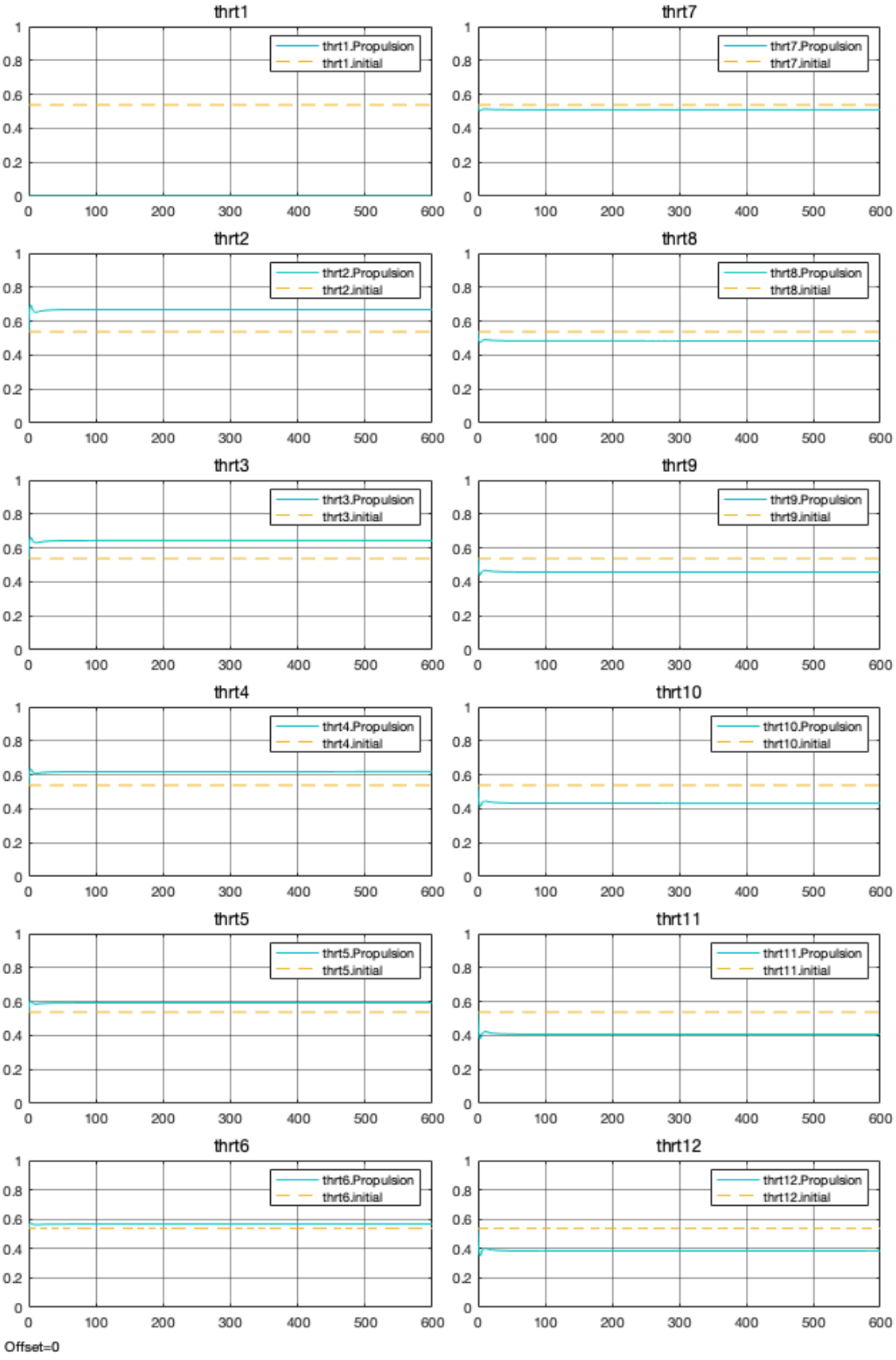


Figure 5.22: Simulation $\dot{\psi} = 5°/min$ with critical engine out DEP results - Propulsive Controls.

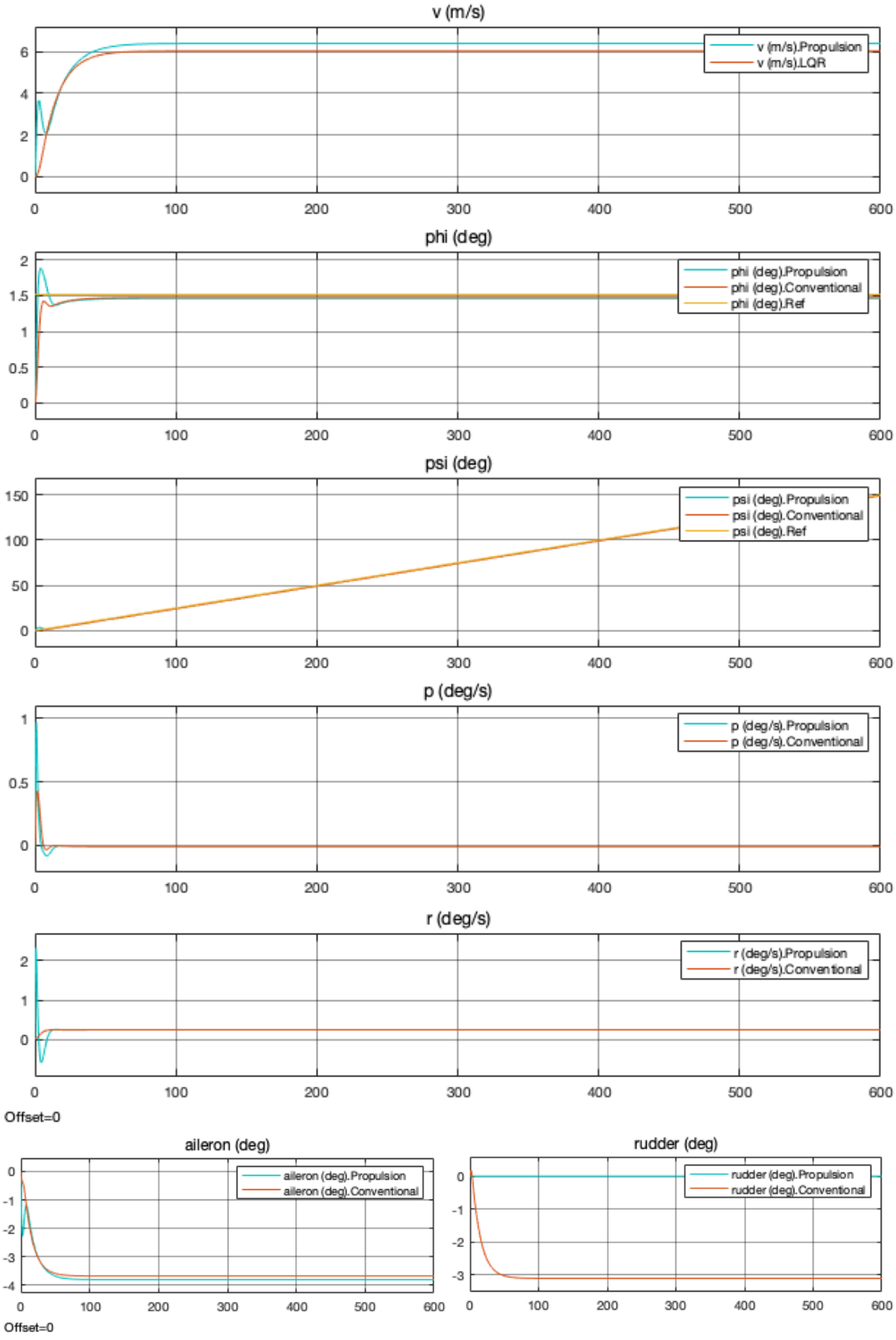


Figure 5.23: Simulation $\dot{\psi} = 15°/min$ with critical engine out DEP results - States and Conventional Controls.

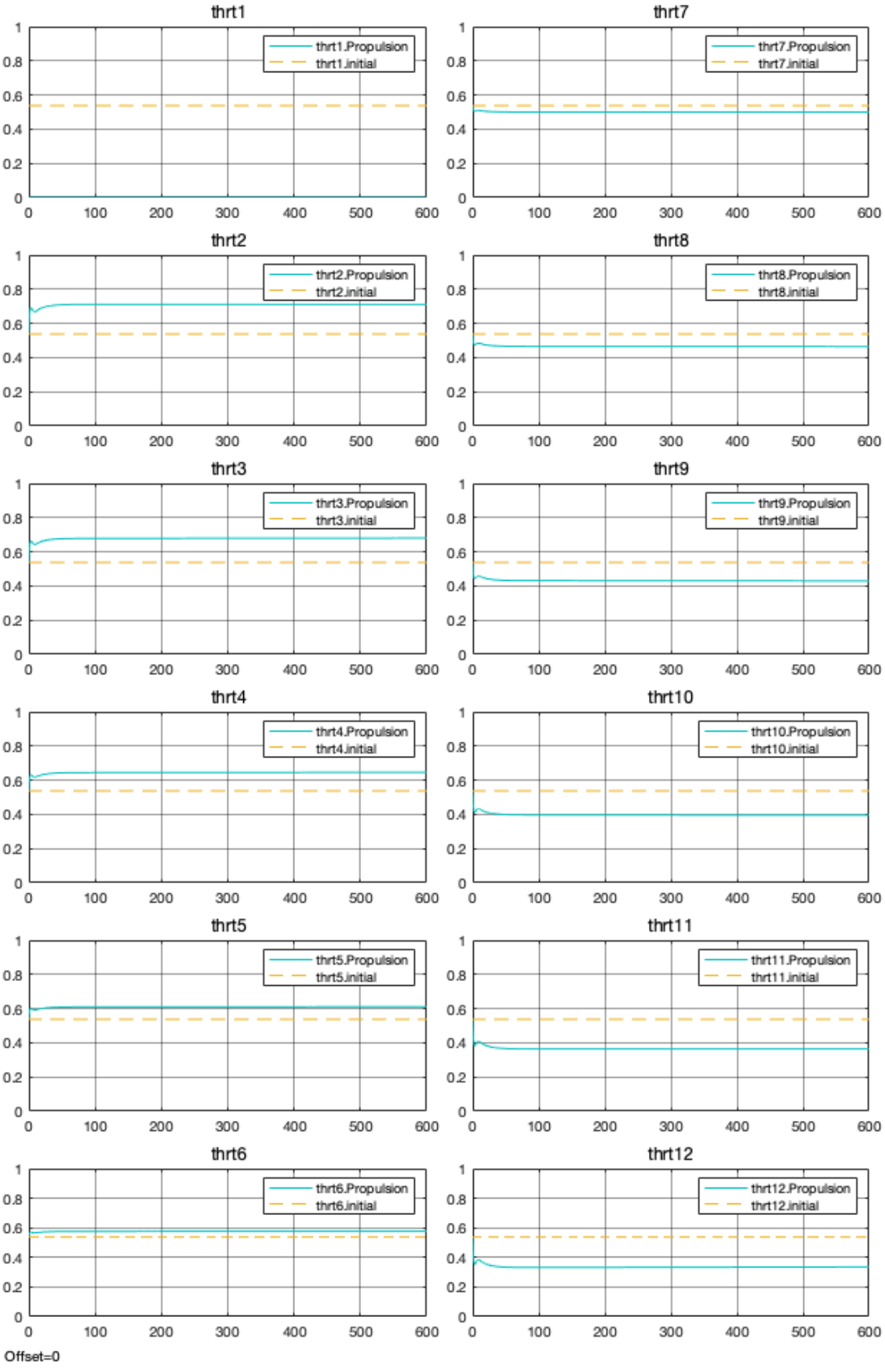


Figure 5.24: Simulation $\dot{\psi} = 15°/min$ with critical engine out DEP results - Propulsive Controls.

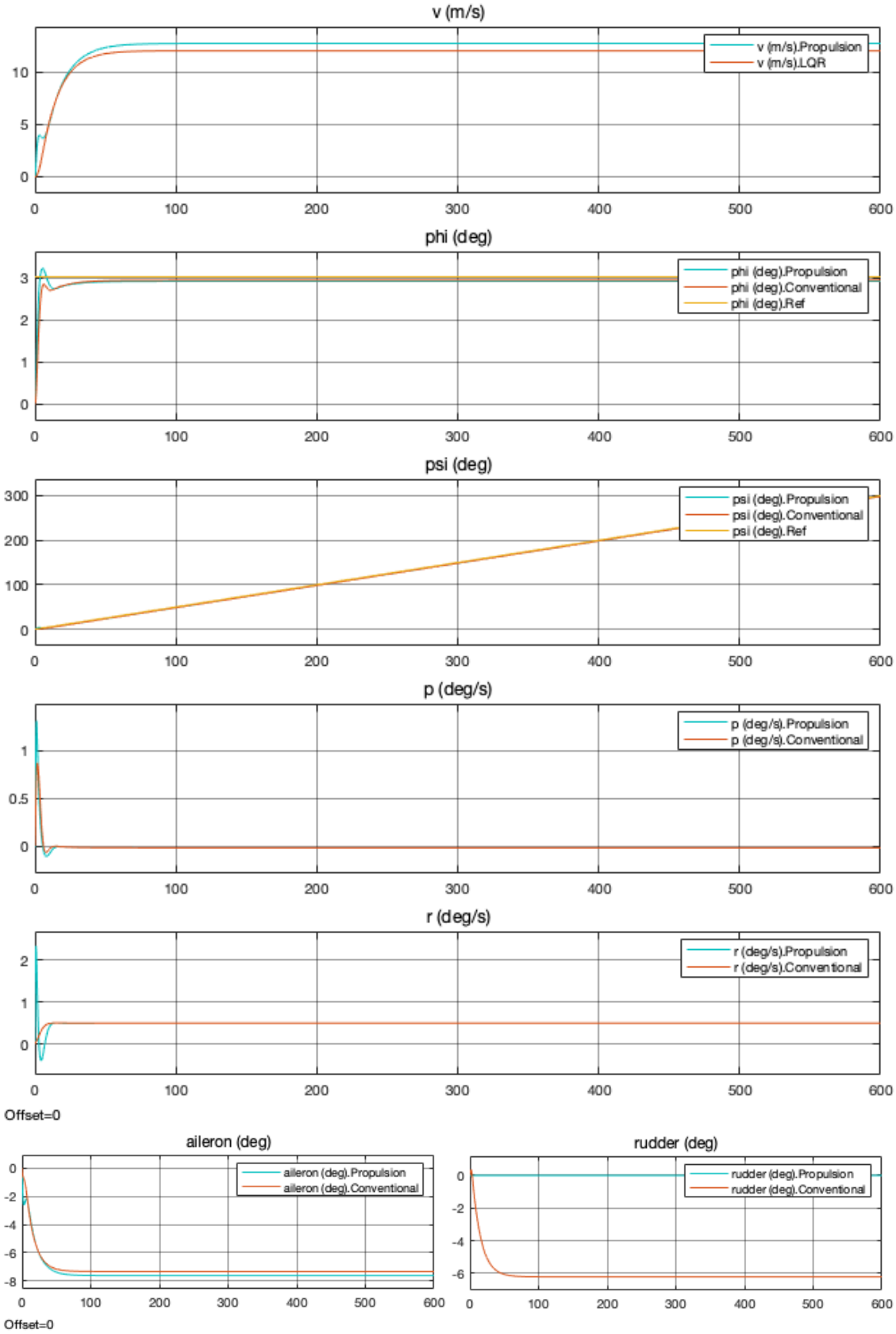


Figure 5.25: Simulation $\dot{\psi} = 30°/min$ with critical engine out DEP results - States and Conventional Controls.

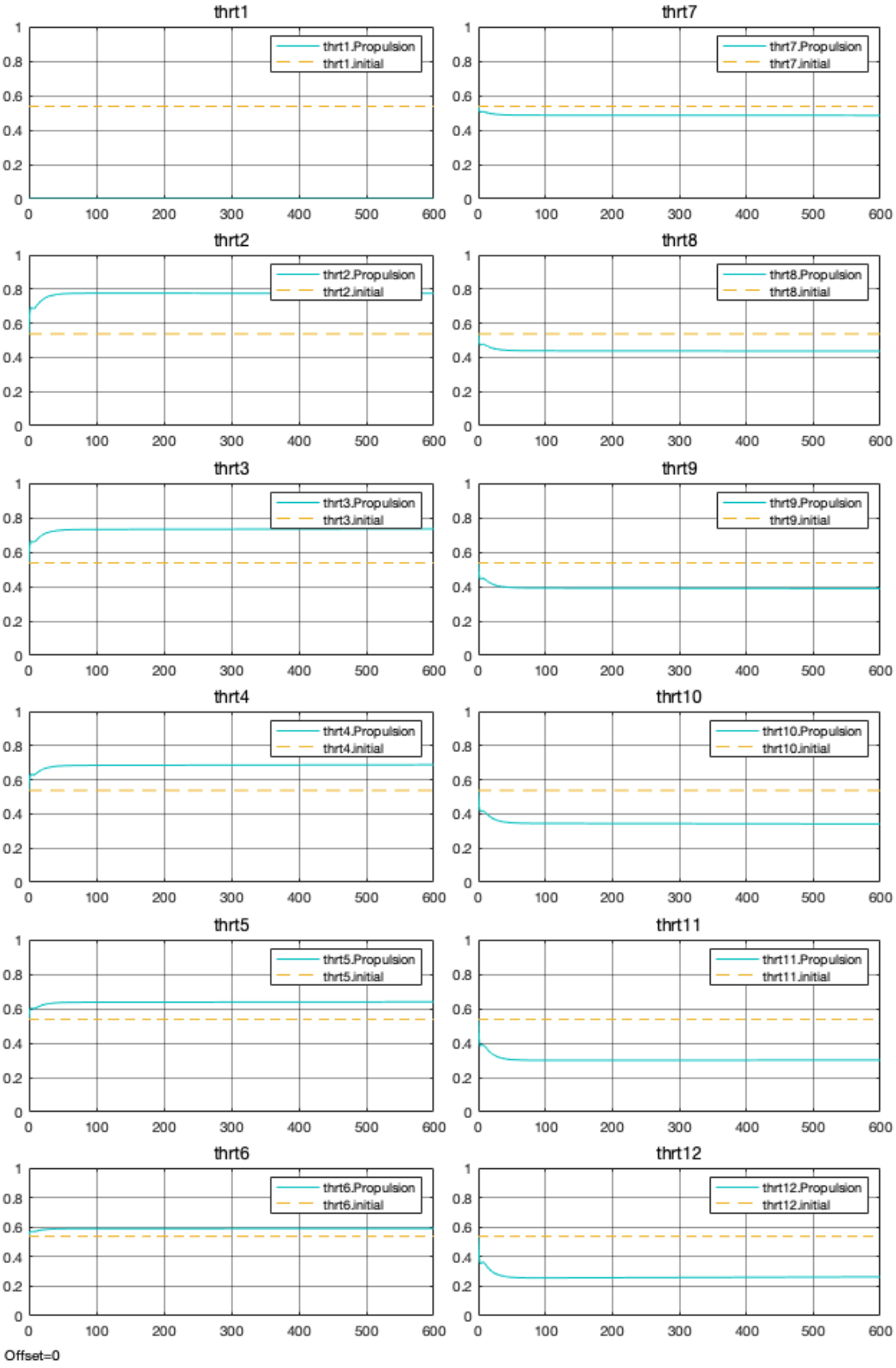


Figure 5.26: Simulation $\dot{\psi} = 30°/min$ with critical engine out DEP results - Propulsive Controls.

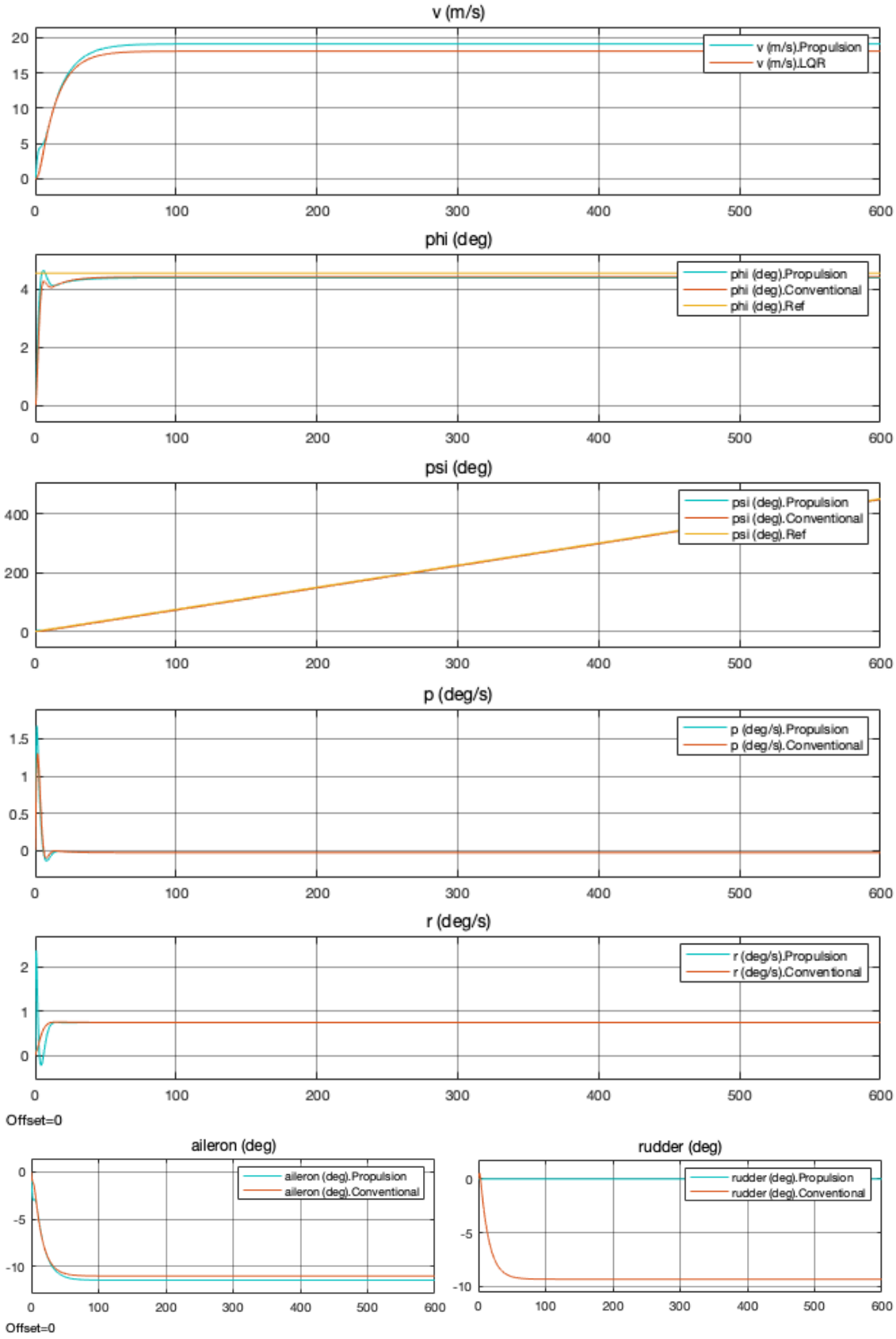


Figure 5.27: Simulation $\dot{\psi} = 45°/min$ with critical engine out DEP results - States and Conventional Controls.

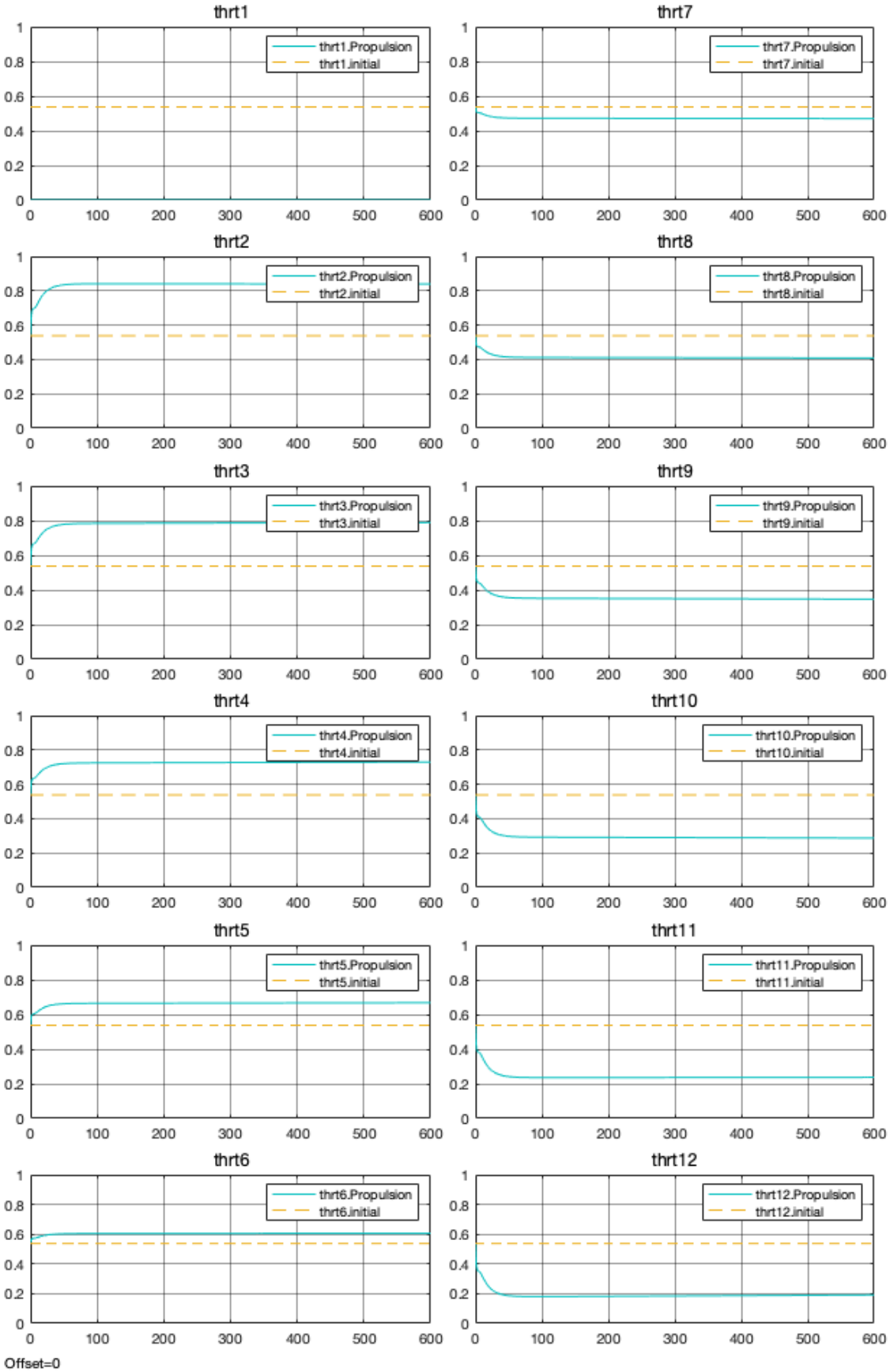


Figure 5.28: Simulation $\dot{\psi} = 45°/min$ with critical engine out DEP results - Propulsive Controls.

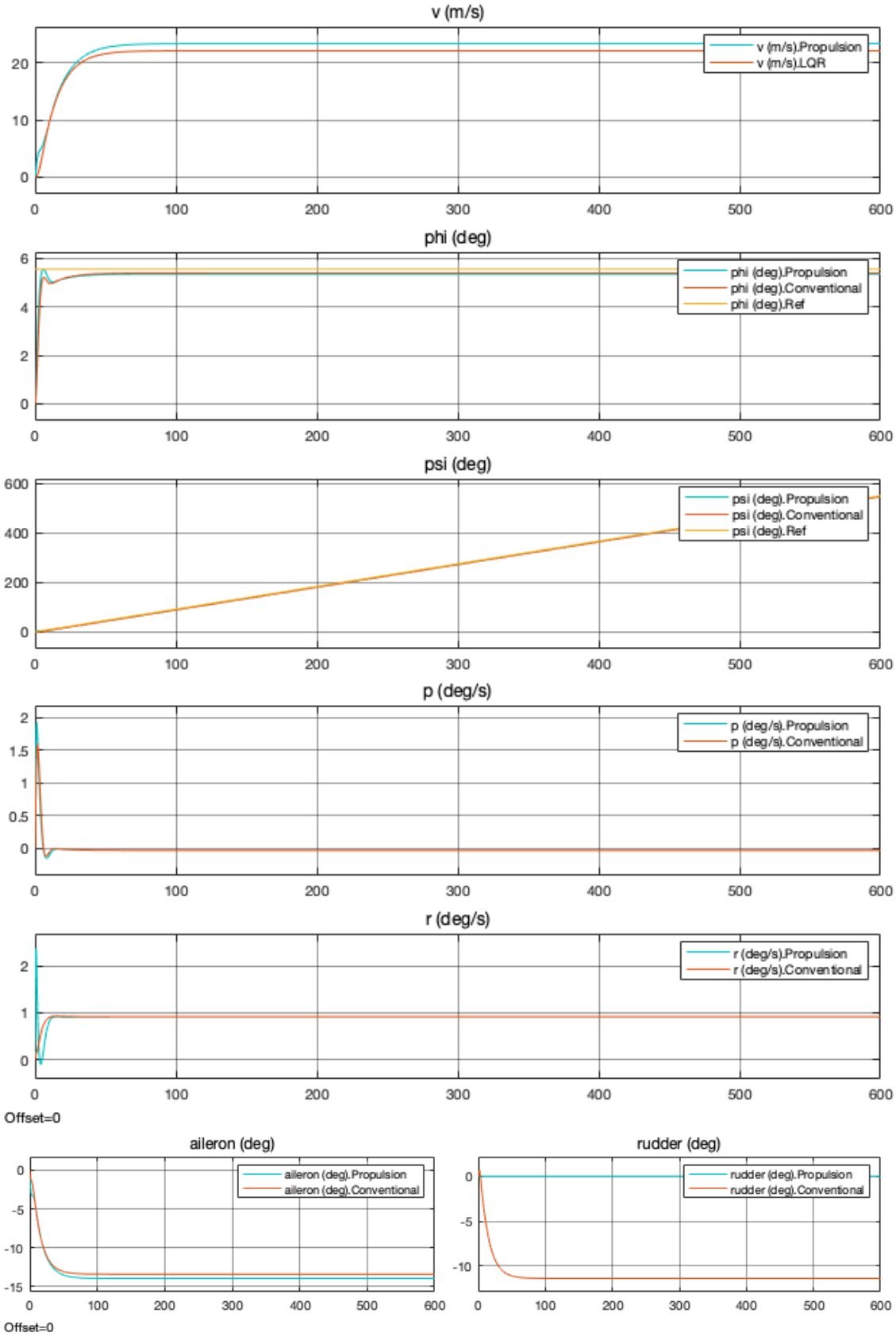


Figure 5.29: Simulation $\dot{\psi} = 55°/min$ with critical engine out DEP results - States and Conventional Controls.

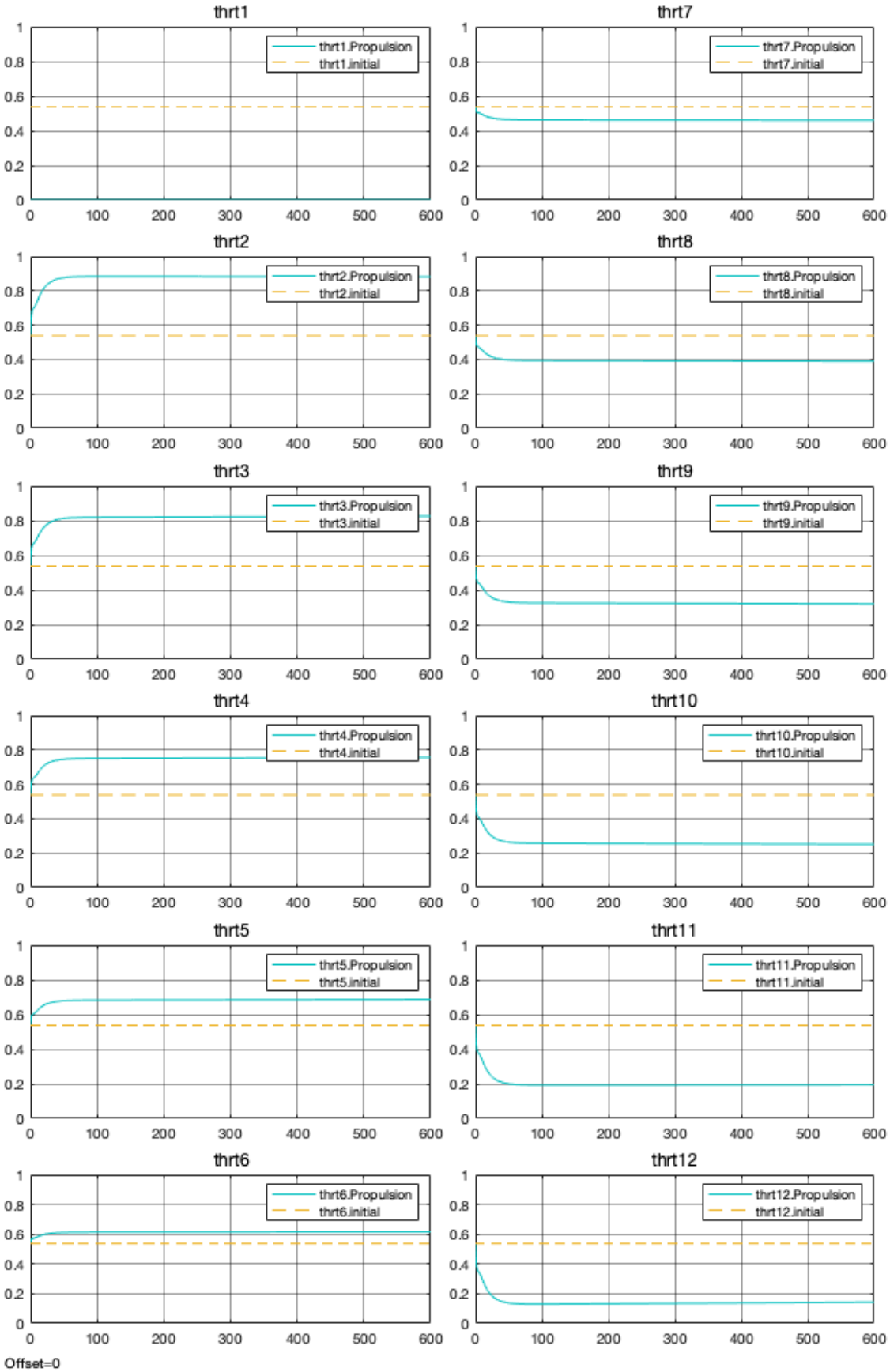


Figure 5.30: Simulation $\dot{\psi} = 55°/min$ with critical engine out DEP results - Propulsive Controls.

Again, the x axis on the simulations shows the simulation time in seconds while the sate ($v\ \phi\ \psi\ p\ r$) and control ($\delta_a\ \delta_r\ \delta_{th_1}\ \delta_{th_2}\ \delta_{th_3}\ \delta_{th_4}\ \delta_{th_5}\ \delta_{th_6}\ \delta_{th_7}\ \delta_{th_8}\ \delta_{th_9}\ \delta_{th_{10}}\ \delta_{th_{11}}\ \delta_{th_{12}}$) variables appear on the y axis.

In order to simulated the failed engine, the third column of the driving matrix $B_{(case_II)}$ was set to zero, as well as the third line of the gain matrix $K_{H_{\infty(case_{II})}}$.

From Figures 5.17 and 5.18, it is straightforward that if the lower limit restriction is kept, the above approximation of the gains has a large peak overshoot and takes to long (about three minutes) to settle into stability. Therefore, those gains would need to be re-calculated for this engine arrangement (i.e., one engine less) and different gains would need to be used for each engine configuration (according to the number of active/failed engines).

On the other hand, if the restriction is removed and the controller is allowed to balance the thrust distribution between both sides (Figures 5.19 and 5.20), a stabilising solutions is achieved immediately and without the need for different gains, although with a slight peak overshoot. For the remaining simulations that strategy was adopted and the lower boundary of the engine throttle was removed. This solution may need stabilator deflection to correct the pitch contribution from Equation 4.18b.

Comparing the engine out coordinated turns with the all engines operating coordinated turns, it can be generalised that the peak overshoot increases with a failed engine, even for the side speed that didn't have any overshoot in the first scenarios. The peak overshoot decreases for the side speed, roll angle, yaw angle and aileron deflection as the turn rate increases, i.e. bigger overshoot on those variables for $\dot{\psi} = 5°/min$ than for $\dot{\psi} = 55°/min$. The settling time is about the same between the engine out and the all engines operating case for aileron deflection and all the state variables, except for yaw rate $r$ which decreases for the engine out case.

For the same turn rate, the same aileron deflection is used between the all engines operating and the engine out case, as can be seen in the graphics from all five simulations. The side speed $v$ also assumes the same values between the two scenarios, as noted in all simulations. This proves the manoeuvrability of the aircraft with the critical engine failed, as the aircraft is able to maintain all commanded states equally as if there had been no failure. Thus, the trajectories of the five simulated turns are similar to the ones from the previous simulation, as shown on Figure 5.31 on Geodetic coordinates.

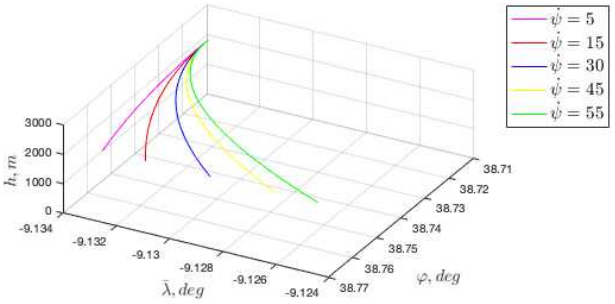


Figure 5.31: Engine-out coordinated turn simulations representation on the Geodetic referential (legend in degrees per minute).

This ability to overcome the failed engine adverse yaw without exceeding the available power and while using a $\delta_{th_n} = 0.53$ throttle setting for cruise and reducing take-off field length when comparing to the original Tecnam configuration, could mean that the engines are overpowered and lower power engines could be used instead, sacrificing of course the two previously mentioned variables (reducing available power at cruise and increasing take-off field length), that the vertical empennage could be reduced even further or even both, depending on the desired project requirements. Hence, a trade-off analysis on this subject would be needed as well as prioritising each of the design requirements to understand the most beneficial solution.

# Chapter 6

# Conclusions

Research was made on topics such as distributed electric propulsion aircraft, propulsion control, aircraft motion, control systems and its tools. The resultant relevant information was gathered in this work.

Considering the engine's thrust for flight control has proven to be very valuable for use and incorporation in the design of future airplanes, as it accommodates several advantages besides providing a safe landing capability in emergency cases and eliminating the need for a less capable hydraulics-dependent backup flight control system, such as reducing the flight control surfaces, tail size, weight and drag.

From a theoretical approach, it is rather perceptible that the DEP incorporation is very beneficial but implementing electric propulsion systems in aviation may reveal to be a considerable challenge, due to the energy storage problem and the extremely high safety standards — there are still many technological and operational difficulties that must be handled before fully introducing these aircraft into production. Nevertheless, a great deal of research is currently focusing on this, for the DEP technology has plenty of potential and new developments open innumerous opportunities for its usage and implementation.

In order to fully understand the validity of this work's propulsion controller, two study cases were compared — an aircraft with conventional control and a modification of the same aircraft for enabling DP control. Two possible solutions for the implementation of the propulsion control were identified: Vectored thrust and Differential/Asymmetric thrust. The author chose to implement the latter, that consists in adding more thrust in one side than the other, in order to turn the aircraft towards the side with the least thrust power, and a comparison between different engine arrangements was made, in order to estimate the best DEP configuration.

A brief and elementary analytic data estimation based on conceptual design methods and certification requirements was performed on Case II's configuration, despite the fact that certification compliance of a distributed electric propulsion aircraft using differential thrust is still under discussion and there are different possible approaches on the matter. If such an optimisation were to be implemented it is not certain current regulations would be the most appropriate, as certification specifications dictate requirements based on traditional aircraft, and as so are not tailored to DEP aircraft. One example is the matter of engine failure probability (Equation 2.1), which states that the probability of an engine failure increases linearly with the number of engines. Based on this, an aircraft with 10 propulsors would be 5 times more likely to suffer an in-flight shutdown (IFSD) of one of them than a twin-engine. Although this is indeed true, the advantage of having the power distributed along 10 engines is that this loss would only represent 10% of the total thrust versus a 50% thrust loss in the twin, making the probability of critical propulsion system failure reduce increasingly with the number of engines. Thus, since the probability of losing specifically the two critical engines in the presented configurations is roughly as likely as losing all engines on a twin-engine, FAR §25.147(a)(1) was considered instead of FAR §25.147(b)(1). Despite this, DEP's many advantages coupled with the increasing drive for electric and hybrid electric aircraft, will certainly promote current regulations' future adaptation to these new approaches.

Although, for this thesis' case study computed data, the fourteen high-lift props configuration seems to be the most promising configuration, a more accurate and complete analysis evolving a greater number of parameters would be necessary to effectively evaluate the best configuration amongst the four proposed. The author decided to choose the twelve high-lift propellers configuration, similarly to the existent Tecnam modification by NASA — X-57 Maxwell. Although this comparison didn't allow to draw a full conclusion on the choice of configuration, it is possible to see the influence of the number of engines on the vertical tail size, weight, inertia, drag and take-off field length.

Despite the fact that the results are for the worst possible case, covering only the current certification requirements and disregarding the potentials of the DEP technology implementation, it was possible to estimate a minimum of 52% vertical empennage area reduction for the chosen Case II configuration (twelve high-lift propellers).

Considering the vertical empennage's modifications impacts on weight, inertia moments and products, drag, take-off performance and control and stability derivatives, the following conclusions may be drawn from the results of the implemented methodologies: a 7.1% reduction on empty weight, 13.3% reduction on parasite drag coefficient and a 24.1% reduction on take-off field length. The proposed reductions in the vertical tail changed the initial aircraft's aerodynamic angle-of-sideslip, roll rate, yaw rate and rudder control derivatives, hence those derivatives were computed based on analytic methods and the remaining aerodynamic derivatives were assumed to remain the same, for simplicity. Also, it was considered that a larger number of engines doesn't necessarily increase the maximum lift coefficient, since enough lift must be achieved even with failed engines. This consideration was made for simplicity in calculations, as this influence's certification (although promising for structural load reduction) is still under discussion.

Generalising the improvements' conclusions for similar aircraft: an almost logarithmic relation between the vertical empennage area reduction and the number of engines would be expected, where the higher the number of high-lift props, the bigger the area reduction; a possibly negative quadratic relation between the number of high-lift props and the weight reduction, where adding more engines is only increasingly beneficial up to a certain point (up to around fourteen high-lift props in the studied case); a high slope linear relation between the number of high-lift props and the parasite drag reduction appears for the three last data points, and an almost irrelevant reduction for the first two, suggesting an increasing reduction from 12 high-lift props on and a not significant one for fewer; an almost linear negative slope relation can be found between the total take-off field length and the number of high lift props (due to the total thrust decrease as the number of electric engines increases, shown in publications [30] for the engines considered).

CAD representations of all considered configurations was developed using CATIA v5[1] and OpenVSP[2] for result visualisation and to provide accurate measures for the mentioned calculations.

Dynamic models of the two study cases were developed from the models' data presented on Sections 3.1.1 and 3.2.3. The used parameters impact the developed controllers' performance, making their correct estimation and validation relevant. With the adopted optimisation methodology all empirical methods are approximations, that is, all the parameters are estimated and their reliability level is uncertain. Also, the developed dynamic model itself for the DEP case has its limitations, for example the roll due to yaw induced by the dynamic pressure variation along the wing's sections is very roughly estimated.

[1] CATIA v5, Dassault Systèmes S.A.

[2] OpenVSP, NASA gov

Although there are already plenty of researches demonstrating different propulsion-based control approaches, further investigation on the various aerodynamic differential-thrust contributions and relations is needed since theoretical insight into the creation of dynamic models for DEP aircraft is still very scarce in literature.

Given the importance of certain key system properties remaining almost unchanged when subjected to disturbances in aircraft control systems, ensuring the controller's robustness was an essential prerequisite for this work since it was intended to obtain a controller that meets design specifications under normal system operating conditions and ensures satisfactory performance in the presence of disturbances. As so, the gain for an $LQR$ and an $H_\infty$ controllers was designed and their response to an atmospheric disturbance compared for case I, in order to answer to *"Which gain design is more suitable in terms of robustness for this study: $LQR$ or $H_\infty$?"*. This comparison proved the $H_\infty$ controller robustness and validated the controller selection, settling in the desired values in slightly less time than the $LQR$ controller and with a lower peak overshoot than for the $LQR$ controller.

For case II, the previously validated $H_\infty$ gain design was computed and the hybrid-controller specifications as well as the corresponding hybrid structure (with a standalone propulsion control operation mode as well as a conventional mode) were established, covering *"How will the propulsion controller be structured?"*.

As expected, finding the adequate weighting matrixes $R$ and $Q$ made the computing of both optimal controllers' gain design difficult and may even limit its utilisation, as developing an efficient and adequate strategy for computing them requires a more profound physical understanding of the controlled system. The weighting matrixes proved too complex to compute through Luo et al.'s method[93] for 7x7 matrixes and Bryson's method[92] was used instead and showed good results. Another challenge regarding the gain design was finding the proper $H_\infty$ $\varepsilon$ and $\gamma$ parameters. The adopted methodology involved randomly assigning $\varepsilon$ and estimating the magnitude of the $\gamma$ parameter accordingly, but using transformation matrixes in the frequency domain to scale these parameters might have made its computation easier and further optimal.

Overall, it was possible to answer the questions proposed for this thesis, and it proved to be indeed possible to robustly control the studied aircraft through its distributed propulsion system with no limitations for the simulated cases. The developed DEP closed-loop control demonstrated and analysed is considered to be appropriate for similar vehicles of the same size and class and was proven to be appropriately chosen, as it proved its robustness in the face of disturbances, which was the set goal for the requirements. This explains *"What is the generic relevance of the model used?"* and *"Was that model appropriately chosen?"*.

For the coordinated turn simulation it was possible to compare the aircraft's response to different turn rates and analyse the control actuation for the distributed propulsion mode and the conventional mode. In the simulations, the aircraft's distributed propulsion replaced up to around $12.5$ degrees of rudder and showed capacity for more. Extended simulations were made but, since this type of aircraft won't go beyond the simulated turn rates, other scenarios and envelope points need to be analysed in order to allow understanding the limitations of this form of control, namely at take off, best climb and final landing phases, which are the flight conditions limiting the margin for yaw moment generation due to the low or high power by them demanded, this answers the question *"Can the standalone propulsion mode handle a coordinated turn? To what extent?"*.

As to *"Can the standalone propulsion mode handle engine failures? To what extent?"*: for the engine out simulation it is clear that the aircraft can readjust its thrust distribution on its own to compensate the respective thrust loss without any controller gain adjustment/modification,

if no restrictions are imposed on the throttle setting. To clarify the question *"Which control authority limitations are implied in the standalone propulsion mode?"*, simulations proved that both for a coordinated turn and at straight level flight there are no limitations on the directional control capabilities of this mode, even with the critical engine out. The engine's dynamics model developed in this work has limitations but overall seems to be appropriate and well represent the effects of the engine's differential thrust on the aircraft.
As proven during simulations, including in the engine out case, with distributed propulsion as a form of aircraft control, the rudder deflection-envelope diminished (having been null for performing coordinated turns while maintaining flight speed and altitude), granting more room for a sub-sequential empennage reduction, lowering the maximum rudder deflection to bellow the established $24$ degrees. Also, as the ability to overcome the failed engine adverse yaw without exceeding the available power and while using a $\delta_{th_n} = 0.53$ throttle setting for cruise and reducing take-off field length when comparing to the original Tecnam configuration, could mean that the engines are overpowered and lower power engines could be used instead, sacrificing of course the two previously mentioned variables (reducing available power at cruise and increasing take-off field length), reinforcing that the vertical empennage could be further reduced or even both, depending on the desired project requirements. Undoubtedly, a cautious analysis of other scenarios and envelope points is needed, as well as a trade-off analysis prioritising each of the design requirements to understand the most beneficial solution.
Thus, the simulations allow concluding that a fully operational controller was designed, answering the first question this work has proposed answering to based on the obtained results and the applied optimisation allowed to partially answer the second question, completed by the same simulations' results, which can be further investigated in order to generalise the improvements to other aircraft types and classes.

In summary, this work allowed shining a light on the distributed electric propulsion technology potential as a control actuator, addressing the issue of lateral-directional motion control by designing a hybrid robust roll-yaw controller which is able to deal with a standalone propulsion control operation mode as well as a conventional mode, combining, if needed, both propulsion control and control-surface operation. Since the DEP technology has zero operation emissions, a step towards reducing our environmental footprint was taken in a time where the need for environmentally responsible solutions in aircraft technology is an indisputable concern. These new developments open countless opportunities for new research on the topic, enhancing the vision of a better tomorrow and sustainable aviation, by boosting the emergence of new and more flexible designs and making use of novel approaches and technology.

Hence, the answers to the aforementioned questions can be further synthesised as follows:

1. **How to robustly control an aircraft through its distributed electric propulsion system?**

To recap: the solution identified in this work consists in enabling the distributed electric propulsion aircraft to add more thrust in one side than the other, in order to turn the aircraft towards the side with the least thrust power, by individually controlling its throttle inputs. A robust controller with independent throttle settings, one for each electric propeller, was designed by applying $H_\infty$ control theory gains and modelling a hybrid control structure, which includes a standalone propulsion mode as well as a conventional mode that, if needed, may be combined.

2. **How to use this capability to introduce improvements in an aircraft's design?**

In brief: considering the engine's thrust for flight control allows a reduction of the flight control surfaces and subsequently potentiating tail size improvements. Examining the vertical empennage's modifications impacts on weight, inertia moments and products, drag, take-off performance and control and stability derivatives several relations were established, namely that the higher the number of high-lift props, the bigger the empennage area reduction; adding more engines is only increasingly beneficial up to a certain point; the more high-lift props, the greater parasite drag reduction; the fewer the electric engines (at current state of art [30]), the shorter the total take-off field length.

## 6.1 Published work

*"Hybrid Lateral-Directional Robust Flight Control with Propulsive Systems"* oral presentation at the International Conference on Aerospace Systems and Avionics (ICASA 2019), to be held in Lisbon, Portugal scheduled for October $30^{th}$-$31^{st}$, 2019 and rescheduled for February $6^{th}$-$7^{th}$, 2020.

## 6.2 Future work

It is this author's opinion that interesting future work directives could be to build up on this research's findings, expanding both the research and used theory, highlighting:

- Generalise the influence of the number of engines and the type of engine (electric) on the advantages of the developed control method and grade/evaluate the interest of its use.
- Compute the influence of each approximation made and premise assumed on the achieved control in order to allow a generalisation of the developed dynamic model.
- Examine how to achieve the required level of safety and how to adapt certification rules for distributed electric propulsion aircraft.
- Understand how the control maneuverability depends on the number of engines, by simulating the dynamic models of the other developed configurations.
- Develop a longitudinal dynamics model and couple both motions.
- Assess the non linear dynamic behaviour of the designed controllers on the studied aircraft (Case I and Case II).
- Extend the simulated flight scenarios to other points of the envelope, in order to generalise the results and identify the control limitations, particularly at take off, best climb and final landing, which are the flight conditions limiting the margin for yaw moment generation due to the low or high power by them demanded.
- Approach the distributed electric propulsion control problem formulated in this work from a fail safe electrical system architecture point of view, accounting for the required redundancy, reliability and maintainability.
- Incorporate the use of propulsion control in a multi-disciplinary design optimisation (MDO) aircraft design methodology.

# Bibliography


[1] D. Mclean, *Automatic flight control systems*. Prentice Hall New York, 1990, vol. 16. xvii, 5, 56

[2] "Photo credit: William scheck, historynet," https://www.historynet.com/lawrence-sperry-autopilot-inventor-and-aviation-innovator.htm, accessed: 2019-08-21. xvii, 10

[3] D. Jenkins, T. Landis, and J. Miller, *American X-vehicles: An Inventory, X-1 to X-50*, ser. Monographs in aerospace history. National Aeronautics and Space Administration, Office of External Relations, 2003. xvii, 10, 11

[4] "Photo credit: NASA/dryden flight research center," https://www.dfrc.nasa.gov/Gallery/Photo/PCA/HTML/EC94-42805-1.html, accessed: 2019-08-20. xvii, 12

[5] "Photo credit: NASA/dryden flight research center," https://www.nasa.gov/sites/default/files/images/328928main_EC95-43247-2_full.jpg, accessed: 2019-08-20. xvii, 12

[6] "Photo credit: NASA illustration," https://www.nasa.gov/sites/default/files/thumbnails/image/pca_rotation.jpg, accessed: 2019-08-20. xvii, 13

[7] "Photo credit: NASA illustration," https://www.nasa.gov/sites/default/files/thumbnails/image/pca_turning.jpg, accessed: 2019-08-20. xvii, 13

[8] "Photo credit: NASA/glenn flight research center," https://ntrs.nasa.gov/archive/nasa/casi.ntrs.nasa.gov/20150002081.pdf, accessed: 2019-09-29. xvii, 20

[9] "Photo credit: NASA/glenn research center," https://www.nasa.gov/content/hybrid-wing-body-goes-hybrid, accessed: 2019-09-29. xvii, 20

[10] "Photo credit: NASA/glenn research center," https://www.nasa.gov/feature/aviation-renaissance-nasa-advances-concepts-for-next-gen-aircraft, accessed: 2019-09-29. xvii, 20

[11] "Photo credit: NASA/glenn research center," https://www1.grc.nasa.gov/aeronautics/hep/airplane-concepts/, accessed: 2019-09-29. xvii, 20

[12] "Photo credit: Aurora flight sciences manassas, virginia, usa," https://evtol.news/aircraft/aurora-flight-sciences/, accessed: 2019-09-29. xvii, 21

[13] "Photo credit: Lilium, munich, germany," https://lilium.com/newsroom, accessed: 2019-09-29. xvii, 21

[14] "Photo credit: Lilium, munich, germany," https://lilium.com/the-jet, accessed: 2019-09-29. xvii, 21

[15] "Photo credit: NASA langley research center," https://www.advancedaircraftcompany.com/greased-lightning/, accessed: 2019-09-29. xvii, 21

[16] "Photo credit: Joby aviation, santa cruz, california," https://vtol.org/files/dmfile/22JobyS2Moore2.pdf, accessed: 2019-09-29. xvii, 22

[17] "Photo credit: Airbus, leiden, netherlands," https://www.airbus.com/newsroom/stories/vahana-marks-a-major-milestone-with-successful-full-transition-flight.html, accessed: 2019-09-29. xvii, 22

[18] "Photo credit: NASA graphic / NASA langley/advanced concepts lab, ama, inc." https://ntrs.nasa.gov/archive/nasa/casi.ntrs.nasa.gov/20160007822.pdf, accessed: 2019-09-29. xvii, 22

[19] "Photo credit: NASA/glenn research center." xvii, 22, 25

[20] P. Vecchia, F. Nicolosi, and A. De Marco, "Stability, flying qualities and longitudinal parameter estimation of a twin-engine cs-23 certifed light aircraft," *Aerospace Science and Technology*, vol. 24, pp. 226–240, 01 2011. xvii, 25, 26, 28, 32, 37, 39, 42, 44

[21] D. Raymer, *Aircraft Design: A Conceptual Approach, Sixth Edition*, 01 2019. xvii, xix, 18, 19, 40, 41

[22] Cooper and Harper, "The use of pilot rating in the evaluation of aircraft handling qualities," *Journal of Geodesy*, 1969. xvii, xix, 59, 61

[23] M. V. Cook, *Flight Dynamics Principles*. Butterworth-Heinemann, 2012. xviii, 77, 78

[24] F. W. Burcham Jr, C. G. Fullerton, and T. A. Maine, "Manual manipulation of engine throttles for emergency flight control," 2004. xix, 1, 14

[25] R. Nelson, *Airplane Stability and Automatic Control*. WCB/McGraw Hill New York, 1998, vol. 2. xix, 60

[26] G. D. Padfield and B. Lawrence, "The birth of flight control: An engineering analysis of the wright brothers' 1902 glider," *The Aeronautical Journal (1968)*, vol. 107, no. 1078, pp. 697–718, 2003. 9

[27] A. E. Bryson, "New concepts in control theory, 1959-1984 (dryden lectureship in research)," *Journal of Guidance Control and Dynamics*, vol. 8, 07 1985. 9

[28] B. L. Stevens, F. L. Lewis, and E. N. Johnson, *Aircraft control and simulation: dynamics, controls design, and autonomous systems*. John Wiley & Sons, 2015. 9, 10, 11, 66

[29] C. E. Billings, "Toward a human-centered aircraft automation philosophy," *International Journal of Aviation Psychology*, vol. 1, 10 1991. 10

[30] W. R. Evans, "Control system synthesis by root locus method," *Transactions of the American Institute of Electrical Engineers*, vol. 69, no. 1, pp. 66–69, jan 1950. 10

[31] D. Berry and G. Gilyard, "Airframe/propulsion system interactions - an important factor in supersonic aircraft flight control," in *Guidance and Control Conference*, 1973, p. 831. 11

[32] E. Rachovitsky, "Opportunities in flight/propulsion control coupling (fpcc)," vol. 1, 1974. 11

[33] E. Rachovitsky, R. Heimbold, R. Miller, and J. Hauge, "An approach to a methodology for selection and development of flight/propulsion control coupling technologies," vol. 1, 1976. 11

[34] J. Baer-Riedhart, "The development and flight test evaluation of an integrated propulsion control system for the himat research airplane," in *1st Flight Test Conference*, 1981, p. 2467. 11

[35] D. S. Joshi, P. D. Shaw, J. Hodgkinson, S. M. Rock, J. H. Vincent, and W. S. Fisk, "A design approach to integrated flight and propulsion control," vol. 1. JSTOR, 1983, pp. 154–164. 11

[36] P. Shaw, K. Blumberg, D. Joshi, R. Anex, J. Vincent, and C. Skira, "Development and evaluation of an integrated flight and propulsion control system," in *21st Joint Propulsion Conference*, 1985, p. 1423. 11

[37] S. Rock, A. Emami-Naeini, and R. Anex, "Propulsion control specifications in integrated flight propulsion control systems," p. 3236, 1988. 11

[38] R. Smith, J. Chisholm, and J. Stewart, "Optimizing aircraft performance with adaptive, integrated flight/propulsion control," *Journal of engineering for gas turbines and power*, vol. 113, no. 1, pp. 87–94, 1991. 11, 12

[39] J. Burken, F. Burcham, T. Maine, J. Feather, S. Goldthorpe, and J. Kahler, "Flight test of a propulsion-based emergency control system on the md-11 airplane with emphasis on the lateral axis," p. 3919, 1996. 12

[40] E. A. Jonckheere, G.-R. Yu, and C.-K. Chu, "$H_\infty$ control of crippled aircraft with throttles only," *IFAC Proceedings Volumes*, vol. 29, no. 1, pp. 7546–7551, 1996. 13

[41] E. A. Jonckheere, G.-R. Yu, and C.-C. Chien, "Gain scheduling for lateral motion of propulsion controlled aircraft using neural networks," vol. 5, pp. 3321–3325, 1997. 13

[42] E. A. Jonckheere and G.-R. Yu, "Propulsion control of crippled aircraft by $h_\infty$ model matching," *IEEE Transactions on Control Systems Technology*, vol. 7, 1999. 13

[43] T. T. N. H. Division), *Touchdown: The Development of Propulsion Controlled Aircraft at NASA Dryden*, ser. Monographs in Aerospace History, 2011, vol. 16. 13

[44] E. A. Jonckheere, Gwo-Ruey Yu, and Cheng-Chie Chien, "Gain scheduling for lateral motion of propulsion controlled aircraft using neural networks," in *Proceedings of the 1997 American Control Conference (Cat. No.97CH36041)*, vol. 5, June 1997, pp. 3321–3325 vol.5. 13

[45] J. F. Burcham and J. Burken, "Flight testing a propulsion-controlled aircraft emergency flight control system on an f-15 airplane," in *Biennial Flight Test Conference*, 1994, p. 2123. 13

[46] F. W. Burcham Jr, T. A. Maine, J. J. Burken, and J. Bull, "Using engine thrust for emergency flight control: Md-11 and b-747 results," 1998. 13

[47] J. Frank W. Burcham, J. J. Burken, T. A. Maine, and C. G. Fullerton, "Development and flight test of an emergency flight control system using only engine thrust on an md-11 transport airplane," 1997, p. 91. 13

[48] J. Frank Burcham and D. Pappas, "Development and flight test of an augmented thrust-only flight control system on an md-11 transport airplane," in *Guidance, Navigation, and Control Conference*, 1996, p. 3742. 13

[49] Y. Ochi and K. Kanai, "Automatic approach and landing for propulsion controlled aircraft by h/sub $\infty$/ control," in *Proceedings of the 1999 IEEE International Conference on Control Applications (Cat. No.99CH36328)*. 13, 14

[50] G.-R. Yu, "Gain scheduling for $H_\infty$ control of propulsion controlled aircraft," vol. 4, pp. 2373–2377, 2000. 14

[51] Y. Ochi, "Flight control system design for propulsion-controlled aircraft," vol. 219, no. 4. SAGE Publications Sage UK: London, England, 2005, pp. 329–340. 14

[52] Y. Hitachi and H. H. Liu, "H1-ltr technique applied to robust control of propulsion-controlled aircraft," in *AIAA Guidance, Navigation, and Control Conference, Chicago, IL, Aug*, 2009, pp. 10–13. 14

[53] J. Litt, D. Frederick, and T.-H. Guo, "The case for intelligent propulsion control for fast engine response," p. 1876, 2009. 14

[54] N. Nguyen and V. Stepanyan, "Flight-propulsion response requirements for directional stability and control," p. 3471, 2010. 15

[55] J. Urnes, "Flight control for multi-engine uav aircraft using propulsion control," p. 2570, 2012. 15

[56] L. Lu and K. Turkoglu, "Robust $H_\infty$ loop-shaping differential thrust control methodology for lateral/directional stability of an aircraft with a damaged vertical stabilizer," 08 2015. 15

[57] L. K. Lu and K. Turkoglu, "Adaptive differential thrust methodology for lateral/directional stability of an aircraft with a completely damaged vertical stabilizer," *International Journal of Aerospace Engineering*, 2018. 15

[58] H. D. Kim, A. T. Perry, and P. J. Ansell, "A review of distributed electric propulsion concepts for air vehicle technology," pp. 1–21, 2018. 16, 17, 18

[59] J. B. Winborn, "The ADAM III v/STOL concept," in *VTOL Research, Design, and Operations Meeting*. American Institute of Aeronautics and Astronautics, feb 1969. 16

[60] A. Ko, J. Schetz, and W. Mason, "Assessment of the potential advantages of distributed propulsion for aircraft," jan 2003. 16, 17

[61] H. D. Kim and J. D. Saunders, "Embedded wing propulsion conceptual study," 2003. 16

[62] H. D. Kim, J. L. Felder, M. T. Tong, and M. Armstrong, "Revolutionary aeropropulsion concept for sustainable aviation:turboelectric distributed propulsion," 2013. 16

[63] L. Leifsson, A. Ko, W. Mason, J. Schetz, B. Grossman, and R. Haftka, "Multidisciplinary design optimization of blended-wing-body transport aircraft with distributed propulsion," *Aerospace Science and Technology*, vol. 25, pp. 16–28, 2013. 16

[64] N. T. Nguyen, K. Reynolds, E. Ting, and N. Nguyen, "Distributed propulsion aircraft with aeroelastic wing shaping control for improved aerodynamic efficiency," *Journal of Aircraft*, pp. 1–19, 2018. 17

[65] N. K. Borer, M. D. Patterson, J. K. Viken, M. D. Moore, J. Bevirt, A. M. Stoll, and A. R. Gibson, "Design and performance of the NASA sceptor distributed electric propulsion flight demonstrator." 17, 22, 25

[66] S. A. Rizzi, D. L. Palumbo, J. Rathsam, A. W. Christian, and M. Rafaelof, *Annoyance to Noise Produced by a Distributed Electric Propulsion High-Lift System*. 17

[67] M. Hepperle, "Electric flight - potential and limitations," 2012. 17, 18

[68] "Effects of battery manufacturing on electric vehicle life-cycle greenhouse gas emissions," https://theicct.org/sites/default/files/publications/EV-life-cycle-GHG_ICCT-Briefing_09022018_vF.pdf, accessed: 2019-09-28. 17

[69] A. Hughes and B. Drury, *Electric Motors and Drives Fundamentals: Types and Applications*, 5th ed. Elsevier, 2019. 17

[70] A. S. Gohardani, G. Doulgeris, and R. Singh, "Challenges of future aircraft propulsion: A review of distributed propulsion technology and its potential application for the all electric commercial aircraft," *Progress in Aerospace Sciences*, vol. 47, pp. 369–391, 2011. 18, 19

[71] S. Farokhi, *Future Propulsion Systems and Energy Sources in Sustainable Aviation*, ser. Aerospace Series. Wiley, 2020. 18

[72] J. Felder, H. Kim, and G. Brown, "Turboelectric distributed propulsion engine cycle analysis for hybrid-wing-body aircraft," 2009. 19, 20

[73] J. Felder, M. Tong, and J. Chu, "Sensitivity of mission energy consumption to turboelectric distributed propulsion design assumptions on the n3-x hybrid wing body aircraft," 2012. 20

[74] M. J. Armstrong, C. A. H. Ross, M. J. Blackwelder, and K. Rajashekara, "Trade studies for NASA n3-x turboelectric distributed propulsion system electrical power system architecture," *SAE International Journal of Aerospace*, vol. 5, 10 2012. 20

[75] P. M. Rothhaar, P. C. Murphy, B. J. Bacon, I. M. Gregory, J. A. Grauer, R. C. Busan, and M. A. Croom, *NASA Langley Distributed Propulsion VTOL TiltWing Aircraft Testing, Modeling, Simulation, Control, and Flight Test Development*. 20

[76] "Introducing the lilium jet," https://lilium.com, accessed: 2019-09-29. 21

[77] "Fast-forwarding to a future of on-demand urban air transportation," https://www.uber.com/elevate.pdf, accessed: 2019-09-29. 22

[78] S. Clarke, M. Redifer, K. Papathakis, A. Samuel, and T. Foster, "X-57 power and command system design," 2017. 22, 25, 35

[79] "Tecnam p2006t type-certificate datasheet - easa.a.185," https://www.easa.europa.eu/sites/default/files/dfu/EASA%20TCDS%20P2006T%20issue%208.pdf, accessed: 2019-06-12. 25, 26, 35, 37

[80] M. D. Patterson, J. M. Derlaga, and N. K. Borer, "High-lift propeller system configuration selection for nasa's sceptor distributed electric propulsion flight demonstrator," p. 3922, 2016. 28, 35, 46, 110, 113

[81] "Part 25 - airworthiness standards: Transport category airplanes," https://www.ecfr.gov/cgi-bin/text-idx?SID=5821229ca187ea496310b2dd70b3a2a3&mc=true&node=pt14.1.25&rgn=div5, accessed: 2019-06-11. 29, 30, 31, 40

[82] E. N. Van, P. Troillard, J. Jézégou, D. Alazard, P. Pastor, and C. Doll, "Reduction of vertical tail using differential thrust: influence on flight control and certification," *AEGATS'18, Toulouse, France*, pp. 1–8, 2018. 29

[83] R. Finck and M. A. C. S. L. MO., *USAF (United States Air Force) Stability and Control DATCOM*. Defense Technical Information Center, 1978. 30, 31, 32

[84] J. Roskam, *Airplane Design: Preliminary Configuration Design and Integration of the Propulsion System*, ser. Airplane Design. DARcorporation, 1997, no. part II. 34

[85] ——, *Airplane Design: Component Weight Estimation*, ser. Airplane Design. DARcorporation, 1999, no. part V. 34, 35, 37

[86] ——, *Airplane Design: Preliminary Calculation of Aerodynamic, Thrust and Power Characteristics*, ser. Airplane Design. DARcorporation, 2000, no. part VI. 34, 38, 39, 42

[87] F. Nicolosi, A. D. Marco, and P. D. Vecchia, "Flight tests, performances, and flight certification of a twin-engine light aircraft," *Journal of Aircraft*, vol. 48, pp. 177–192, 01/02 2011. 41

[88] K. Takahashi, H. Fujimoto, Y. Hori, H. Kobayashi, and A. Nishizawa, "Modeling of propeller electric airplane and thrust control using advantage of electric motor," pp. 482–487, 2014. 54

[89] C. Frangos and Y. Yavin, "Design methodology for linear optimal control systems," *Journal of guidance, control, and dynamics*, vol. 15, no. 5, pp. 1302–1304, 1992. 57

[90] T. Kailath, *Linear Systems*, ser. Information and System Sciences Series. Prentice-Hall, 1980. 58

[91] P. P. Khargonekar, I. R. Petersen, and M. A. Rotea, "$H_\infty$-optimal control with state-feedback," *IEEE Transactions on Automatic Control*, vol. 33, no. 8, pp. 786–788, 1988. 64, 65, 66

[92] A. E. Bryson and Y.-C. Ho, *Applied Optimal Control: Otimization, Estimation and Control*. Routledge, 1975. 65, 67, 111

[93] J. Luo and C. E. Lan, "Determination of weighting matrices of a linear quadratic regulator," *Journal of Guidance, Control, and Dynamics*, vol. 18, no. 6, pp. 1462–1463, 1995. 65, 66, 67, 111

# Appendix A

# Annexes

## A.1 Model-Based Design — block diagram environment

**Model-Based Design**
**block diagram environment**

**Contents**

# 1. ModelBasedDesign

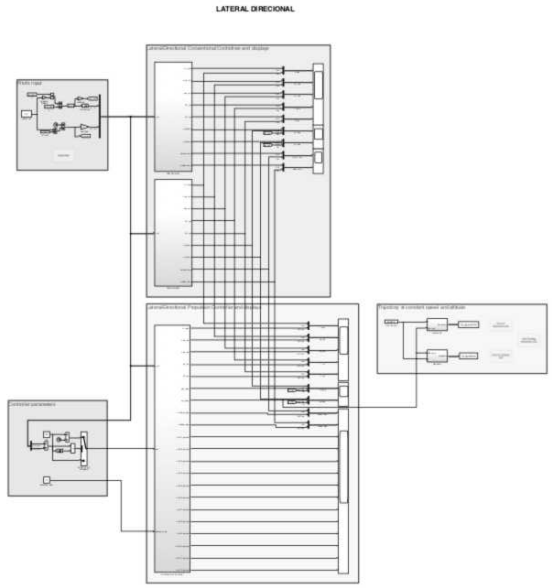


Figura 1.1. ModelBasedDesign





## 1.1. Geocentric

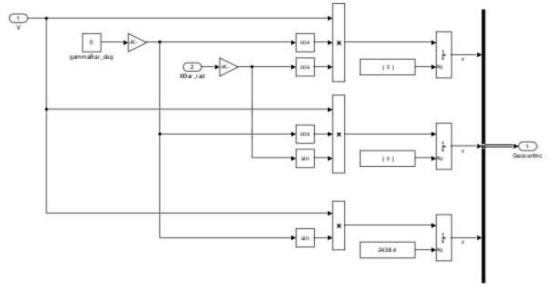


Figura 1.2. ModelBasedDesign/Geocentric

## 1.2. Geodesic

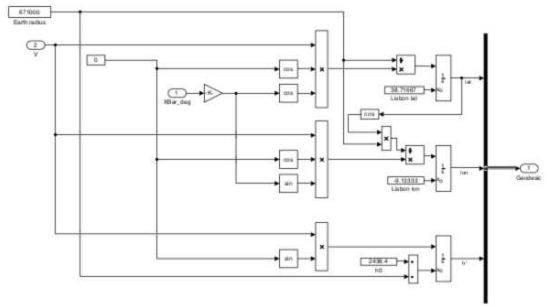


Figura 1.3. ModelBasedDesign/Geodesic





## 1.3. Hinf Controller

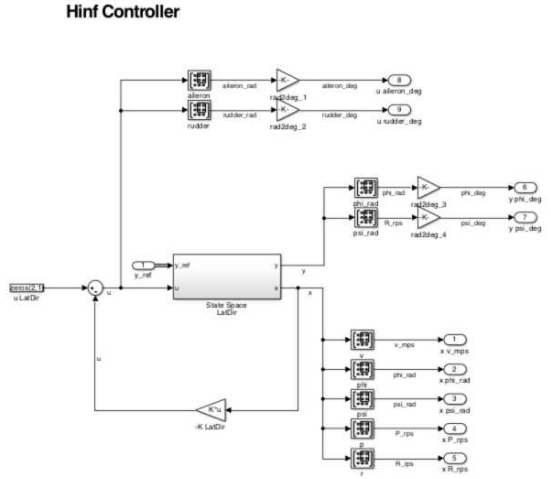


Figura 1.4. ModelBasedDesign/Hinf Controller

### 1.3.1. State Space LatDir

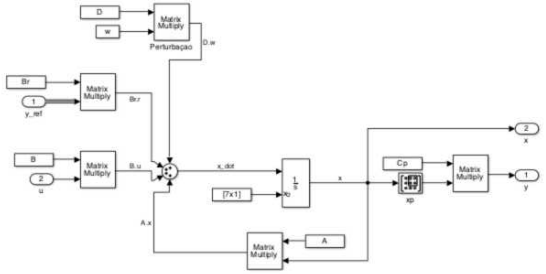


Figura 1.5. ModelBasedDesign/Hinf Controller/State Space LatDir





## 1.4. Hinf Propulsion Controller

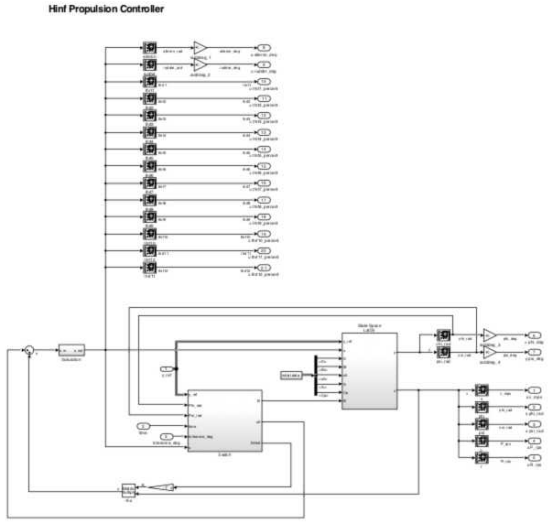


Figura 1.6. ModelBasedDesign/Hinf Propulsion Controller

### 1.4.1. Initial Data

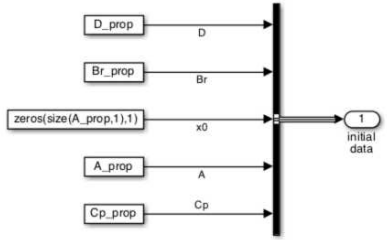


Figura 1.7. ModelBasedDesign/Hinf Propulsion Controller/Initial Data





### 1.4.2. Saturation

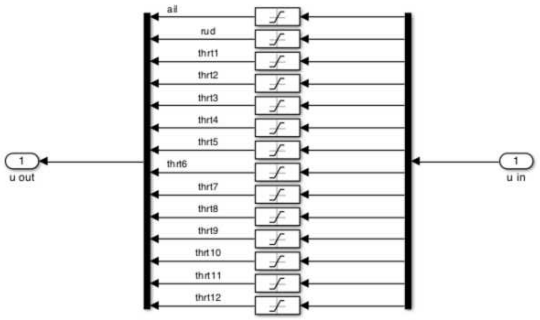


Figura 1.8. ModelBasedDesign/Hinf Propulsion Controller/Saturation

### 1.4.3. State Space LatDir

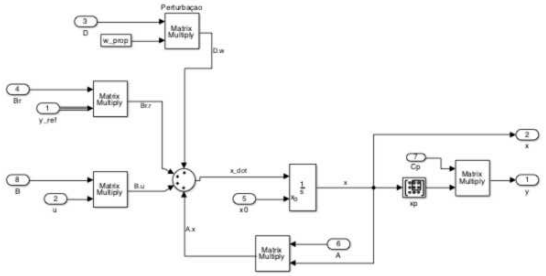


Figura 1.9. ModelBasedDesign/Hinf Propulsion Controller/State Space LatDir





### 1.4.4. Switch

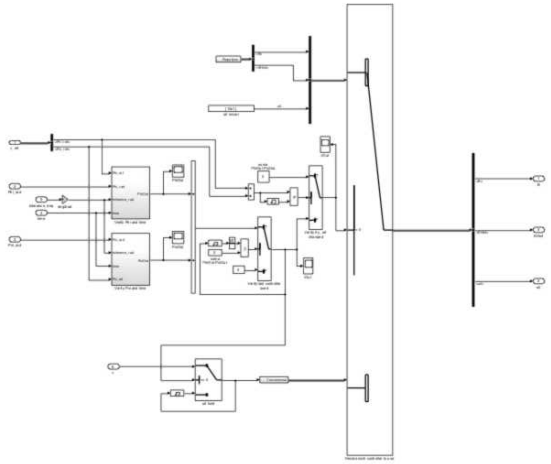

Figura 1.10. ModelBasedDesign/Hinf Propulsion Controller/Switch

#### 1.4.4.1. Conventional Controller Data

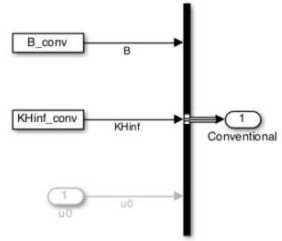


Figura 1.11. ModelBasedDesign/Hinf Propulsion Controller/Switch/Conventional Controller Data





#### 1.4.4.2. Propulsion Conroller Data

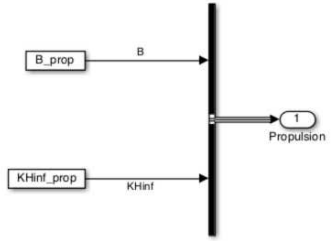


Figura 1.12. ModelBasedDesign/Hinf Propulsion Controller/Switch/Propulsion Conroller Data

### 1.4.4.3. Verify Phi and time

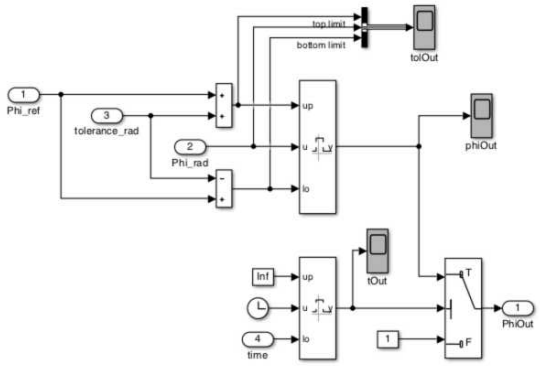


Figura 1.13. ModelBasedDesign/Hinf Propulsion Controller/Switch/Verify Phi and time





#### 1.4.4.3.1. Interval Test Dynamic

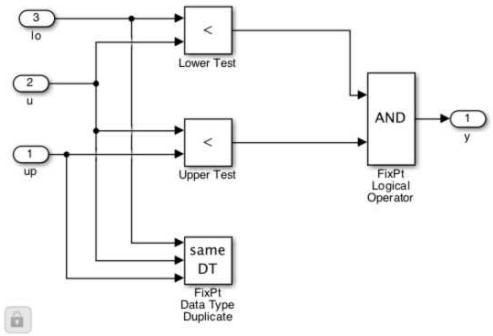


Figura 1.14. ModelBasedDesign/Hinf Propulsion Controller/Switch/Verify Phi and time/Interval Test Dynamic

#### 1.4.4.3.2. Interval Test Dynamic1

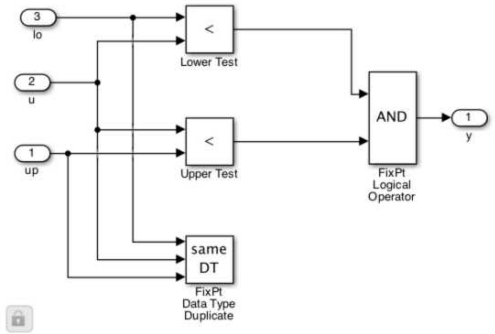


Figura 1.15. ModelBasedDesign/Hinf Propulsion Controller/Switch/Verify Phi and time/Interval Test Dynamic1





#### 1.4.4.4. Verify Psi and time

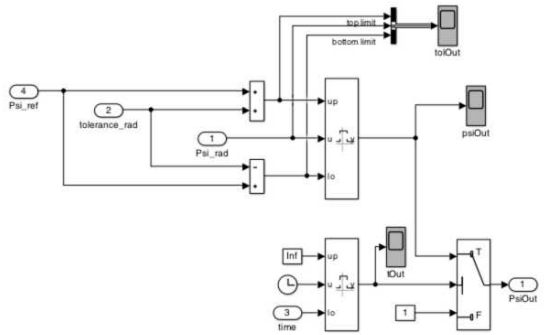


Figura 1.16. ModelBasedDesign/Hinf Propulsion Controller/Switch/Verify Psi and time

#### 1.4.4.4.1. Interval Test Dynamic

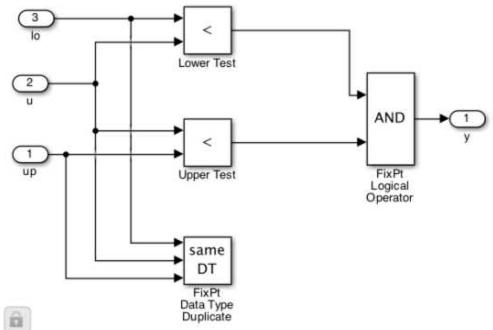


Figura 1.17. ModelBasedDesign/Hinf Propulsion Controller/Switch/Verify Psi and time/Interval Test Dynamic





#### 1.4.4.4.2. Interval Test Dynamic1

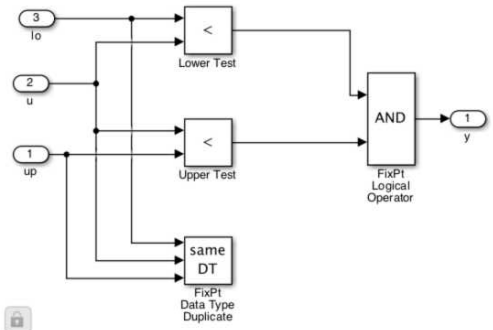


Figura 1.18. ModelBasedDesign/Hinf Propulsion Controller/Switch/Verify Psi and time/Interval Test Dynamic1

## 1.5. LQR Controller

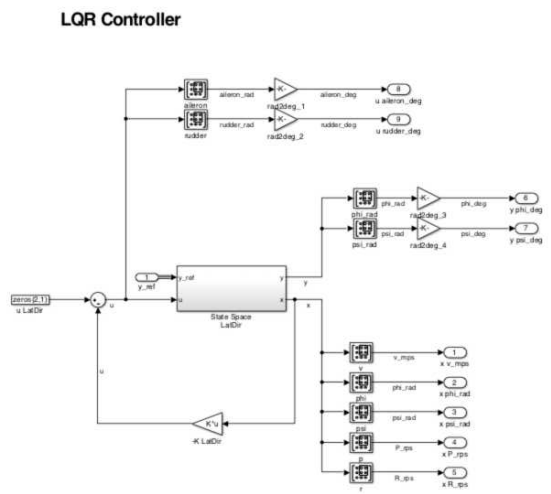


Figura 1.19. ModelBasedDesign/LQR Controller





### 1.5.1. State Space LatDir

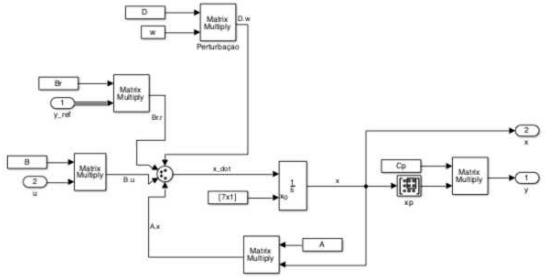


Figura 1.20. ModelBasedDesign/LQR Controller/State Space LatDir

## 1.5. Subsystem1

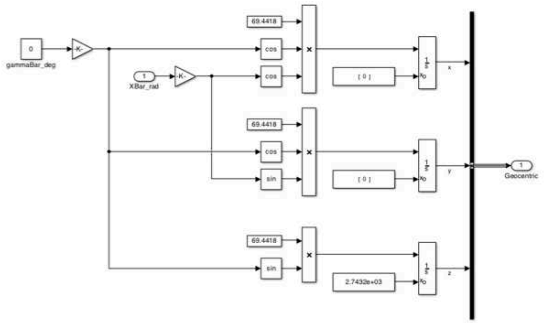


Figura 1.19. LateralDirectionalController4/Subsystem1





## 1.6. Subsystem2

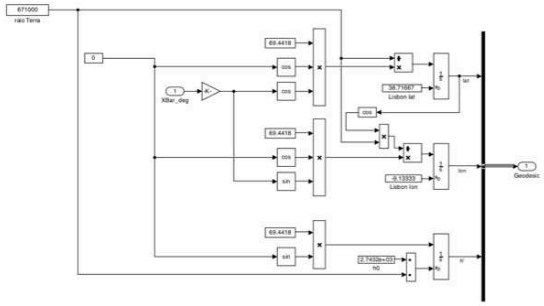


Figura 1.20. LateralDirectionalController4/Subsystem2